



Optical Interconnects For Trapped-Ion Quantum Transmitters

By

Mojtaba Ghadimi

Master of Science in Physics

SUBMITTED IN FULFILMENT OF
THE REQUIREMENTS OF THE DEGREE OF
DOCTOR OF PHILOSOPHY

Principal Supervisor:

Dr. Mirko Lobino

Dr. Erik W. Streed

Associate Supervisor:

School of Natural Sciences,
Griffith University,
Australia.

August 24, 2016

© Copyright 2016
by
Mojtaba Ghadimi

This work has not previously been submitted for a degree or diploma in any university. To the best of my knowledge and belief, the thesis contains no material previously published or written by another person except where due reference is made in the thesis itself.

Mojtaba Ghadimi

Acknowledgments

My acknowledge goes here.

Abstract

This thesis describes the use of diffractive mirrors for efficient collection of photons from an ion in a modern surface Paul trap. Ion light collection is one of the important steps of most of the quantum computing and communication protocols using trapped ions and has a direct effect on the performance of these protocols. This is the first demonstration of an integrated optic for a surface ion trap and a step towards realizing scalable quantum computing and communication using trapped ions. These mirrors are monolithically integrated onto the ground electrode of the trap. The fabrication of the mirrors has been accomplished by patterning diffraction rings on the silicon dioxide substrate of the trap chip and then coating it with aluminium to form a diffractive mirror integrated onto the electrode. We verified that the altered trap is still functional and demonstrated that these mirrors substantially increase the efficiency of free space ion light collection and ion light single mode fibre coupling. The mirror design is aberration free and we demonstrated this by obtaining near Diffraction-limited image of the ion. To measure the diffractive mirror collection efficiency, we performed a single photon generation protocol based on an optical pumping scheme and one chapter of this thesis describes the implementation of this scheme.

Contents

Acknowledgments	iii
Abstract	iv
Contents	iv
List of Figures	vii
1 Introduction	2
2 Integrated Diffractive Mirror Trap	7
2.1 Paul RF Trap	7
2.2 GTRI Microwave I Trap	12
2.2.1 DC Electrodes Voltage Control and Shutting	15
2.2.2 RF Electrodes and RF Voltage Generation	19
2.3 Diffractive Mirrors	21
2.3.1 Theory of Diffractive Mirrors	22
2.3.2 Design of Diffractive Mirrors	25
2.3.3 Fabrication Of The Diffractive Mirrors	28
2.3.4 Diffractive Mirrors Characterization	34
2.4 Atom source	40
2.5 Vacuum System	41
3 Laser Systems, Cooling and Ionization	43
3.1 Scattering Rate and Saturation Intensity	43
3.2 Yb Atomic Transitions	44
3.3 Ionization	45
3.4 Laser Cooling	47
3.5 External Cavity Diode Laser	48
3.6 Optical Isolator	50
3.7 370 nm Diode Laser	51
3.7.1 Lock-in Amplifier	53

3.7.2	370 nm Laser Frequency Stablization	54
3.8	399 nm Diode Laser	59
3.8.1	399 nm Diode Laser Frequency Stablization	60
3.9	935 nm Diode Laser	63
3.10	Beam Combiner	63
4	Imaging and Optical System	65
4.1	Imaging Using External Bulk Optics	65
4.2	Diffraction-limited Imaging(Theory)	68
4.3	Imaging Using Microfabricated Collimators	72
4.3.1	Gaussian Beam Propagation Simulation	74
4.4	Near Diffraction-limited Image	76
5	Single Photon Generation	81
5.1	Atomic Transitions, Absoprtion and Emission Patterns	81
5.2	Automatic Control Of The Lasers and The Detectors Using Labview FPGA	85
5.3	Single Photon Generation Protocol	87
5.4	Experimental Setup	90
5.5	Characterization Of The Time Scales and Delays	94
5.6	Measuring Single Photons 2nd Order Correlation $g^{(2)}$	95
6	Efficient Photon Collection	97
6.1	Ion Fluorescence Collection	98
6.1.1	Experimental Setup	98
6.1.2	Theoretical Estimation Of Collection Efficiency	100
6.1.3	Measuring Collection Efficiency:	101
6.2	Single Mode Fibre Coupling Of the Ion Fluorescence	102
6.2.1	Experimental Setup	103
6.2.2	Theoritical Estimation OF Fibre Coupling Efficiency	104
6.2.3	Measuring Single Mode Fibre Coupling Efficiency	106
7	Conclusion	108
7.1	Future Work	108
References		109

List of Figures

2.1	A four rod conventional Paul trap. Two RF electrodes labelled 1 and 3 and two segmented DC electrodes labelled 2 and 4 that are grounded in the middle and held at a positive potential at the end segments (Left) and RF electric field (Right) (Field image after [1])	8
2.2	Stability diagram for different values of a and q . The area in the middle is stable but the areas on top and bottom are unstable regions. (Fig. after [2])	10
2.3	Microscope image of the Integrated Diffractive Mirror Trap (Left). Middle ground electrode is $80\mu m$ wide and RF electrodes are $30\mu m$ wide. Segmented parts at the top and the bottom of the image are Control DC electrodes. Right image is a schematic of RF electric field that creates a RF node on top of the trap. (Field image after [3])	11
2.4	Rotated coordinate system describing the DC quadrupole. (Fig. from [4]) .	12
2.5	A schematic of the $11 \times 11 mm^2$ silicon chip (a) and the active trapping region (b), showing RF and DC trapping electrodes, capacitive RF filters, the shaped loading slot, and the on-chip microwave waveguides. (Image after [4])	13
2.6	Trap components including a packaged device with top screen removed for clarity (a), a photograph of the wirebond interface (b), and a photograph of a fully installed device with microwave connections (c). (Image after [4])	14
2.7	A cross section showing internal layers of the Microwave I Chip (the vertical direction is scaled by 10x for visual clarity). (Image after [4])	15
2.8	Dimensions and electrode IDs of the trapping region for a Microwave I trap. The z coordinates along the length of the trap correspond to the ion positions relative to the loading position. (Image after [4])	17

2.9	Screenshot of Labview program interface for controlling DC electrodes for shuttling and applying compensation fields. On the top program displays the voltages that are currently being applied to the electrodes. Below that user can enter a destination in the "Where to go um" field and a speed in "m-sec /um" and start shuttling using the button "Start Shuttle / Update setting" to the lft of those. The input fields at the bottom allow user to choosa file for each waveform and selct between constant weight or postion dependent weight. Left inputs are used to save two presets for loading and shuttling and apply them whit a click of a button when needed.	18
2.10	Schematic of the helical resonator used for RF input of the trap (Image courtesy of Valdis Blums)	20
2.11	A Fresnel mirror with 2π cycles. Red arrows are incoming beams at the centre and at the offaxis distance r. Blue arrows are reflected beams that both go to the focal point (Fresnel mirror image taken from Tech Briefs Solutions website techbriefs.com)	24
2.12	Microscope image of the integrated diffractive mirror trap taken by GTRI and layout of the array of the optics	25
2.13	Left: Schematic of the design sizes for the 4-level grating structures. Right: Simulated diffraction efficiency as a function of the incidence angle of light. (Image courtesy of David Kielpinski)	27
2.14	Complete layout of a single wafer, incorporating defence against both ion height errors and lateral offset errors.(Image courtesy of David Kielpinski) .	28
2.15	Representative image of the substrate prepared by GTRI to send to Fraunhofer Institute (Detalis in text) (Image courtesy of David Kielpinski) . . .	29
2.16	Cross section as delivered by FHHI after diffractive mirror fabrication (mirror features are not to scale) (Detalis in text) (Image courtesy of David Kielpinski)	30
2.17	Small diffractive mirror features as received and after metal deposition. (Image courtesy of David Kielpinski)	31
2.18	a. Wafer after plasma etch b. Diffractive mirrors with oxide protection layer (Detalis in text) (Image courtesy of David Kielpinski)	31
2.19	a. DC/RF Metal Deposition and Etch b. Top metal deposition and etch c. Final Device Cross Section (Detalis in text) (Image courtesy of David Kielpinski)	32
2.20	Binary (left) and Hybrid (right) diffractive mirrors after completed ion trap fabrication (Image courtesy of GTRI)	32
2.21	Full Binary DOE on a completed ion trap (Image courtesy of GTRI)	33
2.22	Dark field image of DOE's on completed ion trap (Image courtesy of GTRI)	33
2.23	Ion transport image over the Self-Imager taken by GTRI	34

2.24 (a) Ion and image alignment when micromotion nulled. (b) Applied radial electric field pushes the ion to the right, with a corresponding movement of the image to the left. (Image taken by GTRI)	35
2.25 a. : With the lens aperture closed, the depth-of-field is large enough that the central obscuration of the objective is visible as a dark inner region. The bright horizontal bands are patterns on the trap surface. b. Rough diagram of light collection from IDM with the reflective objective. The collimating optic collection efficiency data were taken so such that the light would both be collected by the lens and pass through the iris when the iris was closed. (Image courtesy of GTRI)	36
2.26 (a) Direct imaging (iris full open) and (b) collimated light imaging (iris closed to minimum) of the ion. (Image courtesy of GTRI)	36
2.27 PMT counts vs. ion position over the collimating optic for the lens aperture (iris) fully open and for the aperture at minimum (closed). The dashed lines are guides for the eye, showing the photon counts for the direct light from the ion, as extrapolated from the measurements in left wing of the plot. Both measurements have had position dependent backgrounds (measured separately without an ion) subtracted out. (Graph by GTRI)	37
2.28 Schematic for bulk collection optics. The trapped $^{174}\text{Yb}^+$ ion acts as a point source. The first lens collimates the collected fluorescence while the second lens focuses(re-image) the collected fluorescence onto a CCD camera. The distance between the 60mm lens and the 200mm lens is 260mm.	38
2.29 A single ion trapped in the IDM trap loading region. Imaging was performed using the bulk-lens objective. The diffractive mirrors were not used to obtain this image.	39
2.30 Comparison between bulk-lens and diffractive mirror imaging for a single ion in the IDM trap. Both images are taken under identical camera integration conditions and are background-subtracted to remove scattered light. Left: bulk-lens image. Right: diffractive mirror image obtained with the loading zone collimator. The fluorescence collection efficiency is estimated as 4%. The loading zone collimator is cut in the middle to create the loading hole. That is the reason why the aberration is high and the image size is much larger than the diffraction limited size.	39
2.31 Image of a single ion using the loading-zone diffractive mirror. The image was obtained by moving the ion several microns along the trap axis relative to the image in Fig. 26. The apparent duplication of the image is consistent with aberrations of the imaging system.	40

2.32 A schematic of the vacuum chamber which consists of the main octagonal part and branches for titanium sublimation pump, ion pump, ion gauge, oven connection Microwave feedthrough, DB25 connections and RF input. (Image courtesy of Valdis Blums)	41
3.1 Relevant energy levels for neutral and ionised Yb. Left: Neutral Yb energy levels from [5]. Right: Yb+ energy levels and branching ratios from [6]. Spontaneous decay times from $^2P_{1/2}$, $^2D_{3/2}$ and $^3D[3/2]_{1/2}$ states are 8.1ns, 53ms and 37.9ns respectively.	45
3.2 A schematic of external cavity diod laser components (Image from [7])	48
3.3) Schematic representation for the various frequency-dependent factors of an ECDL (Graph after [7])	50
3.4 A Faraday optical isolator. The input polariser, P1, is set to maximum transmission. The Faraday medium rotates the polarization by 45° and the output polariser, P2, set to the same angel, transmits the light. For a back-reflection the same process rotates the polarization in the same direction and this makes the direction of the polarization perpendicular to the axis of the input polariser, P1. Therefore the polariser rejects the light.(Image courtesy of Valdis Blums)	51
3.5 A schematic of 370 nm laser system. An external cavity diode laser generates a narrow linewidth laser near wavelength of 370 nm. Half-waveplates and polarizing beam splitters are used to split the power for different components. These components include a wavemeter, polarization spectroscopy system, Fabry-Perot cavity and two outputs with different frequencies for the ion trap. (Image courtesy of Valdis Blums)	53
3.6 A schematic of 370nm laser locking system. Fast lock section uses a signal from a Fabry-Perot cavity to stabilize the frequency. Slower signal that comes from an atomic reference is used to stabilize the Fabry-Perot cavity length.(Image courtesy of Valdis Blums)	55
3.7 Saturation spectroscopy system that uses a powerful counter-propagating beam to eliminate the Doppler broadening of the spectroscopy signal.(Image courtesy of Valdis Blums)	56
3.8 A schematic of polarization spectroscopy for 370nm laser. By using a pump beam with circular polarization and a prob beam with linear polarization that goes to a dual photodiode, A narrow zero crossing signal is generated.(Image courtesy of Valdis Blums)	57

3.9	Plot of polarisation spectroscopy and Fabry-Perot trace. The blue signal is the polarisation spectroscopy and the green signal is a Fabry-Perot trace. The free spectral range of the Fabry-Perot peaks is 1.25GHz. (Graph after [8])	59
3.10	Schematic for 399nm-laser polarisation spectroscopy. The first beam through the hollow cathode discharge lamp is a circularly polarised pump beam. After the discharge lamp the beam is split into 2 and a weaker linearly polarised probe beam is sent back through the hollow cathode discharge lamp. The probe beam is then sent to the dual photodiode. The laser frequency is modulated at 20KHz and a lock-in amplifier is used to amplify the signal. (Image after [8])	60
3.11	a. In a frequency dependent signal, change in signal is proportional to change in frequency times the derivative of the signal with respect to the frequency. b. Lock-in amplifier only amplifies the modulated signal which is proportional to derivative of the signal, therefore its output is positive where derivative is positive and vice versa.	62
3.12	399nm laser spectroscopy trace for neutral Yb. (Graph after [8])	62
3.13	Beam combiner setup for lasers in use. The two 370nm laser are combined using a polarizing beam splitter and then 399nm and 935nm lasers are added using diachronic mirrors. A fast steering mirror and a lens mounted on a translator is used for adjusting the position and angle of the beam that goes to the vacuum chamber.(Image courtesy of Valdis Blums)	64
4.1	A schematic of the lens configuration in the bulk imaging mode(Image is not to scale). Ion is located $60\mu m$ above the chip. The objective lens with focal length of 60mm is positioned 60mm away from the ion. This lens collimates the ion fluorescence. The collimated beam is focused on the camera using a second lens located 260mm away from the objective lens.	66
4.2	An image of the chip and a trapped ion located at loading zone captured using bulk imaging system. Ion is located the middle of the loading zone. The oval shaped scatter around the ion is the reflection of laser from the edge of the loading zone. DC electrodes are visible on both sides of the ion.	67
4.3	Three images from the ion and its image created by the self-imager diffractive optic for different ion positions. This optic forms an image from the ion on itself. left: the ion is located before the self-imager. middle: the ion is located on top of the self imager. images are almost overlapped and this shows that we have small lateral mismatch between optics fabrication ad electrodes fabrication. right: the ion located after the self-imager optic . . .	68

4.4	Graph of intensity of the diffraction pattern for a circular aperture. (Source: boundless.com)	69
4.5	Numerical aperture (NA) of an optical system is a dimensionless number that characterizes the range of angles over which the system can accept or emit light. It is equal to $n\sin(\alpha)$, where n is the index of refraction of the medium and α is half of the acceptance angle.	70
4.6	$1/e^2$ irradiance size of a Gaussian beam. w_0 and θ are the radius and the angle of the far-field divergence of the ideal zero order Gaussian beam and w_{0R} and θ_R are the radius and the angle of the far-field divergence of the mixed mode beam (image source:idexop.com)	70
4.7	An example of measuring M^2 by fitting equation 4.7 to the spot sizes around the focus point for the optical configuration shown in Fig. 4.10. The blue circles are the measured radii and the solid line is the fitted function. In this case M^2 is 1.36 which suggests that our beam is slightly aberrated.	72
4.8	Imaging using integrated collimating mirrors. The collimated light can be focused on the screen using a second lens. This method can be used if the distance between the mirror and the axillary lens is less than Rayleigh range of the beam which is 8.7 mm for one axis and 5.1 mm for the other axis. In our system the distance between the mirror and the first lens is 60 mm. This distance is much greater than the Rayleigh range of the beam and beam will be diverging when it reaches the lens. Gaussian beam simulation must be used to predict the evolution of the beam and design an optical system to image the light collected with the mirrors.	73
4.9	Numerical aperture(NA) of the mirror for the z axis. The distance from the ion to the mirror is 59.6 μm and the half side of the mirror along the z axis is 63.5 μm . Therefore $NA = \sin(\theta) = 0.73$	74
4.10	Gaussian beam propagation simulation for one of the settings we used for beam transfer. Blue curve shows the size of the beam in the x direction and red curve shows the size of the beam for z direction. Vertical black lines are lenses with f their focal lengths and z their distances from the diffractive mirror. r , zr and w labels, next to the focal length label, are radius of curvature, Rayleigh range and beam size respectively. Vertical blue and red lines show the focus points and for each axis the beam size, focus position and magnification is shown with respective color next to them. On the left side it displays the diffraction limited size at ion position for each axis.	76
4.11	Near diffraction limited image of an $^{174}\text{Yb}^+$ ion obtained using integrated diffractive mirror and comparison with diffraction limited size. Solid angle coverage is 13.3% and exposure time is 1 second. Ion image size measured to be 338(1.6)nm x 268(1.2)nm FWHM diameter.	77

4.12 The ion height for the different positions of the ion on the chip. When at the middle of the loading zone the ion height is $52 \mu m$. Ion height gradually increases by moving away from the loading point and becomes $58.6 \mu m$ outside of the loading zone. (GTRI)	79
5.1 Relevant transitions for the single photon generation protocol. The 370 nm $\sigma-$ laser can only excite $^2S_{1/2}m_s = +1/2$ to $^2P_{1/2}m_s = -1/2$ transition. The excited ion may emit a σ photon, with probability of $2/3$, and return back to $m_s = +1/2$ ground state or it may emit a π photon, with probability of $1/3$, and fall into $m_s = -1/2$ state. This is a dark state for $\sigma-$ laser and ion does not interact with the laser while in this state. For the $\sigma+$ laser, after excitation, the ion will undergo the same type of decaying and emission as the case for $\sigma-$ laser. The only difference is that it can only excite $m_s = -1/2$ ground state but not $m_s = +1/2$ ground state.	82
5.2 Emission Pattern of the π and σ polarized photons. top: For the π photons the maximum probability of emission is perpendicular to the magnetic field. No π photon is emitted along the magnetic field direction. bottom: The probability of emission of σ photons along the magnetic field is twice the probability perpendicular to the magnetic field. Both polarizations are linear, if they are emitted perpendicular to the magnetic field. In this direction polarization of the π photons is along the magnetic field and polarization of the σ photons is perpendicular to the magnetic field. (Image courtesy: http://astro1.panet.utoledo.edu)	83
5.3 FPGA control program's user interface screenshot. In the default mode, program shows counts/s for each detector with "DIO 14 Idle Counts(/s)" and "DIO 14 Idle Counts(/s)" outputs and applies the default values to the digital and analogue outputs. These default values are entered using vertical array inputs on the left side of the interface. User can also choose to repeat a sequence of events and change the values of outputs during time. Time length of each element is entered in "Element Clock Cycles" field and the corresponding value of digital and analogue outputs can be entered under each element cell in the inputs provided for each output port. After pressing "Start Sequence" program repeats the commands for the number of times given in "Number of Repetitions". During the execution of the sequence, DIO14 and DIO15 outputs display the live accumulation of number of detections for each time element.	86

5.4	a. Single photon generation protocol. 370 nm $\sigma-$ and $\sigma+$ lasers are on for 500 ns to generate a continuous excitation cycle to cool the ion. Then only $\sigma-$ laser remains on for another 500 ns to prepare the ion in the $m_s = -1/2$ ground state. For 1000 ns both lasers remain off to reliably separate the preparation process from generation process. Detection is turned on 750 ns after the preparation and remains on for 1000 ns. 1000 ns after perpetration, $\sigma+$ generation laser is turned on and remains on for 250 ns. This generates two σ photons on average and finally the ion emits a π photon and goes to the dark state. By filtering the σ photons using a polariser, Only one photon is collected during the generation step. b. Relevant transitions for single photon generation protocol.(for details on transitions see section 5.1 and Fig. 5.2)	88
5.5	Contour plot of the emission pattern on the mirror for π photons(left) and σ photons(right). (Plot courtesy of Erik Streed)	90
5.6	Schematics of the electronic setup for the single photon generation protocol. FPGA card controls the lasers and detection. To turn the lasers on and off, we use FPGA digital outputs to send a TTL signal to the AOM drivers. To turn the detection on and off, we use RF switches between PMTs and the time-tagger box.	91
5.7	Optical set-up for the collection of the single photons. a. The optical set-up used to transfer, collimate and resize the beam to send it to the single photon analyser set-up. The first two lenses are used in the bulk imaging set-up (4.1). We leave this set-up untouched and use a f=250 mm lens to collimate the light. The next two lenses(f=75 mm and f= 125 mm) act as a telescope to resize the beam. This last telescope is not necessary for this experiment and is used for mode matching for the fibre coupling experiment. b. Single photon analyser set-up. This set-up uses a polariser to filter the σ photons and let through the π photons. Using a non-polarising 50-50 beam splitter, the π photons are split and sent to the two photo multiplier tubes(PMTs). A time-tagger device analyses the statistical regime of photon emission(see section 5.6)	93
5.8	Number of photons generated in each step after time t after turning on the generation laser. The data is taken by repeating the sequence for one minute and then normalise the data to one at infinity. the blue fitted graph shows that the exponential time scale of the generation is $0.21\mu s$. This is equivalent to the average generation of 0.69 photons in each step.	94

5.9 Second order correlation $g^{(2)}$ for the single photon generation protocol. The raw $G^{(2)}$ counts are shown on the left red axis. To calculate $g^{(2)}(0)$ we bunched all the counts in each peak and using an exponential decaying fit estimated $G^{(2)}(\infty)$. Using this value we measured $g^{(2)}(0)$ of 0.12(2).	96
6.1 Optical set-up for demonstration of the collection efficiency of the 4th collimator on the γ chip. The focal length of this collimator is 59.6 <i>μm</i> . This collimator collect and collimates the ion beam. because of the short Rayleigh range of 8.7 and 5.1 <i>mm</i> (see section 4.3), this beam becomes divergent before exiting the vacuum chamber. The first 2 lenses are the the lenses that are used for external bulk optics imaging mode(see section 4.1). This part focuses the beam 172 <i>mm</i> after the second lens. A $f = 250$ <i>mm</i> lens is used to collimate the light again. A final telescope consists of a $f = 75\text{mm}$ and $f = 125\text{mm}$ resizes the beam and sends that to a PMT. In principle this complex optical set-up is not necessary for this experiment. The only reason that we used this set-up was that we wanted to use the same optical system for this experiment and the single mode coupling experiment. The iris is used to decrease the counts to 50% and reduce the polarization bluring effect. The polariser is used to filter unwanted σ photons and only let through π photons. This is necessary for single photon generation protocol(see section 5.3).	100
6.2 Optical set-up used for coupling ion fluorescence into the single mode fibre. The optical set-up collimates the ion light and resizes the beam to match it with the mode size of the fibre. An a-spheric lens couples the light into the single mode fibre.	103
6.3 Theoretical simulation of single mode coupling efficiency	106
7.1 Future work	108

CHAPTER 1

Introduction

In the early 1900s when quantum mechanics emerged, there was no implication that it might enter the realm of practical technologies [9]. It is only for a few decades that people started realising that this theory can be used to open ways for new technologies. Laser was one of the technologies that used an entirely quantum effect, stimulated emission. When in 1961 Maiman experimentally demonstrated the first laser[10], people called it a solution that is looking for an answer and today it is omnipresent everywhere from manufacturing sectors to our DVD-drives partly because of the reduction in manufacturing cost.

In 1982 Richard Feynman developed the idea of quantum computing when he found out that simulating quantum systems using classical resources is an intractable problem[11]. By this time experimental physicist had already started working on controlling individual quantum systems, like single atoms, for about a decade[12] but the main interest in the field arose after Shor's paper in 1994 on discrete logarithms and factoring [13]. This algorithm is particularly important because the the most widely used cryptographic system on the internet, RSA, is based on intractability of factoring a big number with classical computers. Shor showed that this quantum factoring algorithm has a polynomial complexity in the input number size ($O[\log(N)^2 \log(\log(N)) \log(\log(\log(N)))]$) while the complexity of the best known classical solution is sub-exponential ($O[e^{1.9\log(N)^{1/3} \log(\log(N))^{2/3}}]$). An estimate shows that this can reduce the time needed for factoring a 400-digit number from age of the universe to a few years [14].

Quantum physics doesn't only provide a solution to break the RSA encryption, It also provides a replacement. Quantum key distribution protocols like BB84 [15] enable us to share a secret key with a provably secure method, guaranteed by the laws of quantum mechanics.

To realise a quantum computing or communication protocol, one needs to be able to decouple a quantum system from the environment to prevent decoherence and at the same time have sufficient control over its evolution. There are many candidate qubits (quantum bits) for physical realisation of quantum computers; atoms, photons, charge in super conductors and quantum dots are among the platforms that has been used for quantum information processing. Photons are the most favourable option for quantum

networking and have very long decoherence times but when it comes to interaction and entanglement, practical implementation is challenging[16].

In 2000 DiVincenzo proposed a list of requirement that is needed for physical implementation of a quantum computer[17]:

1. Having a scalable well characterised qubit.
2. The ability to initialise a state.
3. Having long decoherence times.
4. Having a universal set of quantum gates
5. The ability to measure each qubit

He also proposed two extra conditions for quantum communication:

1. The ability to interconvert stationary and flying qubits.
2. The ability to faithfully transmit qubits between two locations.

Trapped atoms in ultra-high vacuum meets all the DiVincenzo conditions. The longest decoherence time demonstrated using atomic qubits is 50 seconds[18] which are orders of magnitude longer than the typical fast pulsed gates times which range from $1 - 10\mu s$ [19]. All the basic operations including qubit state preparation[20, 21], manipulation[22, 21] and readout[21, 23] have already been demonstrated. Gate error of the order of 10^{-4} has been realised[24]. Despite the fact that the gate errors are getting smaller, it is impossible to make them zero. Therefore we need a error correction scheme to compensate for the errors. It has been shown that the current error levels are sufficient for the implementation of these error correction schemes[25].

In 2004 Chiaverini *et al.* demonstrated an error correction scheme with one primary ion and two ancilla ions and showed that it is robust against spin flips [26]. There is also a proposal for error correction in trapped ion quantum computing that uses 5 ancilla ions and only needs global entangling operations[27].

Researchers have been able to demonstrate full quantum algorithms with trapped ions. Debnath *et al.* have demonstrated a programmable quantum computer module with 5 ion qubits[28] and Monz *et al.* demonstrated the first scalable Shor algorithm[29]. Grover's quantum search algorithm has also been demonstrated with trapped ions[30]. In 2007 Moehring *etal.* demonstrated the remote entanglement of two distant ions[31]. This has applications in quantum communication and distributed quantum computation.

Having demonstrated all the fundamental quantum gates with ions, scaling the number of qubits is the main technological obstacle now. The most widely used multi-qubit gate in trapped ion quantum computing are the Cirac-Zoller[32] and Molmer-Sorenson[33] gates.

These methods exploit the collective vibrational modes of the ions, arranged like a 1D crystal in a trap, as a quantum data bus to transfer the entanglement. These schemes are expected to be limited to tens of ions due to decoherence effects[34, 35]. The maximum number of ions entangled with this scheme is 14[36]. There are two main roadmaps to scale the number of qubits in ion based quantum computers.

One approach is the modular architecture which consists of multiple registers of ions [37]. In each register, ions interact locally through common motional modes. The limit on the number of ions in each register is imposed by decoherence effects[34, 35]. Entanglement between ions in different registers is completed via a probabilistic photonic interface[38].

Second proposition is using a quantum charge-coupled device[39]. In this device it is possible to shuttle ions to different regions of the trap. These regions are dedicated to different functions such as memory, interaction or sympathetic cooling. Sophisticated ion trap technologies that exist now, enable us to trap multiple ions and transport them individually[40, 41]. Successful transport of ions around different areas and through junctions has been demonstrated by different groups[42, 43, 44].

Optical interconnects play a crucial role in all the quantum information processing tasks with ions. These interconnect can be divided into two broad category of laser addressing and photon collecting optics. Laser addressing of individual ions is needed for different tasks including laser cooling, gate operations and state readout. Normal method of laser addressing is through using external bulk optics [45, 46]. Recently an integrated scalable scheme has been demonstrated for addressing of an ion qubit by researchers of Lincoln Laboratory at Massachusetts Institute of Technology[47]. Using lithography they fabricated nanophotonic waveguides that routes laser light and focuses that on an ion using focusing grating couplers. These waveguides are fully integrated into the substrate of a surface-electrode ion trap chip.

Trapped ions can make impeccable qubits. Qubits are encoded in two different atomic states. The reading process is accomplished through exciting the ion using specific laser frequency or polarization. Depending on the qubit state ion may start fluorescing or may not interact with laser. By detecting this fluorescence on a photon detector, one can measure the state of the qubit. The speed and reliability of the readout is directly proportional to the percentage of the fluorescence collected.

Conventionally the ion light is collected using bulk refractive optics placed outside of vacuum chamber. These optical components normally does not operate at high numerical aperture(NA) and therefore do not collect high percentage of ion light. To cover high NAs, these optics must have large diameters and this prevent them to be a candidate for collection light from high number of individual ions. Typical collection for these methods are between one to two percent collection. Most of the proof of the principle experiments in trapped ion quantum computing have been accomplished using these type of optical systems[48].

Using high finesse cavities is one of the methods to efficiently collect ion light[49, 50, 51]. Because the collected light is already in one optical mode, most of it can be coupled into a single mode fibre without the need for aberration correction. The drawback for this method is that micro fabrication and alignment of the cavity is extremely hard and it changes the properties of atomic transitions.

Bulk metallic spherical mirrors are one of the successful methods of ion fluorescence collection. Collection efficiency of 25% has been reported using these mirrors[52]. The problem with this method is that the collected light is hugely aberrated and without sophisticated aberration correction schemes it is not possible to efficiently couple that light into a single mode fibre. Single mode fibre coupling is necessary for many important applications like remote ion entanglement and quantum networking using ions. Micro spherical mirrors are also used in a surface ion trap and reported to improve the normal light collection by 1.9 times[53], but they suffer from the same aberration problem.

Collecting ion light into multi-mode fibre is another method of fluorescence collection. This method is good for ion state readout but not for many other applications that needs single-mode fibre coupling. Efficiency of 2.1% is reported in a surface ion trap by collecting ion light directly into a multi-mode fibre [54] while micro-fabricated diffractive lenses achieved coupling of 0.388% [55]. In an end-cap trap collection of 6% into two multi-mode fibre is reported [56].

In our group diffractive lenses were used for ion light collection[57], near diffraction limited imaging[58] and imaging of the shadow of a single atom[59]. In that project diffractive rings were patterned on a fused silica substrate to form a flat Fresnel lens with diameter of 5mm and focal length of 3mm. The lens was installed on a needle Paul trap in a vacuum chamber. Collection Efficiency of 4.2% was demonstrated.

In this project we designed and fabricated diffractive optics integrated into a surface Paul trap that can efficiently collect light and couple that into a single mode fibre. High resolution imaging is also demonstrated with these optics. These optics were manufactured by patterning diffraction rings on a chip substrate and then depositing the original aluminium electrodes and use them as collimating mirrors. The size of these mirrors is $80 \times 127 \mu m$ and their focal length is about $60 \mu m$. Using these mirrors we demonstrated 5.8(8)% ion fluorescence collection efficiency. The advantage of this scheme is that the design is scalable and it is monolithically integrated into the trap and regardless of its very small dimensions, it is capable of collecting a considerable amount of light.

In the process of demonstrating the mirror collection efficiency we developed and used an on-demand single photon generation protocol and demonstrated $g^{(2)}$ of 0.12(2). This shows that our generation scheme works in single photon regime and when measuring the mirror efficiency we know exactly how many photons we are generating. Comparing the detected photons with generated photons, we calculated the mirror collection efficiency.

Using this mirror, we captured a near diffraction limited image of the ion. The image

is 0.6% bigger than the diffraction limit in one axis and 4% bigger in the other. M^2 of this image is 1.36(9) and 1.54(9) for the two axes. To the best of my knowledge this is the highest resolution image taken of an ion without using corrective optics.

Free space light collection is important for ion state readout but many other applications in quantum information processing using ions need single-mode fibre coupling. This includes probabilistic entangling quantum gates[60], quantum teleportation[48], Bell Inequality Violation[61], Remote entanglement[31], ion light interference[62] and ion photon entanglement[63]. single mode fibre coupling is also specificity important for modular architecture and all the operations that needs remote ion-ion entanglement[31]. The best ion light single-mode fibre coupling efficiency reported is 1.4%[64]. We demonstrated coupling of 4.1(6)% of total ion light into a single-mode fibre. This is achieved using no corrective optics for aberration and the fluorescence beam just size-matched to the fibre mode.

In this thesis I describe design and fabrication of integrated diffractive mirrors implemented on a surface ion trap and explain the demonstration of its efficiency in light collection, Imaging and single-mode fibre coupling. Chapter 2 covers theoretical and practical aspects of trapping an ion and shuttling it to different regions of the trap. It also covers the design and fabrication process of integrated diffractive mirror. Chapter 3 describes the lasers we used for cooling and single photon generation. Chapter 3 explains imaging of the ion using external bulk optics for trapping and shuttling and diffraction limited imaging with integrated diffractive mirrors. Chapter 4 explains the single photon generation protocol that we used for demonstration of mirror efficiency and Chapter 5 is about demonstration of the performance of the mirror in free space light collection and single-mode fibre coupling and finally the conclusion chapter discusses the possibilities of improvement and possible future projects using this method.

CHAPTER 2

Integrated Diffractive Mirror Trap

To be able to use an ion as a reliable quantum particle, we need to keep it isolated from the environment. To do this we keep it in a vacuum chamber to prevent collisions with gas molecules. It also cannot be in contact with any other material in the vacuum chamber therefore we need to use some sort of electromagnetic potential to trap it. Because of the electric charge of the ion it is easy to apply a force on it using electric or magnetic field. The easiest configuration that comes to mind is using a static confining electric field that is confining in every direction but this is impossible due to Gauss's law. Gauss's law states that: the total of the electric flux out of a closed surface is equal to the charge enclosed divided by the permittivity.

$$\oint_S \vec{E} \cdot (\vec{dA}) = \frac{q}{\epsilon} \quad (2.1)$$

Where E is the electric field, dA is a surface element on a closed surface, q is the electric charge inside the closed surface and ϵ is the medium permittivity. This means that if we have an electric field that is pointing towards a certain point in every direction, There must be a electric charge inside that volume to make it possible.

There are two common solutions for this problem: Penning trap and Paul RF trap. In Penning trap a uniform magnetic field is applied along the z axis. In the xy plane, when the electric charge tries to leave the trapping area, the magnetic field turns the direction of its speed and force that to rotate with cyclotron frequency. Adding an inhomogeneous electric quadrupole field to this magnetic field, confines the ion to a certain position. In our experiment we use a Paul RF trap in an ultra-high vacuum chamber. This trap does not use magnetic field. Instead it uses a DC field in combination with an alternating RF field to confine the ion. The trapping mechanism of this trap will be discussed in detail in the following sections.

2.1 Paul RF Trap

Paul RF trap uses an alternating electric field (RF field) to confine the ion. Depending on configuration it can confine the ion in 3 dimensions but in most configurations it

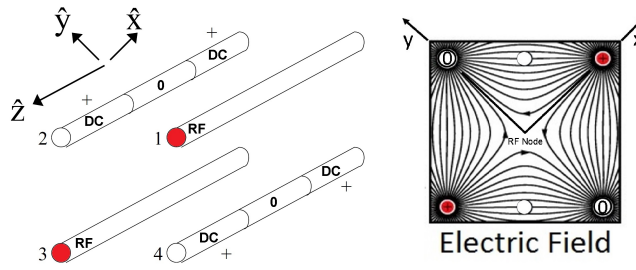


Figure 2.1: A four rod conventional Paul trap. Two RF electrodes labelled 1 and 3 and two segmented DC electrodes labelled 2 and 4 that are grounded in the middle and held at a positive potential at the end segments (Left) and RF electric field (Right) (Field image after [1])

confines the ion in two dimensions and needs an extra DC field to confine the ion in three dimensions. Fig. 2.1 shows a conventional layout of a linear Paul trap. This trap consists of two parallel rods connected to an RF potential (electrodes with the red dots) and two segmented DC rods that are grounded in the middle but have positive voltage at the end parts. Right side of the Fig. 2.1 shows the RF field created by this setup during the period that RF potential is positive. When RF potential switches to negative, we have the same pattern but with reverse electric fields. Looking at the direction of electric field it is evident that when RF potential is positive, the field is confining along the x axis but it is outward along the y axis. When the sign of RF potential changes, the field becomes confining along the y direction. Solving the exact equation of motion given current potential shows that -for some given RF frequency and amplitude- this field keeps the ion at the RF node.

Given a RF voltage on red electrodes $V_0 \cos(\Omega t)$ (Ω is the RF drive frequency) and DC voltages on the end parts U_0 , the quadrupole potential is [65] :

$$\phi(\vec{x}, \vec{y}, \vec{z}, t) = \frac{\kappa_{RF} V_0 \cos \Omega t}{2r_0^2} (x^2 - y^2) + \frac{\kappa_{DC} U_0}{r_0^2} \left(z^2 - \frac{\epsilon_{DC} x^2 + (1 - \epsilon_{DC}) y^2}{2} \right) \quad (2.2)$$

Where r_0 is the distance between RF electrodes and κ_{RF} , κ_{DC} and ϵ_{DC} are dimensionless geometric constants that provide scaling and ellipticity to the electric potential. In reality the potential have higher order quadrupole terms but as long as ion displacement from the RF node is much smaller than the distance between the RF electrodes, the potential above is a good approximation.

The equation of motion for a particle in an electric potential is:

$$m \frac{d^2 \vec{r}}{dt^2} = -Q \nabla \phi(x, y, z, t) \quad (2.3)$$

Inserting the potential from the equation 2.2 and rearranging and separating the vari-

ables we arrive at the equation below for the x direction:

$$\frac{d^2\vec{u}}{d\xi^2} + (a - 2q\cos 2\xi)\vec{u} = 0 \quad (2.4)$$

Where:

$$\xi = \Omega t / 2 \quad (2.5)$$

$$a = \frac{4eU_0\epsilon_{DC}\kappa_{DC}}{m\Omega^2 r_0^2} \quad (2.6)$$

$$q = \frac{2e\kappa_{RF}V_0}{m\Omega^2 r_0^2} \quad (2.7)$$

This form of differential equation is called Matthew equation. This form is common in many problems like solving wave motion in periodic media. For this type of periodic equations we can apply Floquet's theorem and use functions with the form below to find the solutions:

$$x(\xi) \propto e^{\pm i\beta\xi} f(\xi) \quad (2.8)$$

With $f(\xi + \pi) = f(\xi)$. When $\beta = \beta(a, q)$ is real, the ion motion is stable for $|a| < q^2 \ll 1$ [2]. Expanding for small values of a and q we find:

$$x(\xi) \approx x_0 e^{i\beta(\xi - \xi_0)} \left(1 + \frac{q \sin(2\xi)}{2} \right) \quad (2.9)$$

$$\beta \approx \left(a + \frac{1}{2}q^2 \right)^{1/2} \quad (2.10)$$

ξ_0 is a constant phase. Looking at the term outside the brackets in eq. 2.9, this solution can be interpreted as a periodic motion with angular frequency of β that is being modulated by the periodic term in the brackets with angular frequency of Ω_{RF} . The first term is called secular motion and the second term is called micromotion.

In reality stray electric fields will be present at the trapping site. This can happen for example if insulating parts of the trap become charged. This field applies a constant force that displaces the ion from the center of the trap. For a doppler cooled ion this displacement can be small enough to ignore the spatial variation of RF field therefore ion will have the same secular motion. On the other hand the change in the micromotion term is big. If we add the electric force imposed on ion by the stray electric field to the equation 2.3, the solution of the equation will be:

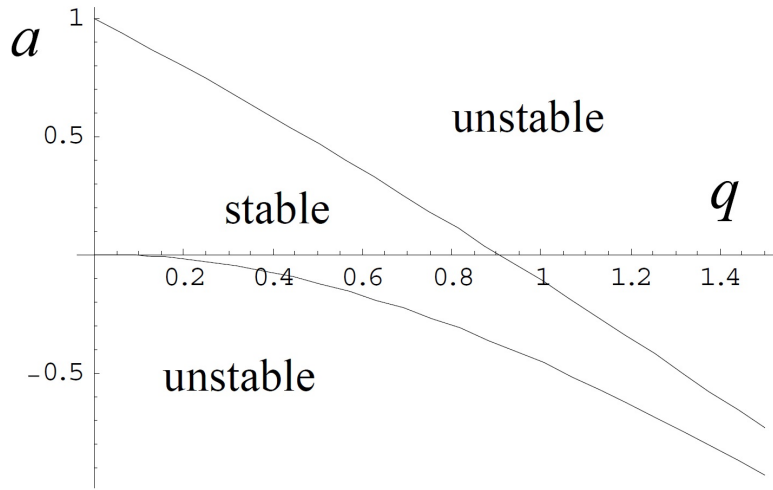


Figure 2.2: Stability diagram for different values of a and q . The area in the middle is stable but the areas on top and bottom are unstable regions. (Fig. after [2])

$$x(\xi) \approx x_0 e^{i\beta(\xi-\xi_0)} + x_1 \left(1 + \frac{q \sin(2\xi)}{2} \right) \quad (2.11)$$

Where $x_1 = 4QE/m\omega^2$ is the displacement, Q is the electric charge of the ion and E is the electric field. Amplitude of a Doppler cooled ion is usually less than 100 nm therefore even a small stray electric field as small as $100V/m$ can significantly increase this amplitude.

Depending on the trap depth (determined by RF drive amplitude and frequency) it may eject the ion from the trapping potential. To prevent the loss of ion and keeping it as cool as possible, traps have DC electrodes that can generate a field along x and y direction to cancel the stray fields. These DC electrodes are also used to move the ion along the 1D RF node.

Fig. 2.2 shows the stability condition for different values of a and q . In atomic ion trapping typically $q \approx 0.1$ is used and $q = 0.3$ is the highest that rarely used. For cooling purposes high secular frequencies are desirable. To achieve higher secular frequencies we need to decrease Ω_{RF} while keeping a and q constant. Keeping a and q fixed becomes possible if we keep the value $V_0\Omega_{RF}$ constant and this means that we need to increase RF amplitude V_0 . The maximum amplitude achievable is usually limited by breakdown voltage which depends on electrodes configuration, RF electrode's material roughness, pressure of the chamber and how clean electrodes are.

In our surface Paul trap shown in Fig. 2.3 the DC and RF electrodes are all in the same plane. As it is shown in the left side of the Fig., the trap has two flat RF electrodes

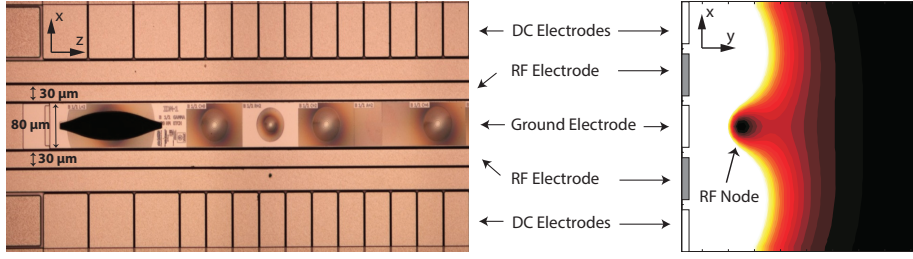


Figure 2.3: Microscope image of the Integrated Diffractive Mirror Trap (Left). Middle ground electrode is $80\mu m$ wide and RF electrodes are $30\mu m$ wide. Segmented parts at the top and the bottom of the image are Control DC electrodes. Right image is a schematic of RF electric field that creates a RF node on top of the trap. (Field image after [3])

and one ground electrode between them that stretch along the trap. The width of the RF electrodes are $30\mu m$ and the width of the ground electrode is $80\mu m$. This creates an RF node $58.6\mu m$ above the surface (As shown in the right side of the Fig. 2.3). Even though the field is asymmetric, near the RF node it can be approximated by to first order as a quadratic potential discussed above. This RF field confines the ion in the xy plane. In the z direction ion can be confined by using DC electrode shown at the top and bottom of the microscope image. For our trap Poisson's equation is used to find the voltages needed to create a confining harmonic potential along the z axis. If we gradually move the center of this filed to another position, ion will be shuttled to that position. Other than confining and shuttling, DC electrodes can provide a constant electric field along x, y or z axis to cancel the stray electric field. There are also two long DC electrodes that can create an asymmetry that is used to slightly rotate the RF axis to make cooling possible for a laser beam parallel to the surface (For detailed discussion for the cooling process refer to 3.4).

Trap secular frequencies depend on both RF and DC potentials but we can ignore DC potentials to calculate an approximate value for the trap frequencies for directions perpendicular to the RF axis.(Refer to the trap manual provided by GTRI [4]). Neglecting DC potentials, The approximate quadrupole RF potential is:

$$\phi = \frac{V_0 \cos(\Omega_{RF} t)}{2} \frac{x^2 - y^2}{R^2} \quad (2.12)$$

Where x and y are the radial coordinates aligned with the RF quadrupole, V_0 is the RF amplitude, Ω_{RF} is the RF angular frequency, and R is a geometric factor of the trap. For this trap R is $133\mu m$ in loading zone and $142\mu m$ outside the loading zone. For the potential above the radial angular frequency is degenerate and is equal to:

$$\omega = \frac{QV_0}{\sqrt{2}\Omega_{RF} m R^2} \quad (2.13)$$

Where Q is the ion charge and m is the ion mass. To increase the secular frequency

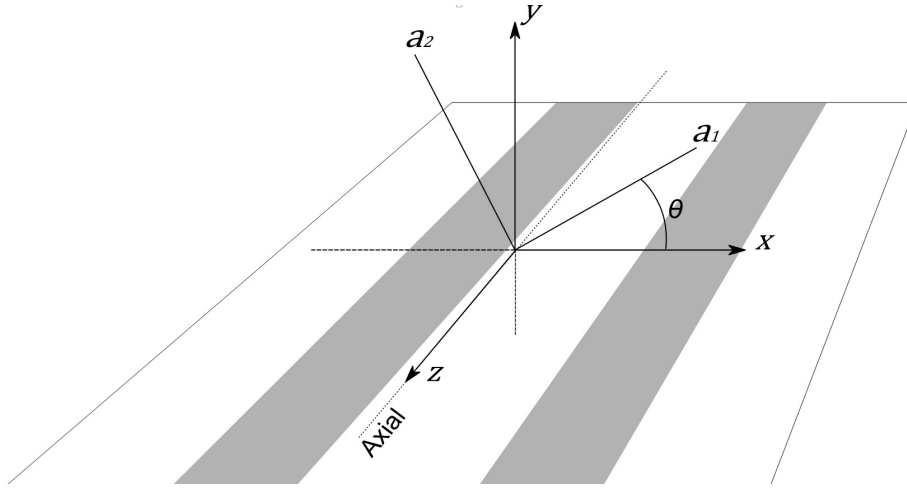


Figure 2.4: Rotated coordinate system describing the DC quadrupole. (Fig. from [4])

it is possible to increase the RF amplitude but this value is limited by RF breakdown voltage for the $4\mu m$ gap between the RF electrodes and the ground electrode. For the the RF frequencies that we use($26 - 29 MHz$), this break down voltage is $250V$. We keep this voltage below $200V$ in our normal operations.

To take into account the axial confinement and frequency asymmetry for the two RF axis, we can use parameters ω_z for axial confinement and $\Delta\omega$ for frequency splitting. with these parameters the secular mode frequencies will be:

$$\omega_1 = \sqrt{\Omega_{RF}^2 - (\omega_z^2 + \Delta\omega^2)/2} \quad (2.14)$$

$$\omega_2 = \sqrt{\Omega_{RF}^2 - (\omega_z^2 - \Delta\omega^2)/2} \quad (2.15)$$

If RF axes are rotated (Fig. 2.4), by creating asymmetry using two long DC electrodes, the frequencies ω_1 and ω_2 will be aligned with the rotated axis a_1 and a_2 . This is only valid when ion is close to the RF node. Away from the node anharmonic terms appears that removes radial degeneracy from pseudopotential ϕ and introduces additional terms. In surface traps these anharmonic terms are large and stray fields that push the ion away from the RF node can change radial frequencies by a large amount.

2.2 GTRI Microwave I Trap

The ion trap that is used in this project is a modified version of the GTRI(Georgia Tech Research Institute) Microwave I ion trap. We modified the trap by adding diffractive mirrors to the middle ground electrode. This modification does not have an effect on the

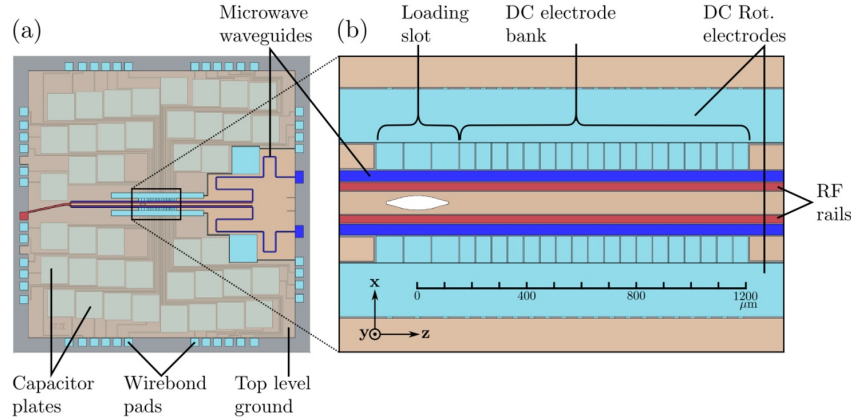


Figure 2.5: A schematic of the 11x11 mm² silicon chip (a) and the active trapping region (b), showing RF and DC trapping electrodes, capacitive RF filters, the shaped loading slot, and the on-chip microwave waveguides. (Image after [4])

trapping functionality of the chip. In this section we explain the unmodified trap and the diffractive mirrors are discussed in section 2.3. GTRI Microwave I ion trap is specificity designed for quantum information processing tasks. It is a flat surface trap and ion sits 58.6 μm above the surface.

This chip trap includes two waveguides (Fig. 2.6b) along the trap axis that produce a polarization-tunable standing microwave field for global addressing of $^{171}Yb^+$ hyperfine qubits. Two Corning Gilbert A010-L34-02 GPO microwave connectors shown in Fig. 2.6 c are the inputs for these waveguides. These input are connected to SMA microwave vacuum feedthroughs via The Accu-Glass in-vacuum coaxial lines. Using these inputs a A 12.6 GHz microwave field can be supplied to drive $^{171}Yb^+$ hyperfine levels. These hyperfine levels are usually used to encode a qubit.

In this trap photoelectrons, generated by UV laser hitting the metal parts of the trap, can easily charge the exposed insulating substrate between the electrodes. Voltages created by this effect can be so large that can make it impossible to counter them with DC electrodes. This can create large micromotion that can eject the ion from the trap. To reduce this effect The trap has an integrated grounded shield outside of the active region (Fig. 2.6c). This part consist of a flat metal part on the sides and a metallic mesh on top of the trapping area to provide optical access. Existence of this shield also simplifies the fields created by control electrodes. This shield is placed a few millimetres above the chip surface to provide laser access parallel to the surface. Because this shield is shorted to trap ground, it cannot be used as a DC electrode or driven by a RF voltage for trap frequency measurements.

The trap has built-in capacitors around the trapping area (Fig. 2.5a) to reduce RF

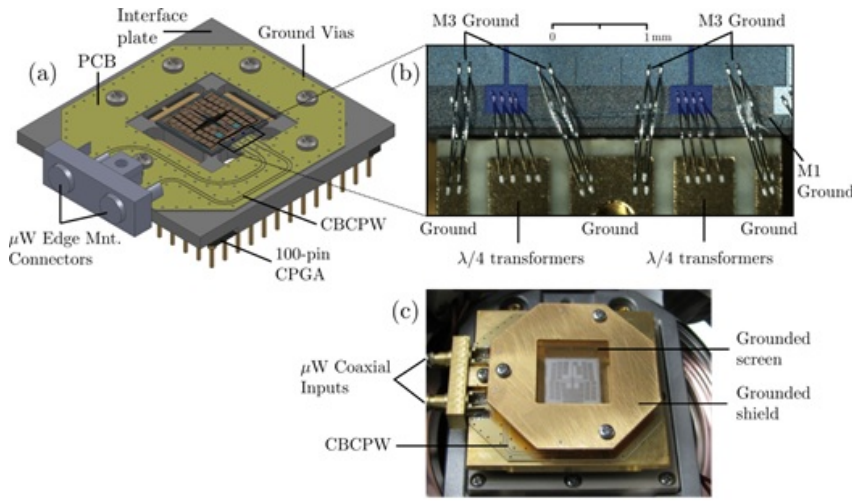


Figure 2.6: Trap components including a packaged device with top screen removed for clarity (a), a photograph of the wirebond interface (b), and a photograph of a fully installed device with microwave connections (c). (Image after [4])

pickup on the control electrodes. Along the trap axis there are 21 pairs of DC electrodes to enable shuttling. For radial micromotion nulling and rotation of principal motional axes it uses 2 large control electrodes along the entire trap axis. These long electrodes can also be connected to an oscillating source to perform mode frequency measurements. In this test the oscillating voltage creates an oscillating field at the ion and this excites motion when tuned close to resonance with a normal mode. In this chip light access to the ion is along the axial direction and along both of the 45° diagonals. In our set-up, we do not have a window along the axial direction and only use the two 45° diagonals.

the chip carrier, which the chip trap is mounted on, has 98 pins on the bottom part(many of them are unused or redundant) and sits on a socket which is connected to a number of in-vacuum DC cables and through them to four Accu-Glass 100220 DB25 vacuum feed-troughs. The pins must be shielded from the neutral atom source(section 2.4) to prevent Yb deposition and shorting.

This trap is designed to work in ultra-high vacuum and operating at atmospheric pressure can lead to sparking between the electrodes. This is because the border between the electrodes are narrow ($2\text{-}9 \mu\text{m}$)and therefore the RF breakdown voltage is only 1V operating at normal pressure while it is 250V in ultra-high vacuum. If voltages higher than breakdown voltage is applied, localised discharges start and if operated for long hours erode the RF electrode and makes the trap inoperable. This happened in this project due to inaccuracy of RF voltage pick-off that we used to monitor RF voltage and we had to replace the trap with a new one.

The chip area is approximately 1.1 cm^2 and it is $500 \mu\text{m}$ thick. It is made of 5 alternate

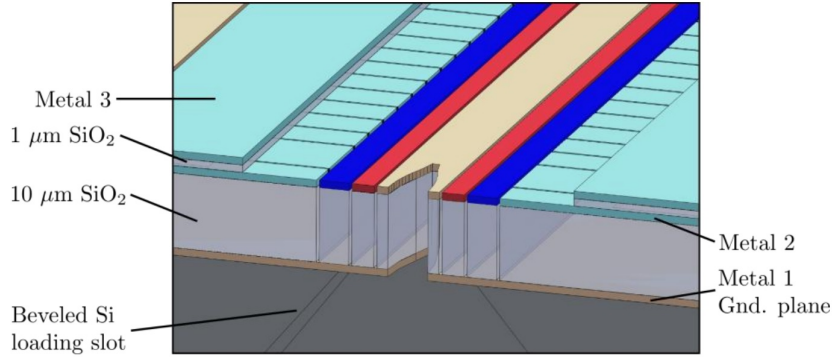


Figure 2.7: A cross section showing internal layers of the Microwave I Chip (the vertical direction is scaled by 10x for visual clarity). (Image after [4])

aluminium and silicon dioxide layers on top of a Si substrate (Fig. 2.7). The bottom metal layer M1 is $1\mu m$ thick and Shields RF field from hi-loss Si substrate. On top of M1 there is a $10\mu m$ Silicon dioxide layer which creates a substrate for second metal layer M2. M2 is where the capacitors are placed. On top of M2 sits a $1-2\mu m$ silicon dioxide layer and on top of that comes the third metal layer M3 with the thickness of $1\mu m$. This layer is grounded and restricts the portion of the DC electrodes that influences ion. It also protects DC electrodes and capacitors in M2 from damage.

2.2.1 DC Electrodes Voltage Control and Shuttling

The electrode structure of the trap is shown in Fig. 2.8. The trap has two long DC electrodes 5 and 6 along the trap axis, array of 21 pairs of DC electrodes, Microwave rail, RF electrodes that stretches along the trap axis, and the middle ground electrode. The rest of the metals in this area and around it are grounded. DC pairs around loading zone are roughly $100\mu m$ wide and rest of the pairs are $80\mu m$ wide for better precision in ion shuttling and positioning. The width of the middle ground electrode that stretches along the trap axis is $80\mu m$. In the modified trap, optics are patterned on this electrode and width of this electrode defines the width of these optics. The white oval shaped cut between electrode 9 and 10 is the loading zone hole. Neutral atom oven(section 2.4) is placed under this hole. After trapping, ion appears at the center of this region. At this point ion height is $52\mu m$ but when it leaves the loading region the height becomes $58.6\mu m$.

DC electrodes are connected to the voltage controllers through four DB25 feed-troughs. The map between DC electrodes and DB25 pins is provided in the trap manual[4]. A National Instruments PXI-1044 14-slot chassis with 12 NI PXI-4713 cards controls the DC voltages. This device can apply -10 to +10V. GTRI provided us with a 2X amplifier to increase the voltage range to -20 to +20V. To apply the voltages properly it is important

that DC and RF controllers have a common ground.

DC electrodes are used for different functionalities. This includes generating longitudinal, lateral and vertical DC compensation voltages, Rotating Principal RF axes and generating harmonic potential along the trap axis. The harmonic voltage confines the ion along the trap axis where RF trapping potential does not confine it. By moving the center of this harmonic potential we can shuttle the ion along the trap axis.

GTRI team use a Poisson solver software for each of the above functionalities to determine the voltage for each DC electrodes. Set of files named waveforms are provided by GTRI for each of these functionalities. These are comma separated value (CSV) files in the following format:

Position	DC_{05}	DC_{06}	...
i_1	$U_{05}(i_1)$	$U_{06}(i_1)$...
i_2	$U_{05}(i_2)$	$U_{06}(i_2)$...
i_3	$U_{05}(i_3)$	$U_{06}(i_3)$...
...

Each file specifically determines the voltage for each of the DC electrodes for a given functionality at a given ion position along the z axis. Since Poisson equation is a linear equation, to scale the electric field created by these waveforms, we can simply scale all the individual voltages by the same amount. If we need to use different waveforms at the same time the linearity allows us to simply add them together. For the stray field compensation voltages, applying a waveform is equivalent to applying electric field of 1000V/m to the ion. One can scale these voltages by multiplying a scalar weight to all the electrode voltages in the waveform table.

I used LabVIEW(tm) to develop a program that has a user interface that enables user to input the file path for all the waveform files and the scalar weights associated to them. An input is provided for user to choose the accuracy in position down to 100nm. The accuracy provided in the waveform files is $6\mu m$. Program uses a linear interpolation to find the middle values for the desired accuracy.

In the next step, the software multiplies the electrode voltages by the weights given by user to scale them and add them together. The user is allowed to opt between fixed or position dependent weight. The fixed weight option uses one scalar weight provided by user for all positions. If position dependent weight is selected, an CSV file must be provided by the user that contains some arbitrary positions and the weight associated to them. The program uses a linear interpolation to calculate the weight for the positions not given in the file.

This functionality helped us to solve the problem of shuttling the ion over certain problematic locations of the trap. We had the problem of losing the ion at these points. One of the points was where the ion leaves the oval shaped loading area. The borders

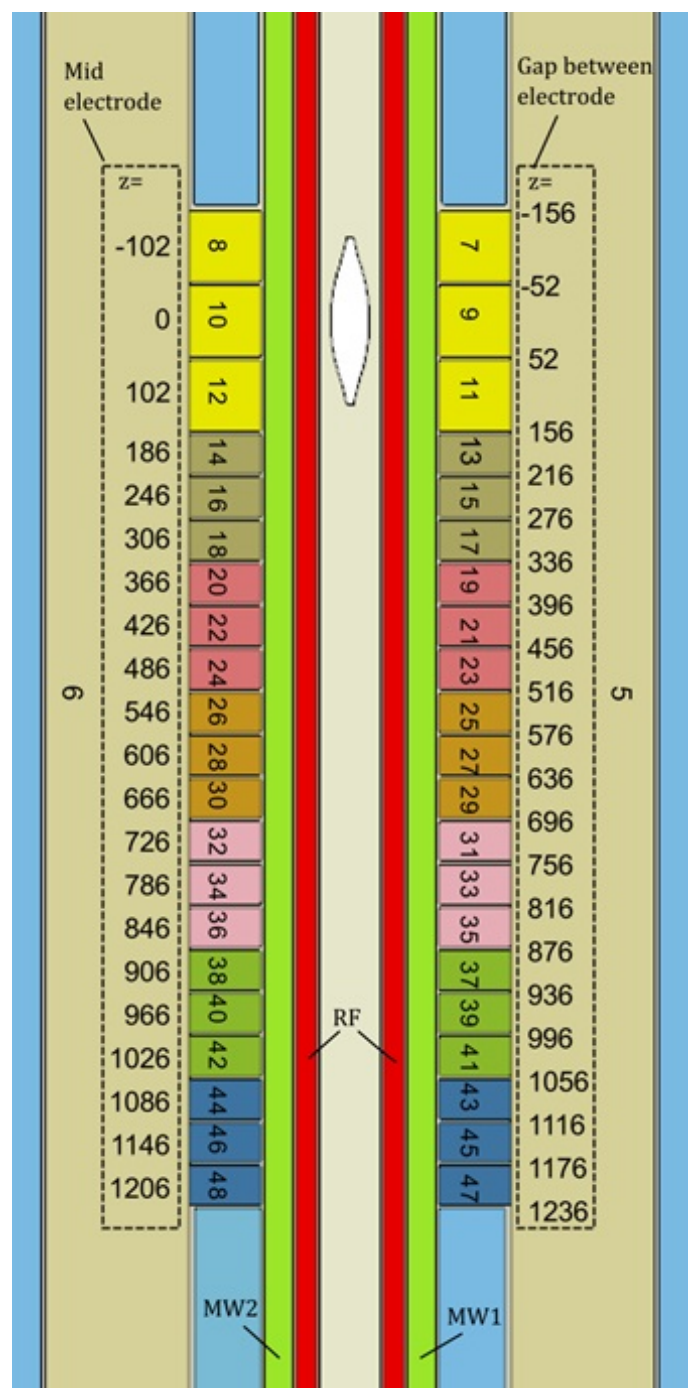


Figure 2.8: Dimensions and electrode IDs of the trapping region for a Microwave I trap. The z coordinates along the length of the trap correspond to the ion positions relative to the loading position. (Image after [4])

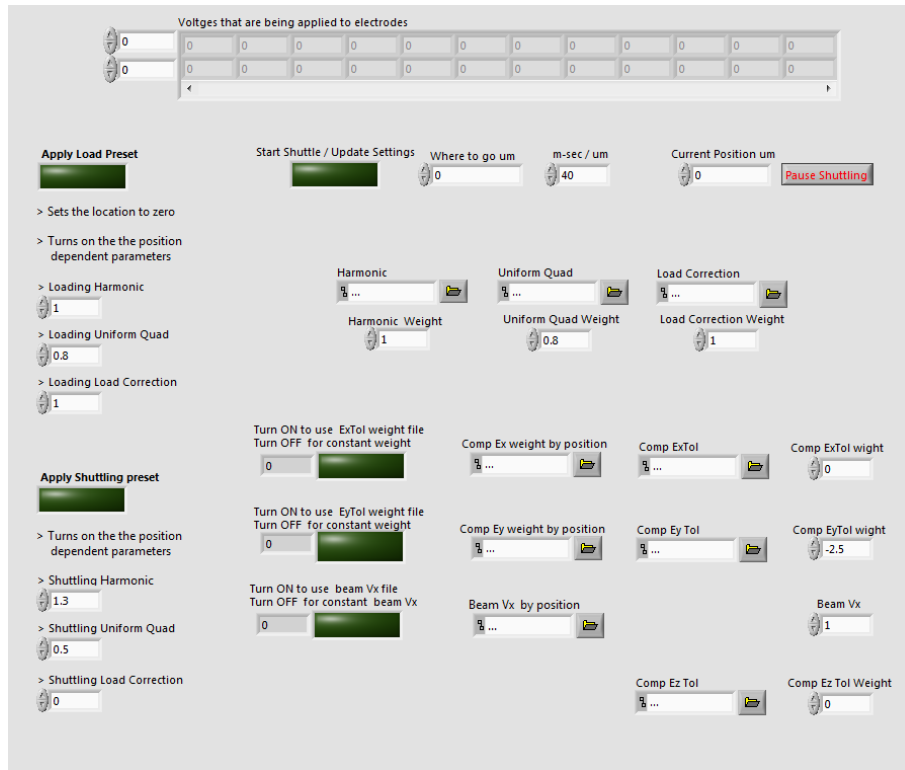


Figure 2.9: Screenshot of Labview program interface for controlling DC electrodes for shuttling and applying compensation fields. On the top program displays the voltages that are currently being applied to the electrodes. Below that user can enter a destination in the "Where to go um" field and a speed in "m-sec /um" and start shuttling using the button "Start Shuttle / Update setting" to the lft of those. The input fields at the bottom allow user to choosa file for each waveform and selct between constant weight or postion dependent weight. Left inputs are used to save two presets for loading and shuttling and apply them whit a click of a button when needed.

between the optics were also problematic. We realised that the stray field, that ion feels, varies very fast near these points. To compensate for these fields and reduce micro-motion and ion heating, I added to the program a capability to accept position dependent weights for each DC compensation waveform and vary that dynamically while shuttling. We mapped the compensation voltages for every $25\mu m$ and saved it in an input file for the program. That modification together with using stronger harmonic DC potential solved the shuttling problem.

Fig. 2.9 shows a screen shot of the user interface of the program. To shuttle the ion around, the program gets a destination in μm from the loading spot and a speed of shuttling. Using current position, destination, accuracy and speed program calculates the number of steps and the time for each step. applying the calculated number of steps and the delay needed for each step, It smoothly moves the ion to the destination.

In this procedure lasers must also track the ion position. We use a fast steering mirror that is controlled by a DAC(Digital-to-Analog Converter) system. We measure the x and y voltage needed to position laser at the loading zone ($0\mu m$) with the right height and at the end of the trap ($1086\mu m$) with the right height. For the rest of the positions the program uses a linear interpolation to calculate the voltages. User is also allowed to provide a position dependent file for slight modification of laser positioning.

The program allows user to save two preset lists for trapping and shuttling. By click of a button, the program changes all the parameters to the saved values to make voltages ready for trapping a new ion or shuttling it around.

After two years of using the same trap we again started losing the ion at the point where it leaves the loading zone. Apparently this problem occurs when neutral atoms deposit on the back side of the trap and this changes the electric field around the loading zone. We solved this problem by applying a strong upward electric field in the loading zone and gradually reducing it to zero at $200\mu m$ away from loading point. Based on GTRI researchers' experience this problem is common but usually solved by using a strong downward electric field.

2.2.2 RF Electrodes and RF Voltage Generation

This trap needs a RF voltage between 80-200 volts and frequency of 25-30 MHz for trapping. To supply this RF voltage we use a HP 8647 RF generator that runs at 8dbm and the output goes through a -29db attenuator and being fed into a 40 dB, 10 W high power RF amplifier. The attenuator is used to make sure that even when the maximum power on the generator is used, the voltage remains below 200V. The output of the amplifier goes to the antenna of the a helical resonator shown in Fig. 2.10 . This antenna induces an RF voltage on the inner coil which goes to the chip.

The Helical resonator acts as a transformer to keep to keep the supplied RF power to a minimum. It consists of a copper cylinder that houses an antenna and a coil and a capacitive divider. RF source is connected to the antenna and induces a voltage on the coil. The outer cylinder is a copper tube that was sand blasted to remove contaminations. A BNC plug mounted on a adjustable lid is the input to this resonator and is connected to an aluminium antenna. Inner coil is made of copper wire and is connected to the grounded housing tube from one side and to the vacuum RF feedthrough from the other side. The adjustable lid is used to find the optimum position for the antenna to reach maximum coupling. The coupling efficiency is optimised by minimising the amount of RF back reflection. Changing the position of the antenna changes the resonant frequency therefore the antenna position and RF frequency must be changed iteratively to reach the optimum coupling.

The design of the resonator is based on the design and equations in [66]. For a desired

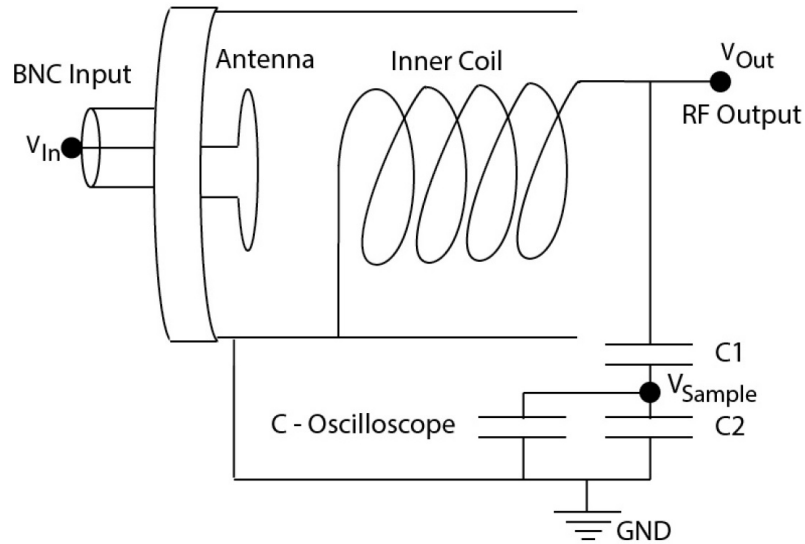


Figure 2.10: Schematic of the helical resonator used for RF input of the trap (Image courtesy of Valdis Blums)

resonant frequency, quality factor and resonator length, the equations determine number of turns, coil length, winding pitch, and the sizes of all the other conducting components. For a given resonant frequency, These designs can reach quality factors of a few hundreds to a thousand in a compact resonator. Capacitive load affects the resonant frequency and quality factor. To replicate the real capacitive load we used a bare vacuum feedthrough during the tests of coupling efficiency and quality factor. This lacks the capacitance of the chip itself therefore the final test numbers are slightly different from the operating values at the trap. The length of the inner coil is the main parameter that we change to achieve the desired resonant frequency. The test quality factor for our resonator was 95 but when it is attached to the trap the quality factor drops to 80. The resonant frequency for the test condition is 27.1 MHz and it is 25.7 MHz when it is connected to the trap.

The helical resonator for the chip trap includes a capacitive divider that is used for monitoring the trap RF voltage. The ratio of capacitance in this divider is 200:1 but the practical voltage ratio is 530:1. Our experience shows that this ratio changes dramatically with slight changes in position of components of helical resonator so care must be taken in measuring a reliable ratio. These changes in the reading is because of parasitic capacitance and inductance. We read 0.15V peak to peak from the monitoring output therefore we are applying 80V peak to peak to the trap RF electrodes. There was a worry that the nano-structuring of the ground electrode for the new optics may lower the RF breakdown voltage but apparently it is the same as the standard trap.

2.3 Diffractive Mirrors

Currently all the basic tasks of quantum information processing with ions have been demonstrated with limited number of ions[28, 29]. The highest number of entangled photons created has been only 14 [36]. This number is theoretically limited to hundreds of ions[34]. Spontaneous decay, laser phase coherence and ion heating are among the factors that limit this number[35]. The future of this field depends on scaling the number of ion qubits under control and that is why recently the interest of people turned into micro-fabrication of ion trap technologies. Now that the Micro-fabricated trapping side of the technology is well advanced[41], the effort of ion-trap community is focused on scalable optical interfaces. Scalability in this context is the ability to increase the number of ions and optics without affecting the performance of the optics and without adding too much technical complexity.

Light collection efficiency directly impacts the time needed for read-out and remote ion entanglement. To collect maximum amount of light the optic must cover large fraction of total solid angle around the ion. As an example, in a collaborating project between Massachusetts Institute of Technology and Max Planck Institutes, researchers manufactured a trap with a built in spherical mirror that covers 80% of the solid angle. To scale the number of ions, the prospect is to have the ion density of about one ion in every 100 μm . With this size the only way to cover more than 10% solid angle is to place the optic at a distance smaller than 100 μm to the ion. If we place a dielectric optic this close to the ion, charging from photo-ionisation starts to build up on the optic very quickly and makes trapping impossible. Transparent conductor coating is a solution for this problem but might not be practical for all designs. The problem with metal optics, if they are not part of the trap, is that they change the trapping field configuration. Integrated mirrors do not have any of these problems because they are integrated into the original electrodes of the trap. They also do not restrict optical access of the trap. These characteristics enable us to increase optics density beyond any other competing technology. This design does not need optical alignment and is robust against thermo-mechanical movement and stress during bake-out. The fabrication process uses standard lithography and is robust against ion trap bakeout. The performance of these optics is comparable to advanced non-scalable technologies.

To demonstrate the quality of the imaging with these optics, we showed that a large fraction of the collected light can be coupled to the single mode fibre. Single mode fibre coupling of the ion light is important for remote entanglement and quantum communication. Single mode fibre coupling efficiency η_{SM} depends both on free space collection efficiency η and beam quality M^2 . A rough estimate is that $\eta_{SM} = \eta/M^2$. We demonstrate that the light collected with these optics have M^2 values close to one and large percentage of the light can be coupled into a single mode fibre without any aberration

correction. In chapter 6 we demonstrate that we can couple 71(5)% of the collected light into the single mode fibre which is equivalent to coupling of 4.1(6)% of the total ion light into the single mode fibre.

As another method to demonstrate the imaging quality, we showed that images captured with the diffractive mirrors are close to the diffraction limit(section 4.4) and this another reason why they are ideal for single mode fibre coupling4.3.

To manufacture integrated diffractive mirrors, a joint project were defined between our team at Griffith University and Quantum Information Systems group at the Georgia Tech Research Institute (GTRI). The project were funded by Intelligence Advanced Research Projects Activity (IARPA), Griffith University and Australian Government. M. Ferstl at the Heinrich-Hertz-Institut of the Fraunhofer-Institut fur Nachrichtentechnik in Germany performed the the step that needed electron lithography.

2.3.1 Theory of Diffractive Mirrors

A collimated beam has a flat phase front. What a conventional focusing curved mirror does is that it focuses the light by changing the phase front of a beam so that different parts of the beam be in phase at our desired focus point. This phase shift can be written in the form $2n\pi + \Delta\phi$. Here $\Delta\phi$ is between 0 and 2π . n might be different at different positions but it does not have an effect on the focusing procedure. In design of diffractive mirrors we set n to zero and impose periodic $\Delta\phi$ from 0 to 2π .

When a beam reaches the focus point from an off-axis distance r (Fig. 2.11) it has travelled a distance equal to $\sqrt{r^2 + f^2}$ (f is the focal length). Thus the phase difference between the on-axis beam and this beam is:

$$\Delta\phi = \left(\frac{\sqrt{r^2 + f^2} - f}{\lambda}\right)(2\pi) \quad (2.16)$$

We need to change the path length to eliminate this phase difference. If $\Delta\phi$ is greater than 2π we can deduce multiples of 2π from the phase shift without changing the effect of phase shift (or equivalently if difference in path length is greater than λ we can deduce whole λ s from the path length difference). To eliminate this phase difference and make beams in phase at focus, we can increase the height by $\Delta h = \sqrt{r^2 + f^2} - f$ at r (This must be done by deducing multiples of λ when Δh is grater than λ). This means that at radii associated with 2π phase difference, height starts at zero and increases to λ at the next radius associated with 2π phase shift and then drops abruptly to zero and continue increasing upto the next ring. These rings are located at:

$$r = \sqrt{2n\lambda f + n^2\lambda^2} \quad (2.17)$$

This creates a pattern shown in Fig. 2.11. In practice it is hard to fabricate this

smooth pattern but in the small angle limit where scalar diffraction approximation is valid, approximating the continuous pattern even with two levels can lead to about 30% diffraction efficiency and 4 level approximation can increase the efficiency up to 70%.

In our group we have used Fresnel lenses to collect ion [?]. The advantage of our new method of using mirrors is that for moderate NA's (< 0.5 NA) maintaining high diffraction efficiency is much easier with mirrors. Interference effects lowers the diffraction efficiency at moderate angles in diffractive lenses. This effect is absent in diffractive mirrors. For mirrors with high Na's (> 0.5 NA), the scalar approximation is not valid any more and vector diffraction must be used. In this regime, the reduction in phase contrast for step profile reduces the diffraction efficiency to a considerable amount. However it is possible to optimize the profile, using a vecotr method, to maintain diffraction efficiency of 95% even for solid angle coverage near 50%[67].

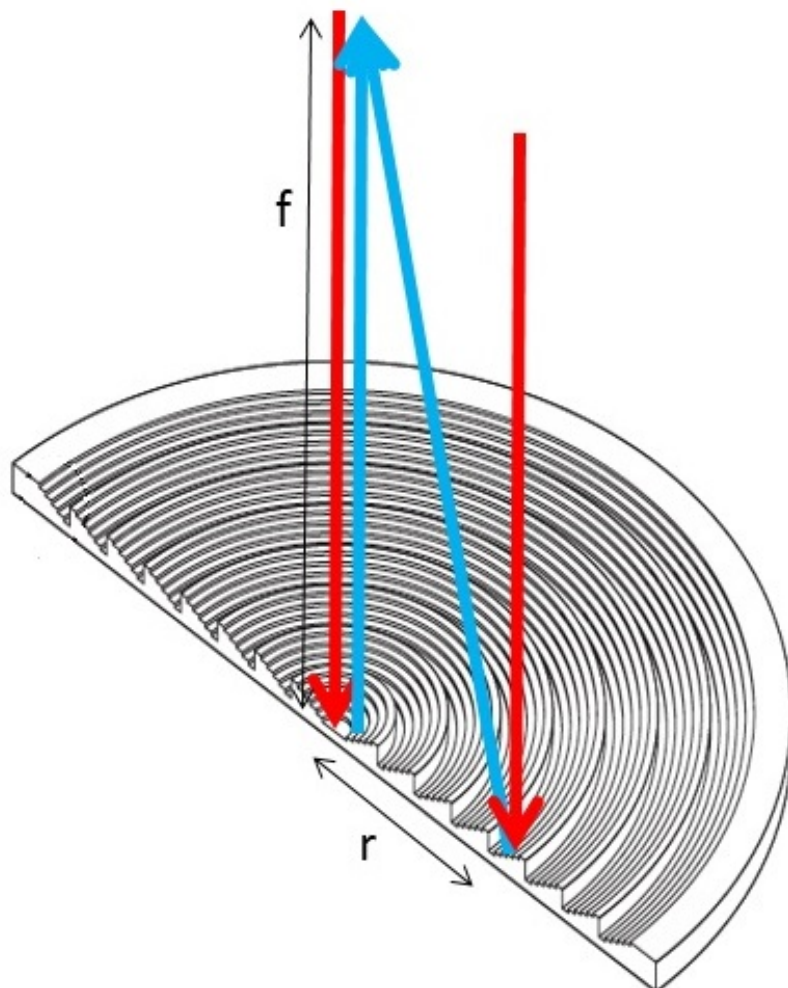


Figure 2.11: A Fresnel mirror with 2π cycles. Red arrows are incoming beams at the centre and at the offaxis distance r . Blue arrows are reflected beams that both go to the focal point (Fresnel mirror image taken from Tech Briefs Solutions website techbriefs.com)

2.3.2 Design of Diffractive Mirrors

In this project we integrated diffractive mirrors into the middle ground electrode of the Microwave I trap. Fig. 2.12 Shows a microscope image of Integrated Diffractive Mirror trap (IDM trap) taken by GTRI. The array of optics consists of 5 collimators and 3 other test optics. Collimators collect ion light, collimate it and send it out of the vacuum chamber. We also have a collimator at the loading zone which is located at the most left side of the trap. This collimator is $200\mu m$ long. Most of the area of this collimator is etched away to create the loading zone(oval shape black area on the left side of the chip in Fig. 2.12). We demonstrated that even with this mirror, imaging is possible and aberration is not dramatically high. On the right side of the loading zone there is a small area left for logo and labelling and after that the main array of optics starts. The length of each optic is $127\mu m$ to match the commercial v-groove fibre connectors. The width of the optics are the same as the middle ground electrode which is $80\mu m$. The design focal length of the mirrors is $58.6\mu m$ so the optics cover 13% of total solid angle. The collimators in different designs have a focal length equal to nominal ion height, $58.6\mu m$, or equal to $58.6 \pm 1\mu m$ or $58.6 \pm 2\mu m$. The design is wavelength dependent and for this case the design wavelength is $369.5nm$ which is the wavelength of the main cooling transition for Yb^+ ion. The first test optic is a self imager. This optic focuses the ion light on itself. This works as a half cavity and designed to investigate quasi-cavity effects. It is shown that placing an ion in a cavity can change properties like spontaneous emission lifetime [68]. The second test optic is a laser addresser. Collimated laser light shined on this optic will be focused on the ion located at the next region. We also have a cross imager optic. If we place two ions on each side of this cross imager, their light will be focused on each other. This optic is for testing photon mediated interactions between two ions.

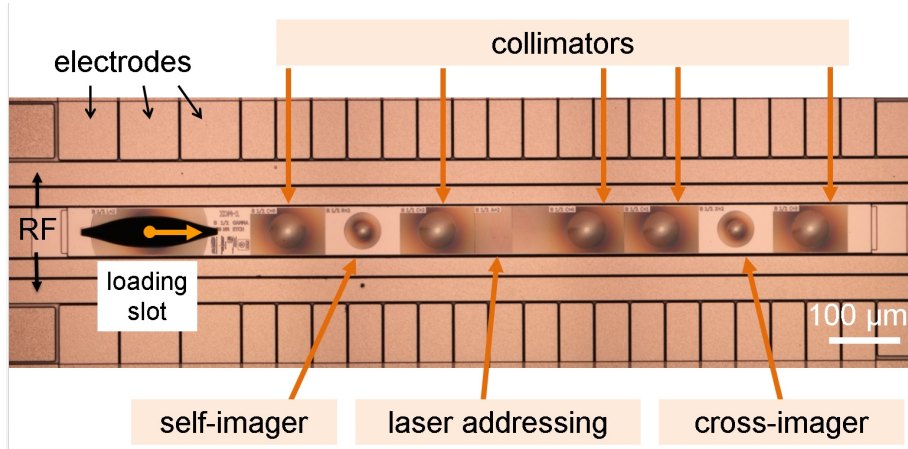


Figure 2.12: Microscope image of the integrated diffractive mirror trap taken by GTRI and layout of the array of the optics

The design of the diffractive mirrors comprised of 5 main steps:

1. Ray tracing design
2. Grating structure design
3. Single-optic mask generation
4. Array-level mask generation
5. Wafer layout design

All the design tasks were performed by David Kielpinski at Griffith University. For each of the optics ZEMAX OpticStudio was used to model a realistic ray optic tracing and find the best phase function to minimize the aberration. Designs are aberration free and their tolerances is $1\mu m$. The effect of off-conjugate imaging were also simulated to evaluate the effect of fabrication imperfections. Simulations shows that the error in ion height can have the biggest contribution to aberration.

The next level of fabrication was to create 2-level, 4-level and hybrid step profiles using the phase functions obtained in the previous step. 2-level design approximates the phase profile with a two level profile with the height of $90 nm$. In 4-level design, steps are $45nm$ high and have equal widths. The hybrid design uses 4-levels for inner rings with widths greater than $200nm$ and 2-level for outer rings with widths smaller than $200nm$. For all the designs, lateral features smaller than $100nm$ were removed. To optimize the diffraction efficiency of the step profiles we used a genetic algorithm. Gsolver and GD-calc was used to calculate the diffraction efficiencies.

Gsolver solves Maxwell's equations within an arbitrary periodic grating structure at the interface of two semi-infinite half-spaces: the superstrate, and the substrate. It is a visual software that uses rigorous coupled wave analysis and modal analysis to evaluate diffraction efficiency of arbitrary gratings. GD-calc is a MATLAB-based system simulation that also uses rigorous coupled-wave vector diffraction analysis to calculate diffraction efficiency. These two independent solvers were used to make sure that diffraction efficiency calculation are accurate and consistent. The final step in diffraction efficiency evaluation was to add constraints in fabrication with lithography to calculate a realistic diffraction efficiency.

Fig. 2.13 shows a schematic of a 4-level profile and its calculated diffraction efficiency. The steps have equal widths and heights and the diffraction efficiency is between 60-80%. Simulation shows that if we use 2-level design but with the height of $90nm$ we get 30-40% diffraction efficiency and for hybrid design we get about 40-60% efficiency.

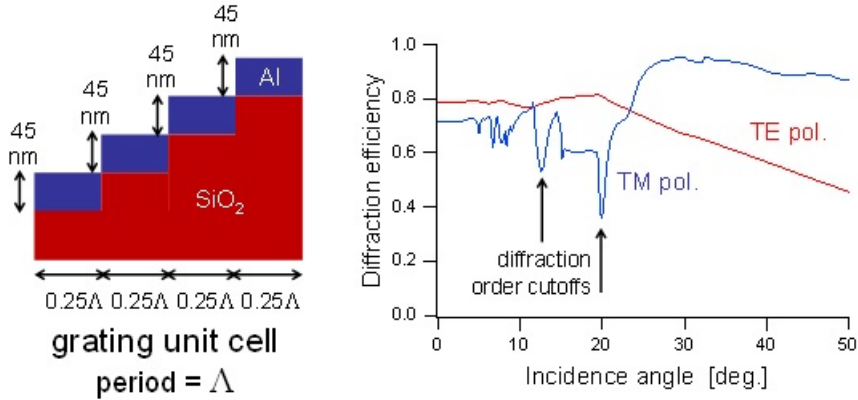


Figure 2.13: Left: Schematic of the design sizes for the 4-level grating structures. Right: Simulated diffraction efficiency as a function of the incidence angle of light. (Image courtesy of David Kielinski)

Next step in designing was to create the masks. To account for fabrication limitations we used different types of designs in each mask. Masks were saved in PNG format. Nominal ion height in Microwave I Trap is $58.6 \mu\text{m}$. This number is inferred using Poisson's equation simulation but was never confirmed experimentally by GTRI. Because of optical aberrations in high NA optics, our design tolerance is only $1 \mu\text{m}$. With deviances greater than $2 \mu\text{m}$, the aberration becomes significant. Because of this problem we designed arrays than contains collimators that have focal lengths equal to or 1 or 2 μm above or below nominal ion height. In general it is possible to use DC fields to push the ion up or down but pushing ion away from the RF node increases the micromotion and it makes ion unstable therefore we tried to avoid using this method as much as possible. We designed 4 different masks and labelled them α, β, γ and δ . Currently we use γ design which contains collimators with focal lengths equal to nominal ion height or $+1, +2$ and $+4 \mu\text{m}$.

To fabricate mirrors and electrodes, Separate lithographic processes is used and this may lead to an offset between ion poison and focal point in the plane parallel to the trap surface. Offset along the RF rails is not a problem because it can be fixed with DC fields without any side effects but if we push the ion laterally we increase the micromotion of the ion. Even though this offset was predicted to be less than $1 \mu\text{m}$, we still tried to defend against this possible problem by having lateral offsets in some of our array designs.

We combined all these different array designs in a wafer to create the final mask for fabrication. This mask is shown in Fig. 2.14.

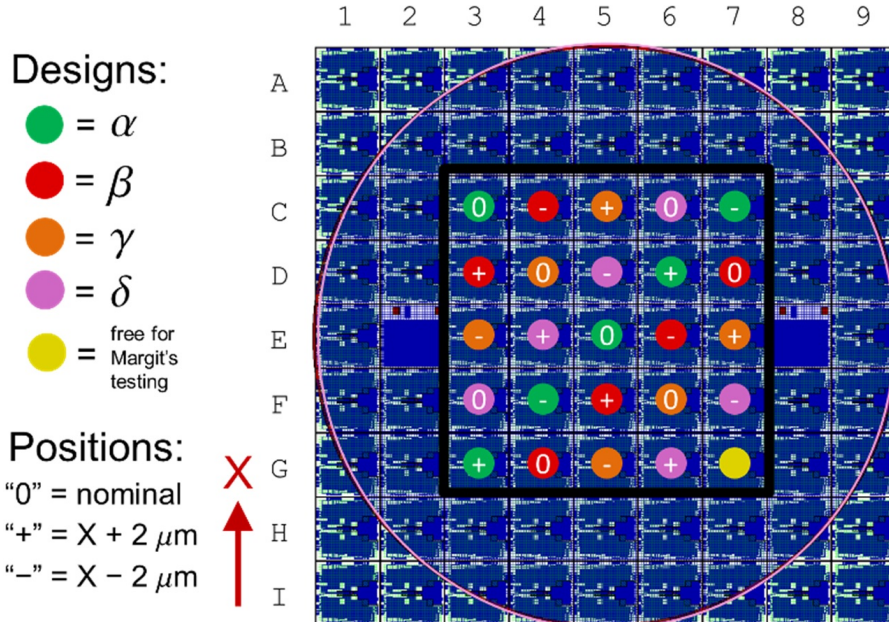


Figure 2.14: Complete layout of a single wafer, incorporating defence against both ion height errors and lateral offset errors.(Image courtesy of David Kielpinski)

2.3.3 Fabrication Of The Diffractive Mirrors

GTRI and Fraunhofer Heinrich-Hertz Institute (FHHI) performed the fabrication of the Integrated Diffractive Mirrors. The process needed a work flow that matches the capabilities of both institutes. The coordination and supervision of the process flow were undertaken by David Kielpinski at Griffith University. FHHI had some design requirement and material characteristics to be able to perform a fine task of fabrication of diffractive mirrors. We had to decide at which step of the original fabrication process we want to perform the intervening step of etching the mirrors. After consulting with both institutes the decision was that GTRI builds an initial three level substrate and send it to Germany for electron lithography and leaves the rest of the process until after receiving the altered substrate back.

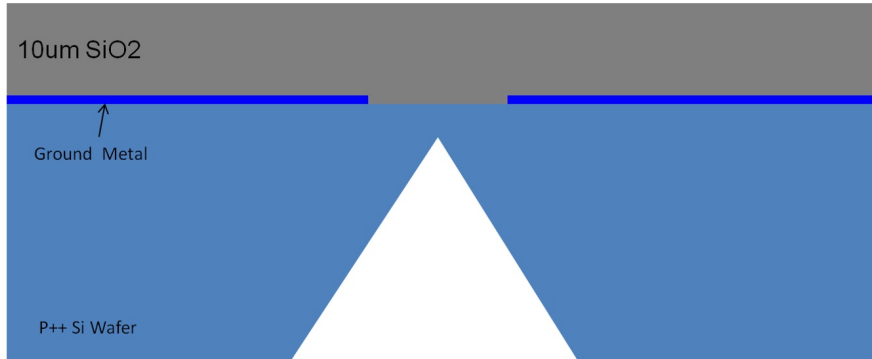


Figure 2.15: Representative image of the substrate prepared by GTRI to send to Fraunhofer Institute (Details in text) (Image courtesy of David Kielpinski)

This substrate included a P^{++} doped Si wafer that had a ground metallic layer on top of that and at the most top level there was a $10\mu m$ SiO_2 layer (Fig. 2.15). The next step was sending this substrate to FHHI for lithographic etching of the mirrors. FHHI required $1.5-2\mu m$ alignment marks with vertical side walls and uniform oxide thickness with RMS roughness of $< 5nm$. The original roughness of the oxide layer was of the order of $10-20nm$. GTRI performed a chemical mechanical polishing -which is not part of their original fabrication process- to reach the roughness of $5nm$. Before starting the fabrication process some preliminary samples were sent to FHHI to confirm the suitability of the characteristics of the substrates.

After transferring the substrate to FHHI, they started the fabrication process of the mirrors with electron lithography. They tried to fabricate 2-level, hybrid and 4-level designs. The fabrication of 2-level and hybrid designs were successful but they concluded that feature sizes are too small for 4-level design for the alignment tolerance required. We currently use the hybrid design which has 4 steps for big features and 2 steps for small features. FHHI performed an AFM microscopy and confirmed that the step sizes are within 5% of the nominal size(45-50nm). Representative image of the outcome of this process is shown in Fig. 2.16.

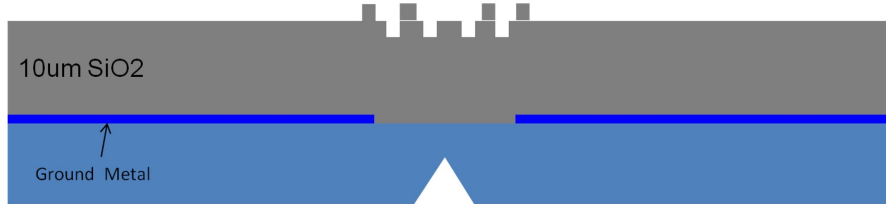


Figure 2.16: Cross section as delivered by FHHI after diffractive mirror fabrication (mirror features are not to scale) (Detalis in text) (Image courtesy of David Kielpinski)

At this point GTRI had to coat a metal layer on top of the oxide layer but they had to consider some complications that could have arisen during the process:

1. The most important challenge was that the coating may wash the features out.
2. This metal had to act as ground electrode and if after fabrication it was not electrically connected it would not perform its role.
3. The features could have been damaged during the coating of surrounding thick electrodes and had to have some protection during this process.
4. mirror's layer and other thicker electrodes had to end up at the same height at the end of the process.

In deciding the ideal metal layer thickness, both feature size and connectivity plays a role. After coating the metal layer, ridges become thicker and trenches become narrower and using too much metal washes out the whole features. On the other hand using too thin of a metal layer may affect the electrical connectivity. After some tests 100nm of metal was found to be the best thickness. This thickness still changes the size of ridges and trenches but this was already been considered and countered in the mask design. Fig. 2.17 shows a microscope image of the features before and after metal deposition.

After this step surrounding oxide substrate was plasma-etched to match the height of mirrors with the thicker electrodes that would be deposited later (Fig. 2.18 a). An oxide layer also deposited on the mirrors to protect them during subsequent processing (Fig. 2.18 b)

In that stage of the process DC and RF electrodes were deposited and ICP aluminium etch was used to cut the metal and separate different electrodes(Fig. 2.19 a). Then a $1\mu m$ oxide layer was used on the outer side of the electrodes to insulate these DC electrodes from the outer ground electrode that would be deposited at that position(Fig. 2.19 b). At this point the final etching of oxide for the gap between electrodes and making the loading zone hole was performed. A photo resist was also used to protect mirrros from etching.

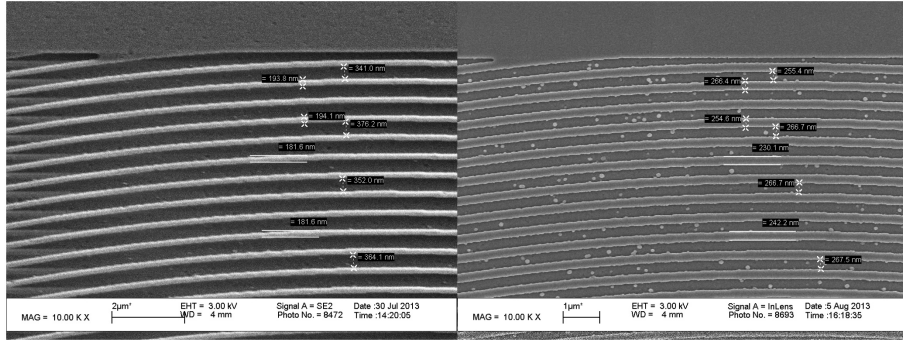


Figure 2.17: Small diffractive mirror features as received and after metal deposition. (Image courtesy of David Kielpinski)

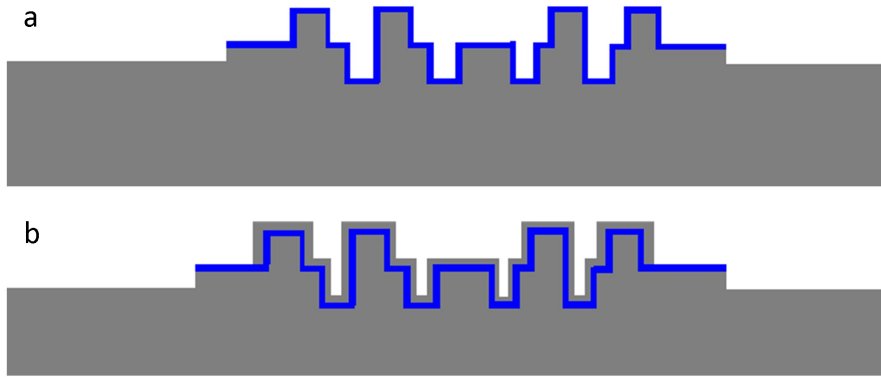


Figure 2.18: a. Wafer after plasma etch b. Diffractive mirrors with oxide protection layer (Detalis in text) (Image courtesy of David Kielpinski)

Finally to finish the fabrication process the protective oxide layer was removed (Fig. 2.19 c).

Not all the attempts of fabricating a completed chip from patterned substrates were successful but GTRI could fabricate numbers of working ion trap chips from patterned substrates. An image of a successful binary and hybrid mirror fabrication is shown in Fig. 2.20 . Fig. 2.21 shows a SEM microscope image of a completed 2-level mirror taken by GTRI. They also imaged a completed chip using a dark-field microscope shown in Fig. 2.22 .

To investigate the potential ways of improvement in fabrication, nano-imprinting was found to be an attractive option[69]. It fixes multilevel fabrication problem, trap-misalignment issues and feature size limitations that we had in electron lithography. Although the pressure that it needs for imprinting is 1 GPa which is on the order of fracture stress for silicon wafers. At this moment this is just a plausible idea and an extensive research is needed to make it practical.

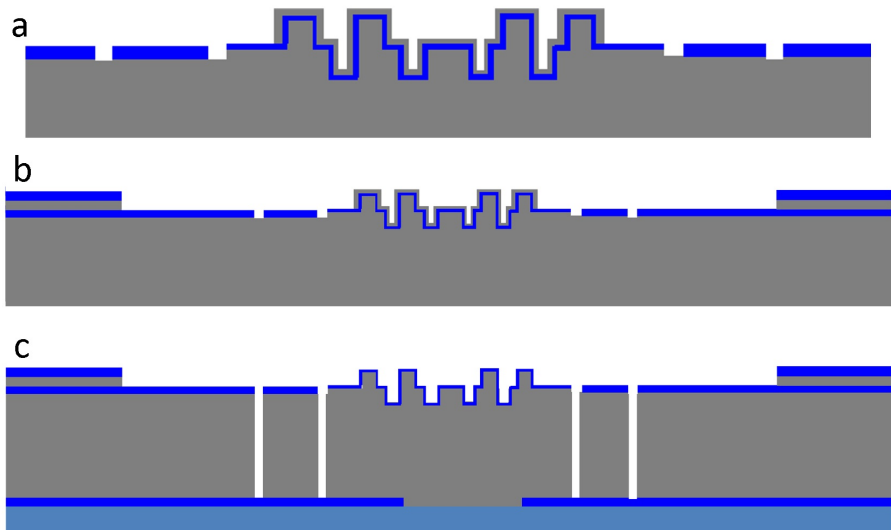


Figure 2.19: a. DC/RF Metal Deposition and Etch b. Top metal deposition and etch c. Final Device Cross Section (Details in text) (Image courtesy of David Kielpinski)

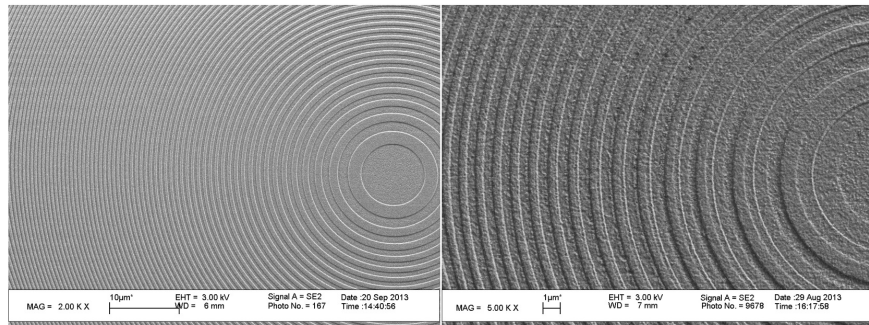


Figure 2.20: Binary (left) and Hybrid (right) diffractive mirrors after completed ion trap fabrication (Image courtesy of GTRI)

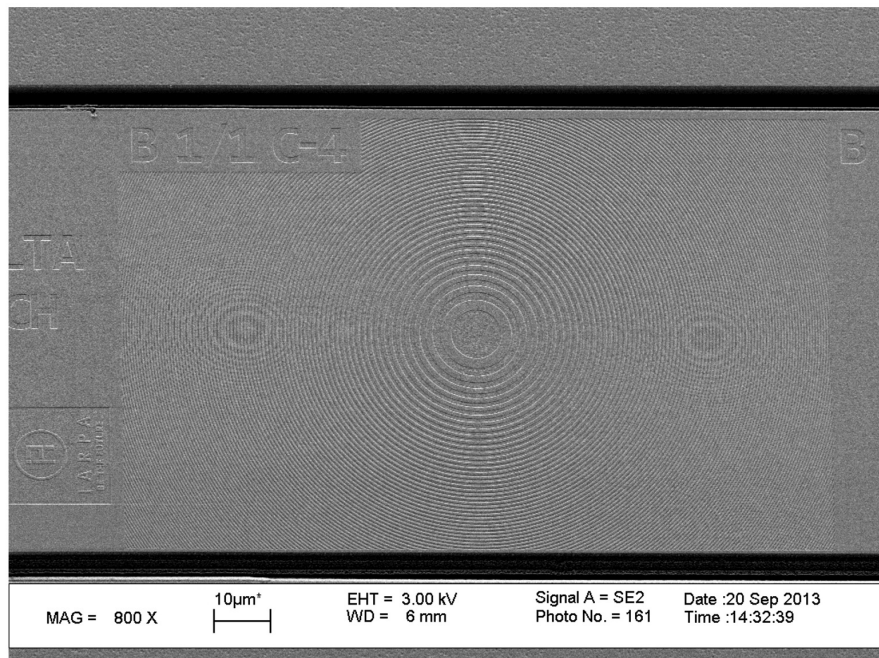


Figure 2.21: Full Binary DOE on a completed ion trap (Image courtesy of GTRI)

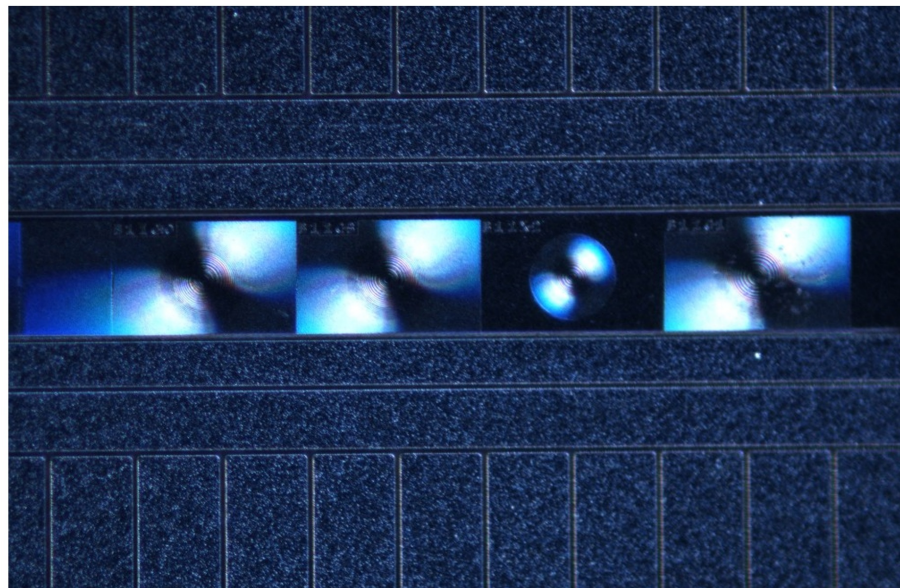


Figure 2.22: Dark field image of DOE's on completed ion trap (Image courtesy of GTRI)

2.3.4 Diffractive Mirrors Characterization

This section covers the preliminary tests performed by GTRI and our group on Integrated Diffractive Mirror chip. The main characterization of imaging and light collection will be discussed in chapters 4 and 6 .

GTRI did the initial tests on the new chip. The first test chip was a hybrid one. The ion used by GTRI for testing was Ca+ ($\lambda = 397\text{nm}$) so the wavelength was slightly different from design wavelength of 370nm. The first optic that they tested was the self-imager. This test was as straight forward as moving the ion over the optic and capturing the ion image next to the ion itself (Fig. 2.23).Images show that there is a lateral displacement between the ion and its image. This is due to the mismatch of less than a μm between mirror fabrication and electrode fabrication. Using a lateral DC field they showed that this mismatch is fixable(Fig. 2.24). Because of the nonlinear EM gain in their EMCCD camera, the relative brightness of the image cannot be used to estimate the collection efficiency of the optic.

To test the collimator, they used a reflective objective to image the ion. As shown in Fig. 2.25, this objective has an annular aperture and the center of the objective is blocked by the second mirror. This means that the second mirror will block the collimated beam in the ideal situation where the ion is at the center of the collimator and both optics has a common axis. By pushing the ion to the side they captured the image shown in Fig. 2.25 b. This is taken with the iris closed to its minimum aperture and depth-of-field is large enough that the blocked area is roughly visible in the center of the image 2.25 a.

Fig. 2.26 shows two images of the ion with iris open (a) and iris closed(b). The one with the iris open collects, the collimated light, the direct light from the ion and the scatter from the chip. In this mode, it is hard to distinguish the light that is coming from the collimator. With the iris closed the numerical aperture becomes very small for direct light and the scatter but has minimal effect on the narrow collimated light therefore a clear image of the collimated beam can be captured that is shown in Fig. 2.26b.

To measure the enhancement in light collection form the collimator they used a PMT to count the number of photons for different ion positions both with iris open and closed.

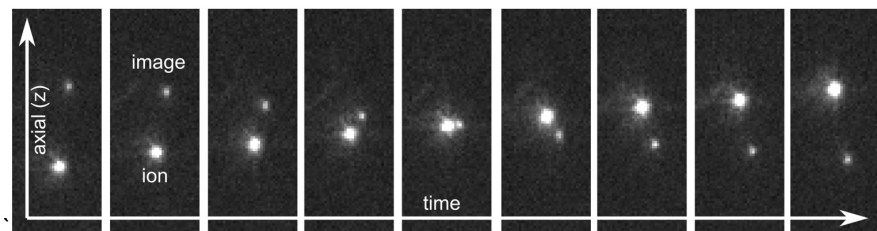


Figure 2.23: Ion transport image over the Self-Imager taken by GTRI

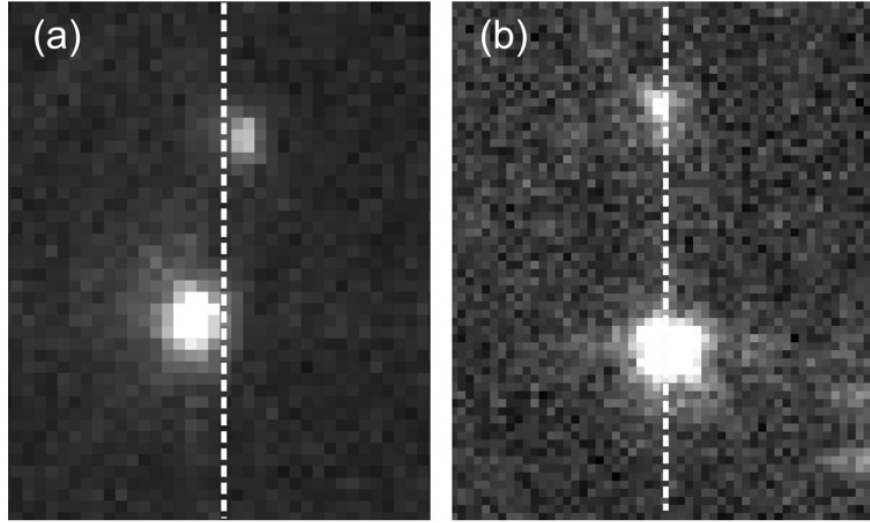


Figure 2.24: (a) Ion and image alignment when micromotion nulled. (b) Applied radial electric field pushes the ion to the right, with a corresponding movement of the image to the left. (Image taken by GTRI)

In both cases lasers track the ion position to keep fluorescence constant. The background scattered light is also measured without ion for both cases. Fig. 2.27 shows the background corrected data for different positions. The graph shows that with the iris open, number of photons in a fixed time interval is 0.8. For the positions that collimated light is also being collected this number increases to maximum of 1.8. Second graph shows that closing the iris suppresses the direct light collection by a large amount but has almost no effect on the collimated light. Even though the center of the collimator located at $235\mu m$ (nominal position marked on the graph), the maximum light collection happens around $245\mu m$. This happens because of the occluded objective that GTRI used and does not mean that the center of the collimator is at $245\mu m$.

Data on the graph in Fig. 2.27 suggests that the collection for direct light is 0.8 and for mirror is 1 in a fixed interval. Knowing that the numerical aperture (NA) of the objective is 0.28, they estimated NA of 0.31 or collection of 2.5% for the mirror. Our later rigorous characterization shows that this collection is 5.8% (See chapter 6).

After finishing the initial tests GTRI sent the tested trap to Griffith. This trap was damaged during transport and some DC electrodes were shorted. GTRI sent us a special set of potentials that took into account the shorted electrodes. We used a 2X amplifier for our operations because our standard DAC system supplies $\pm 10V$ but some electrodes needed $\pm 20V$.

The next step for trapping was to prepare lasers. We were sure that the frequency of the lasers are correct because we trapped an ion in our old trap, using the same lasers.

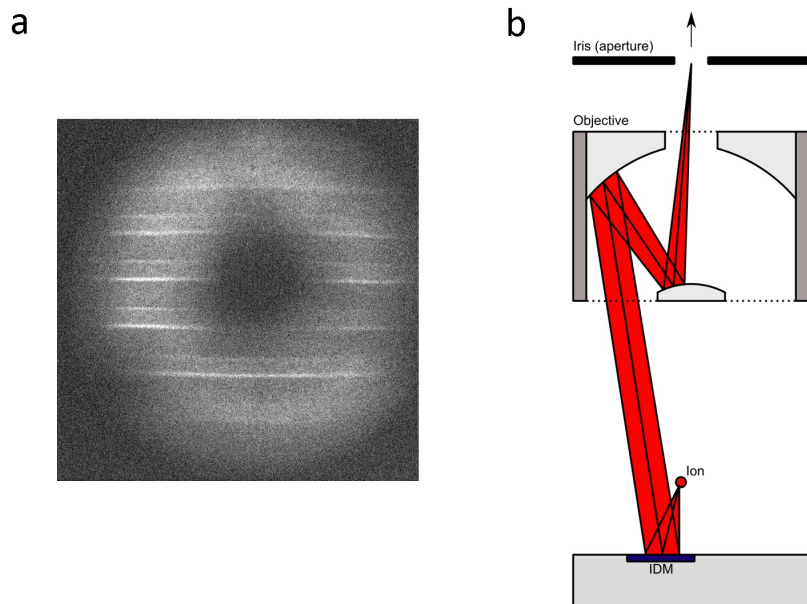


Figure 2.25: a. : With the lens aperture closed, the depth-of-field is large enough that the central obscuration of the objective is visible as a dark inner region. The bright horizontal bands are patterns on the trap surface. b. Rough diagram of light collection from IDM with the reflective objective. The collimating optic collection efficiency data were taken so such that the light would both be collected by the lens and pass through the iris when the iris was closed. (Image courtesy of GTRI)

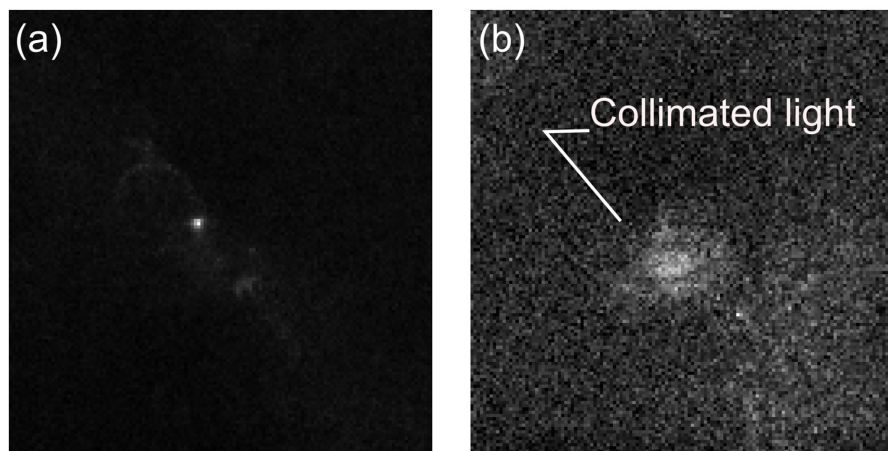


Figure 2.26: (a) Direct imaging (iris full open) and (b) collimated light imaging (iris closed to minimum) of the ion. (Image courtesy of GTRI)

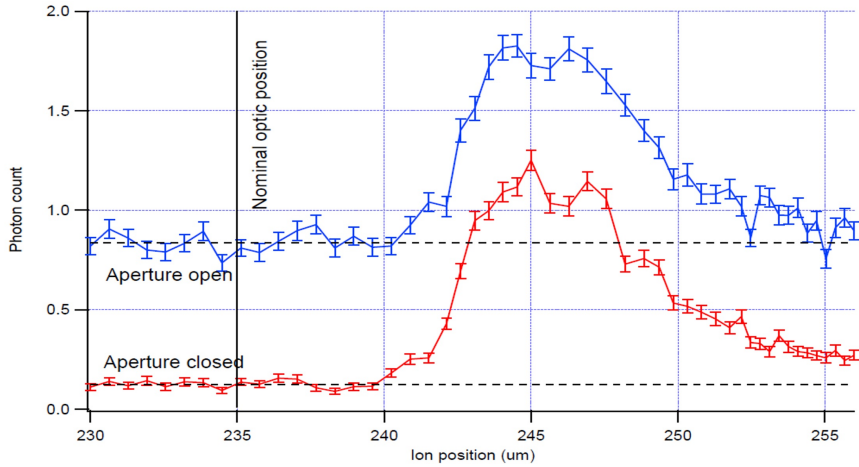


Figure 2.27: PMT counts vs. ion position over the collimating optic for the lens aperture (iris) fully open and for the aperture at minimum (closed). The dashed lines are guides for the eye, showing the photon counts for the direct light from the ion, as extrapolated from the measurements in left wing of the plot. Both measurements have had position dependent backgrounds (measured separately without an ion) subtracted out. (Graph by GTRI)

To set the beam pointing we had to preset the laser position and angle and then scan the beam position around the preset point. The first step in presetup was to make sure that the beam is parallel to the surface of the chip. We did this by checking the laser beam on a card where it exits the back window. When the beam is too angled towards the surface, a clear reflection of the laser off the surface can be seen on the card. When the beam is angled up, pushing the beam towards the surface cuts laser in half but no reflection can be seen. When the beam is parallel to the surface, hitting the chip creates a diffraction pattern on the card. When the diffraction pattern has the maximum brightness, center of the beam is at the chip surface. From this point we need to move the beam up by about 50-60 μm to center it at ion. The positioning parallel to the surface was done by setting the beam to the center of the oval shape loading zone hole. This was done by looking at the camera image taken from the top.

It is important that the beam does not hit the surface of the trap while RF voltage supply is on. If this happens the photo electrons ejected by high energy UV photons hit the exposed silicon dioxide and charge it. During time this build up of charge creates a stray field that makes trapping impossible. Wait time of several hours is needed for the charge to dissipate.

Supplying the RF voltage was the next step. We started with RF frequency of 23 MHz but our attempts were unsuccessful. By changing the RF frequency to about 26 MHz we managed to trap our first ion. The first image that we captured (Fig. 2.29) was obtained

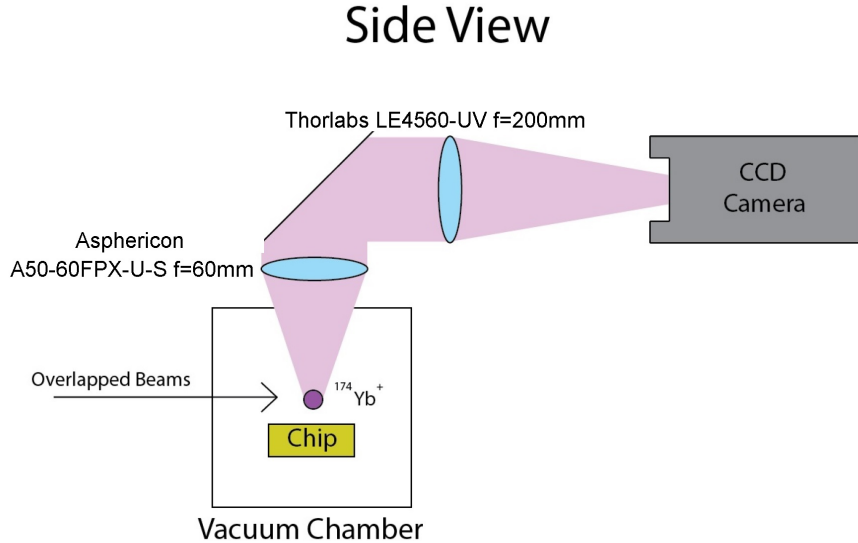


Figure 2.28: Schematic for bulk collection optics. The trapped $^{174}\text{Yb}^+$ ion acts as a point source. The first lens collimates the collected fluorescence while the second lens focuses(re-image) the collected fluorescence onto a CCD camera. The distance between the 60mm lens and the 200mm lens is 260mm.

only using external bulk optics as shown in Fig. 2.28. We use this imaging mode for trapping and shuttling. At this point of time we did not have the capability to shuttle the ion and all the test were made at loading zone.

By changing the optical setup configuration, we focused the light reflected from the load zone collimator on the camera. The image taken is shown on the right side of Fig. 2.31 . In this mode we used an iris on our objective lens to make sure that we are limiting the collection of scatter from the surface of the chip. Due to aberration the image size is several times larger than diffraction limit. One of the reasons for this aberration is that the ion is not exactly at the right height for the collimator. Another important reason is that during the ablation of the loading zone the mirror was deformed. The image in Fig. 2.30 shows that if we move the ion along the trap axis by several *μm* two images will be formed from one ion. Changing the height of the ion changes the distance between these two images. The same behaviour was observed in the diffractive lens project (Previous project in the group) when ion was not at the focus.

The florescence counts that we measured from the collimator was the same as bulk optic imaging within 20%. Numerical aperture of the bulk optics is 0.39 equivalent to collection efficiency of 4%. Therefore the estimate for collection efficiency of the loading zone mirror is $4\pm1\%$. The size of loading zone mirror is about 50% bigger than other collimators but about half the area is ablated to create the loading hole therefore we get

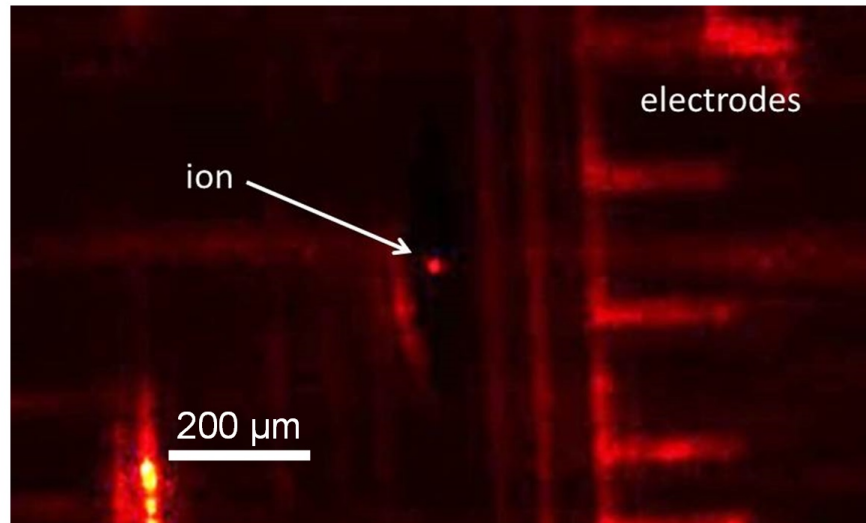


Figure 2.29: A single ion trapped in the IDM trap loading region. Imaging was performed using the bulk-lens objective. The diffractive mirrors were not used to obtain this image.

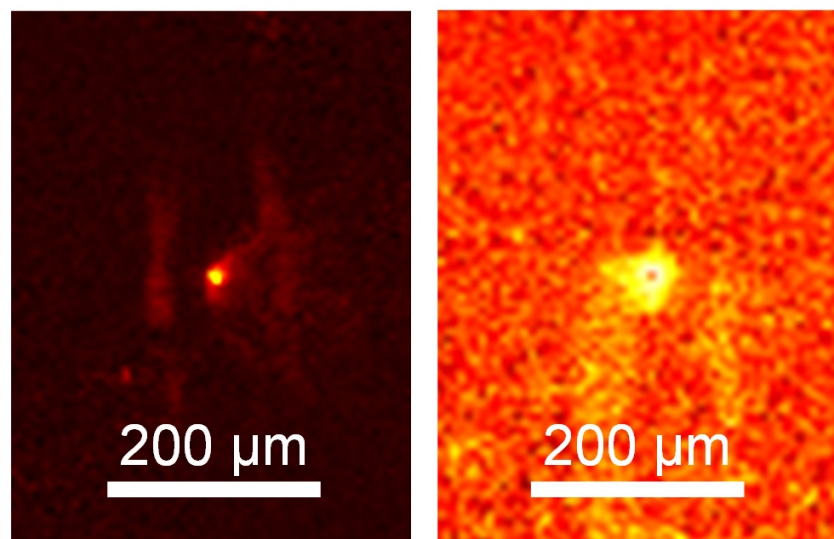


Figure 2.30: Comparison between bulk-lens and diffractive mirror imaging for a single ion in the IDM trap. Both images are taken under identical camera integration conditions and are background-subtracted to remove scattered light. Left: bulk-lens image. Right: diffractive mirror image obtained with the loading zone collimator. The fluorescence collection efficiency is estimated as 4%. The loading zone collimator is cut in the middle to create the loading hole. That is the reason why the aberration is high and the image size is much larger than the diffraction limited size.

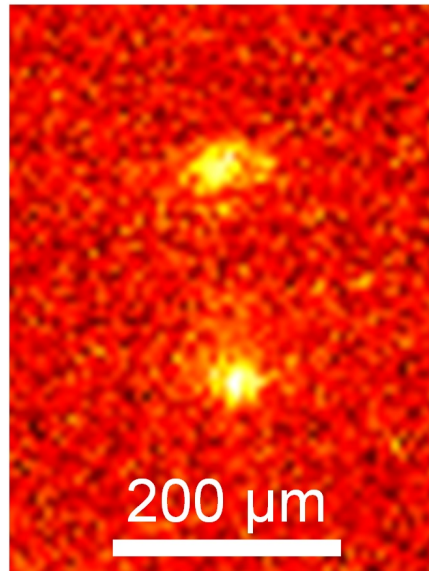


Figure 2.31: Image of a single ion using the loading-zone diffractive mirror. The image was obtained by moving the ion several microns along the trap axis relative to the image in Fig. 26. The apparent duplication of the image is consistent with aberrations of the imaging system.

higher collection efficiencies for other mirrors(See chapter 6).

2.4 Atom source

To create and trap Yb ions a source of neutral Yb is needed. We generate these atoms using an atomic oven. The oven consists of a tantalum foil cylinder filled with Yb chips. By sending about 1 A of current through the oven we make it hot and this evaporates the neutral Yb. A larger cylinder is placed between ovens output and the loading hole in the chip. This second cylinder prevents neutral Yb from coating the chip pins and shorting them. It contains of two disk with a hole at the middle that collimates the neutral Yb beam and directs that towards the trapping node.

Despite having the collimating cylinder, oven coats some Yb on the back side of the loading hole and over time this layer changes the potential at the loading zone. This can be countered using an upward electric field. Previous experience shows that Yb gradually covers the top vacuum window as well and it may drop the transmission of the window dramatically over time. In this case the trap has to be brought up from vacuum and the window must be cleaned by soaking in a dilute concentration of sulphuric acid.

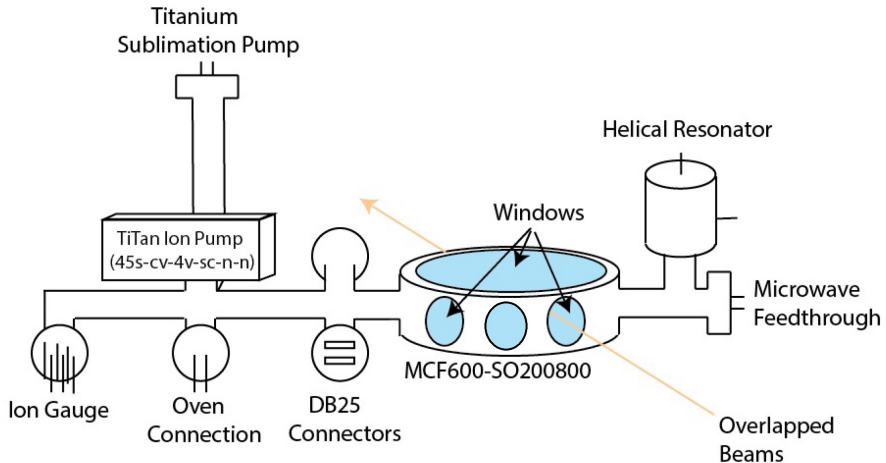


Figure 2.32: A schematic of the vacuum chamber which consists of the main octagonal part and branches for titanium sublimation pump, ion pump, ion gauge, oven connection Microwave feedthrough, DB25 connections and RF input. (Image courtesy of Valdis Blums)

2.5 Vacuum System

The trap needs to be installed in a vacuum chamber for operation. In ultra-high vacuum regime ($\sim 10^{-11}$ Torr) the ion lifetime is of the order of hours for our system. A schematic of our vacuum system is shown in Fig. 2.32 . A Kimball Physics MCF600-SO200800 spherical octagon chamber is the central part of our vacuum system. This design allow us to have six 2" windows, approximately 150 mm from the center of the trap, for horizontal axes of lasers and two 4" window for optical access from top and below (With Chip trap only the top window can be used for imaging). It is equipped with a titanium sublimation pump, an ion pump and an ion gauge.

The trap is built on a $11 \times 11\text{mm}^2$ Silicon Dioxide substrate which is housed in an interface plate that contains 100 pins connected to trap DC electrodes. The trap socket is made of PEEK (polyetheretherketone). Socket pins are connected to four Vacuum compatible DB25 connectors through Kapton coated solid-core wires. To avoid contamination from entering the vacuum system, at the time of building or opening, a walk-in clean room (specified at class 10,000) is used. Many types of contaminations including plastic and bio-chemicals can prevent trap to reach ultra-high vacuum even with long baking times. The new chamber was baked for 20 days without the trap installed. We use heater taps and aluminium foil to heat the trap up and use manual variacs to control the heat. The temperature is monitored using a thermocouple thermometer.

To build the vaccum chamber for the first time we cleaned all the components (except for the chip itself) by sonication in acetone then methanol and lastly isopropanol. Then

all the metal and ceramic parts assembled and mechanically pumped to $\sim 10^{-8}$ Torr. This pumping system consists of a turbo pump connected to a roughing pump. At this stage residual gas analyser (RGA) was used for leak check. Then the chamber was baked (without chip trap) with 350°C for 20 days to remove hydrogen and water from the stainless steel.

The next part was installing the chip and reaching ultra-high vacuum. This part of the procedure must be repeated each time we open the trap. We need to fill chamber with nitrogen to bring it to atmospheric pressure and open it in a clean room. After installing the chip we let the turbo and roughing pump to drop the pressure to 10^{-8} Torr. At this stage the chamber(including the chip) is backed 200°C for a week. After finishing the baking and letting the chamber to cool down, ion pump, ion gauge and Titanium sublimation pump are degassed. At this stage the chamber is sealed from mechanical pumps, with an all metal angle valve, and ion pump and titanium sublimation pump bring the pressure down to 10^{-11} Torr and keep it there. At the moment we do not use an ion pressure gauge because it tends to increase the pressure while operating. The pressure is being monitored using ion pump pressure reading which is derived from the pump current.

In our first attempt after installing the trap the chamber was baked for about 2 weeks with 250°C . At the end of the procedure, the monitoring of the contaminations with residual gas analyser (RGA) showed PEEK contamination. After cooling down the chamber the pressure only reached 3×10^{-9} Torr which is not acceptable for the trap operation. We found out that the problem was that temperature was too high for PEEK and it started outgassing. Baking the chamber again without the trap with 350°C did not solve the problem therefore ultrasonic cleaning was used. For the next bakeout we tried to keep the temperature between $180 - 200^{\circ}\text{C}$ and successfully reached 10^{-11} Torr. Baking with the temperature of 200°C and higher for a long time can also lead to formation of micron sized hummocks and extruded whiskers on trap electrodes therefore it is recommended to keep the temperature below 200°C and keep the baking time as short as possible.

CHAPTER 3

Laser Systems, Cooling and Ionization

Keeping an ion trapped in a Paul trap and manipulating and reading ion's quantum state involve interaction of the ion with one or more lasers. Atoms interact with only selected wavelengths and only for narrow bandwidths. We use three external cavity diode lasers(ECDLs) in our experiments and use atomic spectroscopy to lock the frequency of the two of them. These lasers include a 370 nm laser, used for cooling/florescence generation and ionizations, a 399 nm Laser for ionization, and a 935 nm laser, used to drive the ion, when it drops to a particular dark state for 370 nm laser.

3.1 Scattering Rate and Saturation Intensity

The two main atom-photon processes involved in this experiment are absorption and spontaneous emission. In the process of absorption a photon, that has an energy close to the energy difference between the two atomic levels, is absorbed and excites the atom to the higher level. For an atom in an excited state, there is an exponential decay probability, with a time constant called the transition lifetime, to decay to a lower state and emit a photon in a random direction. This is called spontaneous emission. The time scale of this process(transition life time) is $\hbar/\Delta E$, where ΔE is the energy difference between current level and a lower energy level and \hbar is the reduced Plank's constant.

The chance of absorption and emission of a photon depends on the intensity of the laser, natural characteristics of the atom and the specific transition properties. The total scattering rate for a 2 level atom, driven by a laser, is [70]:

$$\gamma_p = \frac{s}{1+s} \frac{\gamma/2}{1 + (2\delta/\gamma')^2} \quad (3.1)$$

Where s is the saturation parameter, γ is the natural decay rate of the transition, δ is the laser frequency detuning from the resonance and $\gamma' = \gamma\sqrt{1+s}$. The saturation parameter s is defined by the ratio of the laser intensity I and saturation intensity I_{sat} . Saturation intensity is defined as having one photon per atomic cross section per spontaneous lifetime. The saturation intensity for a 2 level atom, with laser at resonant frequency, is [70]:

$$I_{sat} = \frac{\pi hc}{3\lambda^3\tau} \quad (3.2)$$

Where h is the Planck's constant, c is the speed of light, λ is the wavelength of the laser, $\tau = 1/\gamma$ is the excited state lifetime. The resonance saturation parameter is defined by:

$$s_0 = \frac{I}{I_{sat}} \quad (3.3)$$

For the $^2S_{1/2}$ - $^2P_{1/2}$ transition of $^{174}Yb^+$ we have:

$$I_{sat} = 0.05W/cm^2 \quad (3.4)$$

If laser is detuned by δ from the resonance, the cross section decreases therefore we have smaller saturation parameter:

$$s = \frac{s_0}{1 + (2\delta/\gamma)^2} \quad (3.5)$$

Equation 3.1 shows that if the laser frequency is at resonance and the laser intensity is the saturation intensity, the scattering rate is $\gamma/4$. For $^{174}Yb^+$, the $^2S_{1/2}$ - $^2P_{1/2}$ transition linewidth, γ , is 19.6MHz therefore the scattering rate for saturation intensity is $30.8 \times 10^6 photons/sec$.

3.2 Yb Atomic Transitions

In my project two set of distinct energy levels of Yb were important; the first one was the transitions for the neutral ^{174}Yb atom and the second for $^{174}Yb^+$ ion.

At the start of each experiment we generate neutral Yb atoms and ionize them in a two level process shown on the left side of Fig. 3.1 (For detailed explanation of ionization process refer to section 3.3). The first step of the ionization is to excite the 1S_0 - 1P_1 transition in neutral Yb. The wavelength of this transition is 399.2 nm with the natural linewidth of 28 MHz giving an excited state lifetime of 5.7 ns. The second transition is the excitation from the 1P_1 level to the continuum. The energy of 370 nm photons is enough for this final step of ionization.

The right side of Fig. 3.1 shows the relevant transitions for $^{174}Yb^+$ ion. The main transition here is the $^2S_{1/2}$ - $^2P_{1/2}$ transition with wavelength of 369.5 nm. Linewidth of this transition is 19.6 MHz which is equivalent to excited state lifetime of 8.1 ns. This is the main transition for cooling, fluorescence imaging and single photon generation. When the ion is excited to $^2P_{1/2}$ state, it returns back to $^2S_{1/2}$ state 99.5% of the time and emits a photon with wavelength of 369.5 nm but there is a 0.5% chance for the ion to fall into $^2D_{3/2}$ state. The life time of this state is 53ms and falling into this state slows down

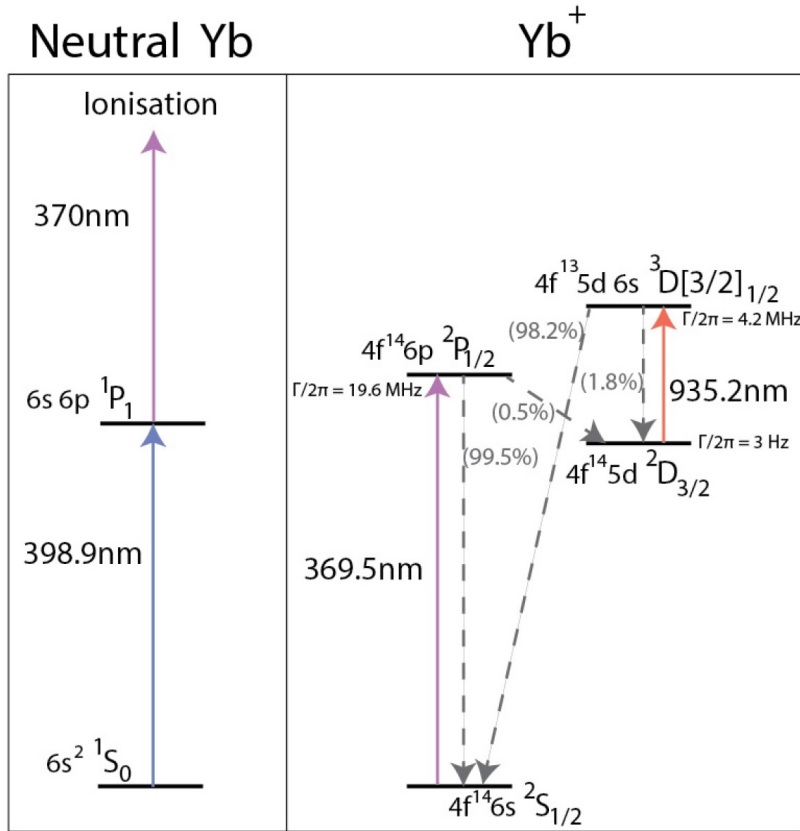


Figure 3.1: Relevant energy levels for neutral and ionised Yb. Left: Neutral Yb energy levels from [5]. Right: Yb^+ energy levels and branching ratios from [6]. Spontaneous decay times from $^2P_{1/2}$, $^2D_{3/2}$ and $^3D[3/2]_{1/2}$ states are 8.1ns, 53ms and 37.9ns respectively.

the process of cooling and fluorescence generation for this period of time. To prevent this delay, we pump the $^2D_{3/2} - ^3D[3/2]_{1/2}$ transition with a laser at 935.2 nm wavelength. The linewidth of this transition is 4.2 MHz. From the exited state of $^3D[3/2]_{1/2}$, atom falls to $^2S_{1/2}$ state with probability of 98.2%. The lifetime of this decay is 37.9ns which is about six orders of magnitude shorter than the lifetime of the metastable state $^2D_{3/2}$. There is a 1.8% chance for the ion to return back to $^2D_{3/2}$ state but 935.2nm laser excites the ion again and eventually it ends up in the ground state.

3.3 Ionization

In the process of trapping an ion, our atom source spatters neutral Yb atoms into the region of trapping potential. This neutral Yb gas contains 7 different stable isotopes. Table 3.1 shows the list and specification of these isotopes.

Isotope	168	170	171	172	173	174	176
Natural abundance	0.13	3.04	14.28	21.83	16.13	31.83	12.76
Normalised line strength	0.4	9.6	44.9	68.6	50.7	100	40.1
Isotope shift (MHz)	1887	1192	939 (centroid), 832 ($F=3/2$), 1153 ($F=1/2$)	533	291 (centroid), 587 ($F=7/2$), 515 ($F=3/2$), -253 ($F=5/2$)	0	-509

Table 3.1: Natural abundances [71] and isotope splittings [72] of neutral Yb. Isotopes with an odd number of atomic mass units have multiple peaks due to hyperfine structure.

^{174}Yb and ^{171}Yb are the most wildly used isotopes for trapped ion experiments. ^{171}Yb has a nuclear spin and this creates a hyperfine splitting in its energy levels. This isotope is used when there is a need for hyperfine levels such as when we want to encode a qubit. To drive these hyperfine levels and have a continuous cooling cycle, a microwave source is needed[73]. In neither of our experiments we needed these hyperfine levels, therefore we only used ^{174}Yb . This isotope is the most abundant isotope and does not have nuclear spin. Because of the abundance, the choice decreases the initial trapping time.

To selectively trap ^{174}Yb isotope, we use a double step ionization process. First we use a 399.2 nm laser to drive neutral ^{174}Yb from 1S_0 to 1P_1 . Because of the different nuclear masses, the wavelength of this transition is slightly different for each isotope. The difference in the wavelengths is very small therefore we need to have a laser with a narrow linewidth locked to the frequency of the transition of that isotope, to be able to select it.

Even if our laser linewidth is sufficiently narrow, because of the finite linewidth of the transition we may excite the neighbouring isotope ^{172}Yb . To calculate the relative chance of exciting ^{172}Yb , we use equation 3.1.

If we Suppose that the laser is at resonance for ^{174}Yb ($\delta = 0$), It is detuned by the amount equal to isotope frequency splitting for ^{172}Yb . Dividing the two scattering rates, the relative scattering rate is:

$$R_\gamma = 1 + (\Delta\delta/\gamma_0\sqrt{1+s_0})^2 \quad (3.6)$$

Where $\Delta\delta$ is the frequency difference between the transitions for the two isotopes. From table 3.1 $\Delta\delta = 533\text{MHz}$. The natural linewidth of 1S_0 to 1P_1 transition for neutral Yb, γ_0 , is 28MHz [72]. With 399 nm laser intensity of $0.5W/cm^2$ and saturation intensity of $6.8 \times 10^{-2}W/cm^2$ [72] we have a saturation parameter s_0 of 7.25. Therefore from equation 3.6 our relative scattering probability is 44.9. Higher natural abundance of ^{174}Yb increases this value by a factor 1.5 and decreases the chance of trapping ^{174}Yb to 1/75. If the transition is Doppler broadened the chance of trapping other isotopes increases. With the collimation procedure described in section 2.4 we minimize the component of atoms' speed along the laser direction and prevent Doppler broadening.

In the second step of the ionization process we need to drive the atom from 1P_1 to the free continuum state. Energy of the photons of the 370nm laser is enough for this transition. This ionization happens at the trapping node and if the kinetic energy of the ion is less than the depth of the trapping potential, It confines the ion.

3.4 Laser Cooling

There are heating mechanism in Paul traps, including RF heating, that transfers energy to the ion. To prevent loss of the ion, due to these effects, we use Doppler laser cooling. Doppler cooling is the process of extracting heat from an atom using photons. For this type of cooling one needs to use a transition with short lifetime(narrow bandwidth)[12] and laser frequency must be red detuned relative to the resonance. To explain this effect, for simplicity, we only focus on the axis parallel to the laser direction. Because of the Doppler effect, in the ion's reference frame, the frequency of the laser changes depending on the direction of the ion's velocity. In the case that ion moves towards the photons the frequency shifts towards blue and becomes closer to the resonance. The low velocity approximation for this frequency shift is:

$$\omega' = \omega \left(1 - \frac{v}{c}\right) \quad (3.7)$$

Where ω' is the frequency in ion's reference frame, ω is the frequency in lab's frame, v is ion's speed and c is the speed of light. With this frequency shift, there is a high chance for the photons to get absorbed by the atom. If they are absorbed, this head to head collision reduces the momentum of the atom in this direction. The exited atom spontaneously emits a photon in an approximately random direction. In many scattering events the effect of this random scattering averages to zero so the total process reduces the atom's energy.

In the case that the atom moves away from the photons, the frequency becomes even more red shifted and the chance of photon absorption decreases to a great extent. If this absorption happens anyway, it heats the ion. Because of the great difference between the chance of absorption for cooling and heating photons, the average effect is cooling.

If for different trapping axes the trapping frequencies are degenerate, at least 3 lasers are needed to cool the atom, one for each axis. This is the case for many trapped neutral atoms. In our case because of the anisotropy for the two RF axes and the DC axis, it is possible to use only one laser. The only requirement is that we need to set the laser direction in a way that it has a component along each of the three axes.

The lower limit for the Doppler cooling is reached when the cooling and heating rates are in equilibrium. From [12] this limit is:

$$T = \frac{\hbar\gamma}{2k_B} \quad (3.8)$$

Where γ is the transition linewidth, k_B is Boltzmann's constant and \hbar is reduced Plank's constant. The transition, that we use for cooling, is the $^2S_{1/2}$ - $^2P_{1/2}$ transition with wavelength of 370nm and transition linewidth of 19.6 MHz. For this transition the minimum temperature is 0.75 mK.

As shown in figure 3.1, there is a 0.5% chance for the ion to fall into the metastable state of $^2D_{3/2}$. This interrupts the cooling cycle and to prevent this we use a 935.2 nm laser to pump the ion out of this state and resume cooling(for detailed explanation refer to section 3.2).

3.5 External Cavity Diode Laser

The lasers used in my experiments need to be tunable and have very narrow linewidth (\ll transition linewidth). External cavity diode lasers are cost effective and efficient options for this purpose. A bare diode has a very wide bandwidth and is very sensitive to optical feedback. Sending a controlled amount of light to the diode solves this problem. This fractional feedback is generated by a diffraction grating. The -1 order of the grating is used to reflect back a small portion of the light into the diode. The rest of the light is reflected normally and used as output. This grating forms a long external cavity that narrows the bandwidth and stabilises laser against stray light. A lens is needed to collimate diode light before it hits the grating (Fig. 3.2).

The laser usually oscillates in the highest gain mode because this mode limits the

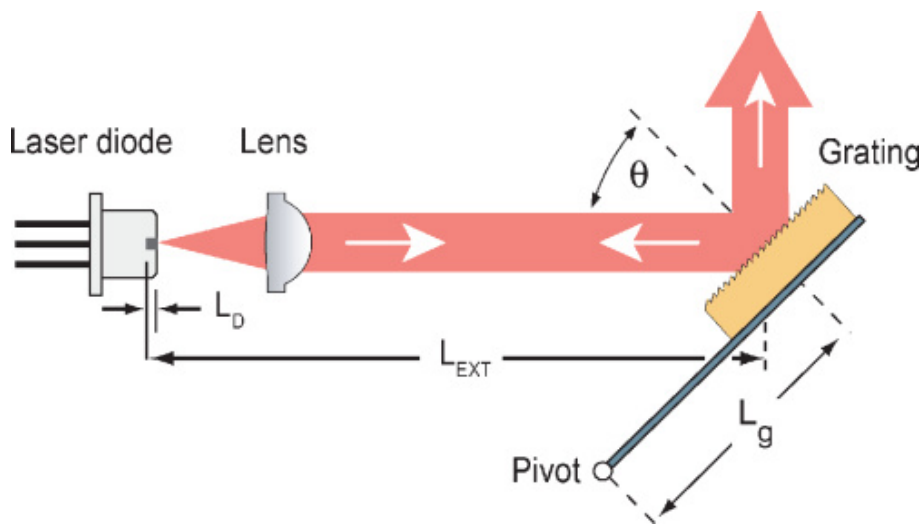


Figure 3.2: A schematic of external cavity diod laser components (Image from [7])

number of electron-holes for the other modes and as a result extinguishes the others. In ECDL this gain is a function of four factors (Fig. 3.3):

1. The medium gain: this gain is determined by properties of diode and is very wide in frequency(of the order of a few 100 GHz). Peak of this wide gain can be changed using diode temperature.
2. Internal Cavity: facets of the diode forms an optical cavity that makes the gain periodic. This period is called free spectral range. Each peak is much narrower than the medium gain peak but it is not narrow enough for our applications. Changing temperature shifts the peak of this gain in the same direction of the medium gain but with a different rate.
3. The grating feedback: For each angle of grating only a certain frequency is reflected back to the diode. The linewidth of this feedback decreases with the increase of the line density of the grating.
4. The external cavity: Grating creates an extra cavity for the diode but with longer length. This leads to a much shorter free spectral range and narrower linewidth.

All the lasers that we use are ECDLs. All of them are used to be homebuilt ECDLs but currently we use Moglabs commercial laser for 370nm. During my candidature I had to realign and optimize ECDLs. The first step in this process was to make sure that diode light is collimated after the lens. Then I tried to minimize the lasing threshold current by optimizing the direction of the backreflected beam. To measure the threshold current, I used to set the current just below lasing threshold and sweep the current and monitor laser power on a fast photo-diode. The next step was to increase the current to reach the desired power. At this power, frequency was set by changing the length of the external cavity. A discrepancy of few picometers in wavelength was fixed by changing the diode temperature.

The laser frequency is normally changed through changing the control voltage of the the grating piezo. This gives us about 2pm mode-hop free tuning range. To increase this range to about 4pm, laser current need to be changed accordingly. We use a variable gain amplifier that amplifies the monitor output of piezo driver and feed that to the modulation input of the laser current controller. By adjusting the gain to the right ratio long mode-hop free tuning range was achieved.

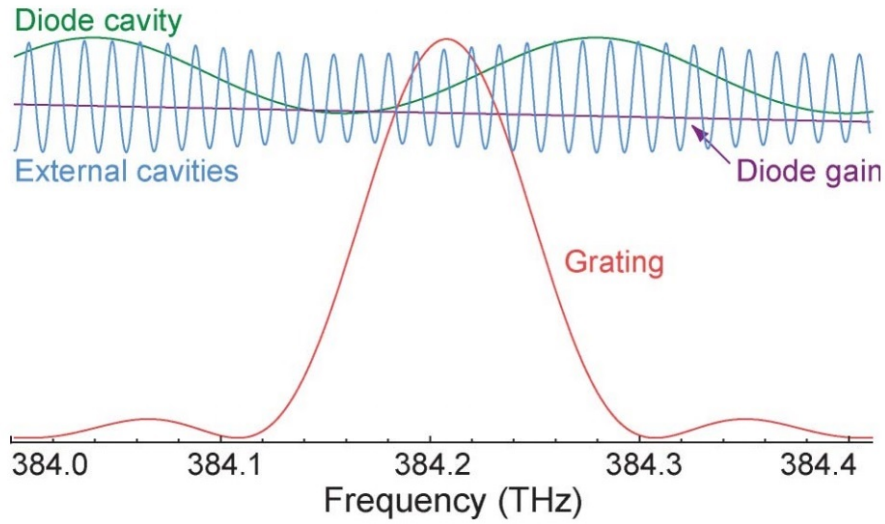


Figure 3.3:) Schematic representation for the various frequency-dependent factors of an ECDL (Graph after [7])

3.6 Optical Isolator

To protect our diodes from back reflection and prevent unwanted laser light feedback to the diode, we use an optical isolator consisting of two polarisers and a Faraday rotator (Fig 3.4). Faraday rotation is a magneto-optic phenomenon that rotates the polarization. The isolator uses an input polariser that purifies the polarization and makes it linear. The Faraday medium rotates the polarization by 45° . The exit polariser is set to the same angle to let all the light through. If there is any back-reflection into the isolator the output polariser makes the polarization linear and the Faraday medium rotates that in the same direction by 45° . This makes the polarization of the light perpendicular to the direction of the input polariser and this polariser does not let the light to go back to the laser diode.

The angle of rotation depends on the medium properties and strength of the magnetic field. In these isolators, the magnetic field and the polarisers' directions can be manually adjusted. An iterative process is used to find the optimum orientations of the polarisers and the strength of the magnetic field for the 45° rotation. First step is to take the output polariser, P₂, out and set the input polariser, P₁, to maximum transmission. The P₁ orientation is kept fixed after this step. The second step is to return P₂ to its position and rotate the isolator to isolation direction. With this direction P₂ is changed for maximum isolation. The third step is to return isolator to transmission direction and maximise transmission by changing the magnetic field. Steps two and three must be repeated until they are converged.

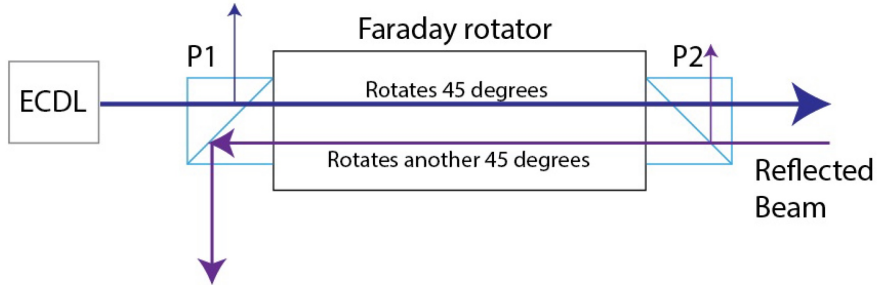


Figure 3.4: A Faraday optical isolator. The input polariser, P1, is set to maximum transmission. The Faraday medium rotates the polarization by 45° and the output polariser, P2, set to the same angle, transmits the light. For a back-reflection the same process rotates the polarization in the same direction and this makes the direction of the polarization perpendicular to the axis of the input polariser, P1. Therefore the polariser rejects the light.(Image courtesy of Valdis Blums)

3.7 370 nm Diode Laser

We use a commercial Moglabs ECDL as our 370nm laser source. This system uses the ECDL configuration described in section 3.5 and the control box for this laser provides current controller, piezo voltage controller and one proportional integral derivative(PID) controller. It is also possible to sweep piezo voltage and monitor different laser properties with this box. This box stabilises diode temperature using negative temperature coefficient thermistor for sensing and Peltier thermoelectric cooler for changing the temperature. At the start of my candidature we used a homebuilt ECDL with Nichia diodes. We experienced sharply reduced lifetime of the diode to one month comparing to one year in the previous diodes. Nichia discontinued manufacturing 20 mW, 375 nm laser diodes and replaced it with 70 mW, 375 nm laser diodes. The new model showed less stability and needed near-perfect feedback setting. We switched to Moglabs laser that shows better opto-mechanical stability and flexibility. After optimizing ECDL configuration in Moglabs laser we achieved 4 pm tuning range near 369.525 nm which matches the specification of this Moglabs model. We use maximum output power of 7 mW after ECDL.

A schematic of our 370 nm laser system is shown in figure 3.5. This system consists of following components:

1. Optical Isolator: This Faraday optical isolator prevents the back reflection, from the optics in the system, from reaching laser diode. Random back-reflections may push the diode to lase in a power higher than specification and may damage the diode. This component protects the diode against this unwanted feedbacks.

2. Wavemeter: This is used for coarse measurement of laser wavelength with accuracy of 1 pm.
3. Polarization Spectroscopy: This component works as an atomic reference to lock the laser frequency to the desired transition frequency for a specific isotope. This part is discussed in section 3.7.2.
4. Fabry-Perot Etalon: This component is used to make sure that the laser is lasing in one mode and it is also used for fast locking discussed in 3.7.2.
5. Off resonant output: This output goes through an Acousto-optic modulator(AOM) and this AOM changes the frequency to 70 MHz red-detuned from the resonance. We also use this AOM as a switch when needed.
6. On Resonant Output: Using an AOM we can continuously tune the frequency of this output from resonant frequency to about 30 MHz red-detuned. This AOM makes a switch to turn the laser on and off for some applications.

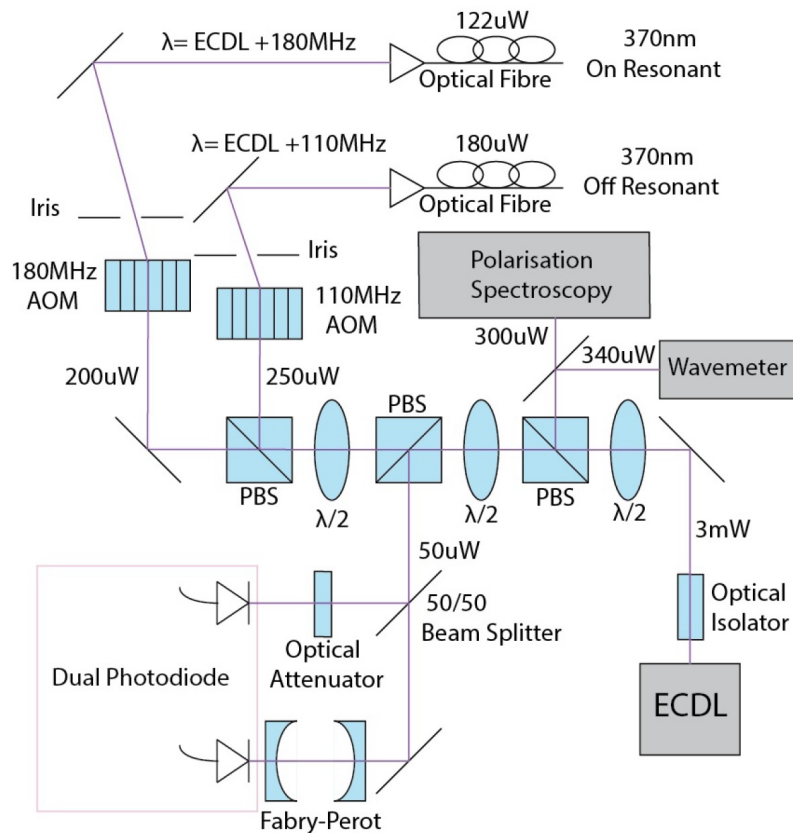


Figure 3.5: A schematic of 370 nm laser system. An external cavity diode laser generates a narrow linewidth laser near wavelength of 370 nm. Half-waveplates and polarizing beam splitters are used to split the power for different components. These components include a wavemeter, polarization spectroscopy system, Fabry-Perot cavity and two outputs with different frequencies for the ion trap. (Image courtesy of Valdis Blums)

3.7.1 Lock-in Amplifier

Lock-in amplifier is an electronic component that is used in our atomic spectroscopy systems. This device accepts a periodic reference input and only amplifies the part of the signal that has the same frequency. The signal to noise ratio, that we normally achieve in our spectroscopic systems, is 10 to 1. This is not enough for having a stable reference to lock the frequency. Noise components in the signal are spread on random frequencies. If we modulate the signal with a reference frequency, we can amplify the signal while keeping the noise at the same level.

The first step in using a lock-in amplifier is to generate a reference signal and use it to modulate the signal and feed it to reference input on the lock-in amplifier. The reference signal can be written as:

$$V = V_{ref} \sin(\omega_{ref}t + \theta_{ref}) \quad (3.9)$$

The modulated signal can be written as:

$$V = V_{sig} \sin(\omega_{sig}t + \theta_{sig}) \quad (3.10)$$

Where V is the signal voltage, ω is the angular frequency and θ is the phase. Lock-in amplifier multiplies reference signal and modulated signal and generates the mixed signal below:

$$V_{mix} = \frac{V_{sig}V_{ref}}{2} \cos([\omega_{sig} - \omega_{ref}]t + \theta_{sig} - \theta_{ref}) - \frac{V_{sig}V_{ref}}{2} \cos([\omega_{sig} + \omega_{ref}]t + \theta_{sig} + \theta_{ref}) \quad (3.11)$$

In the next step, lock-in amplifier uses a low-pass filter and suppresses all the high frequency components. After this stage ideally only the first term in equation 3.11 remains and if the modulation frequency, ω_{sig} , and reference frequency, ω_{ref} , are the same the output is a DC signal:

$$V_{mix} = \frac{V_{sig}V_{ref}}{2} \cos(\theta_{sig} - \theta_{ref}) \quad (3.12)$$

The equation above shows that the amplitude of the signal is dependent on the phase difference; For no phase difference, the signal is maximum and for phase difference of $\pi/2$ it is zero. Even though we use the same generator for modulation and reference signal, they usually have different phases after going through different components. To get the highest signal, using a phase control knob, we apply a phase shift to the input signal to make it in phase with the reference and maximize the signal. Doing this we reach the maximum signal level of $\frac{V_{sig}V_{ref}}{2}$.

There are two other important settings in every lock-in amplifier: sensitivity and time constant. Sensitivity is inversely proportional to the amplification gain. It determines the voltage level that is equal to 1V/gain. Time constant is the inverse of the bandwidth of the low pass filter. By increasing the time constant, the output becomes more steady and easier to measure reliably. The trade off comes when real changes in the input signal take many time constants to be reflected at the output.

3.7.2 370 nm Laser Frequency Stabilization

For laser-cooling, we use 370nm laser which is resonant to $^2S_{1/2} - ^2P_{1/2}$ transition. The linewidth of this transition is 20 MHz and to be able to efficiently cool the ion we need to stabilize laser frequency within a MHz.

We use an improved and very precise version of frequency stabilization with atomic

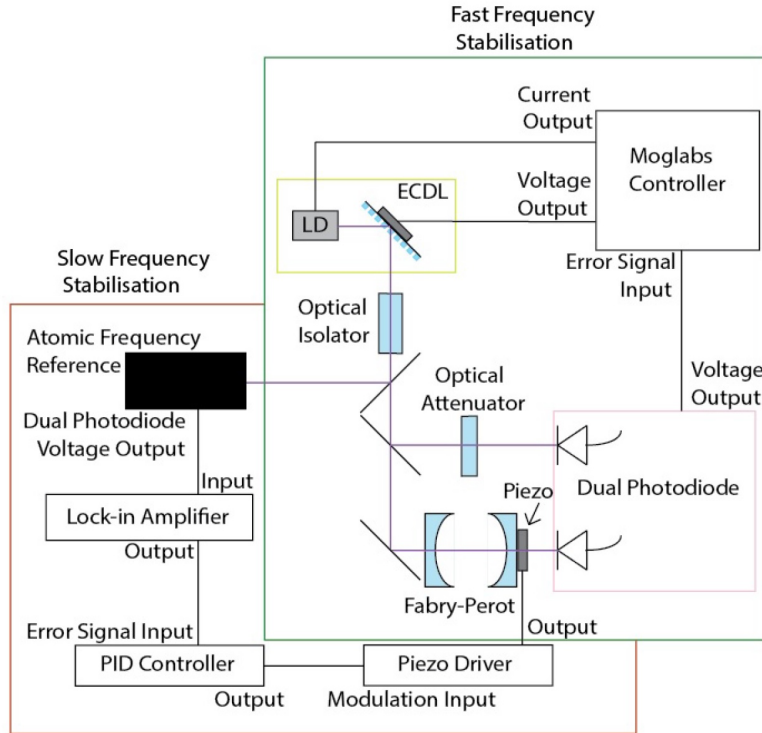


Figure 3.6: A schematic of 370nm laser locking system. Fast lock section uses a signal from a Fabry-Perot cavity to stabilize the frequency. Slower signal that comes from an atomic reference is used to stabilize the Fabry-Perot cavity length.(Image courtesy of Valdis Blums)

reference called saturation polarization spectroscopy. Our frequency locking system consist of a fast lock using Fabry-Perot etalon and a slow lock using an atomic reference(See Fig. 3.6). This two-level system is necessary for fast and reliable laser frequency stabilization for laser-cooling.

The first step of locking is to detect changes in frequency by monitoring changes in Fabry-Perot signal and use a PID controller to compensate for it by changing the external cavity length of the ECDL. A PID controller needs a signal that crosses zero at desired state of the system. To create this signal we use a dual photodiode. Using a beam splitter we send part of the light through the Fabry-Perot cavity and into one of the detectors. The second part goes through a variable optical attenuator and then goes to the second detector. By adjusting attenuator and subtracting signals we set the middle of the Fabry-Perot peaks to zero volt. The middle of the peak is the steepest part of the signal and the best for fast response to frequency changes.

The locking system above works fine as long as Fabry-Perot cavity length stays constant

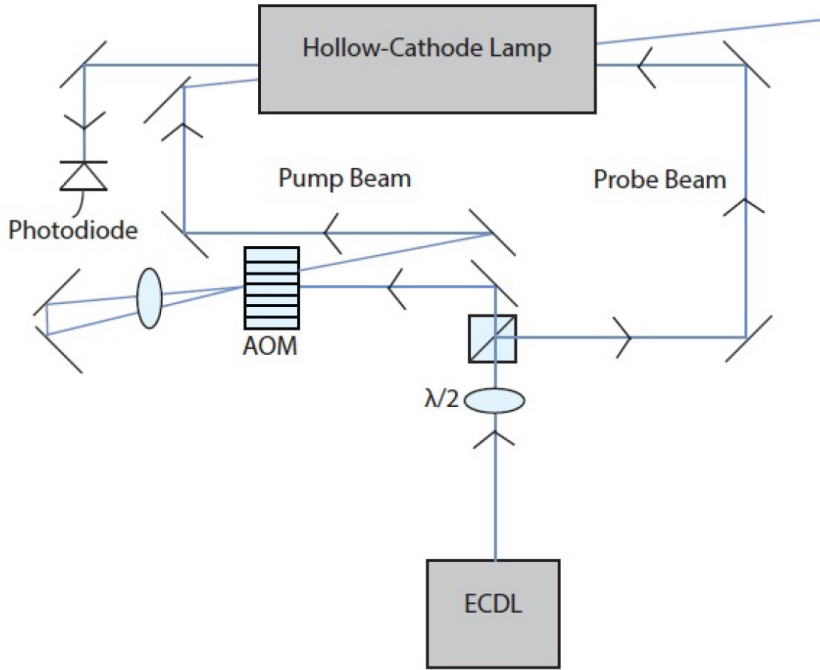


Figure 3.7: Saturation spectroscopy system that uses a powerful counter-propagating beam to eliminate the Doppler broadening of the spectroscopy signal.(Image courtesy of Valdis Blums)

but temperature fluctuation alters the cavity length and shifts the frequency away from the set value. We use an atomic reference to stabilize the Fabry-Perot cavity length. This system is a sub-Doppler spectroscopy system.

We use a 3QQNY/YB Heraeus discharge lamp as an atomic reference. This lamp, which has an Yb cathode, is filled with neon with the pressure of 6 Torr. Voltage applied to the electrodes accelerates stray electrons in the gas and if the voltage is large enough they ionize Ne. The new electrons from ionization also ionize other neon atoms and this creates an avalanche. After ionization, Ne^+ ions start moving towards Yb cathode and sputter Yb throughout the lamp. Neutral Yb atoms are then ionized through Penning interaction with neon ions.

The simplest way of extracting a signal from this lamp is using the linear absorption of laser at resonance but the problem is that because of the Doppler effect this signal is very broad in frequency and it does not resolve the peaks for different Yb isotopes. To eliminate the Doppler effect we use saturation absorption spectroscopy technique(Fig. 3.7). In this technique we add one powerful counter-propagating beam to the previous setup. If we scan the frequency over the resonance and monitor the prob beam, the exact same absorption happen except for the resonant frequency which we observe small or no

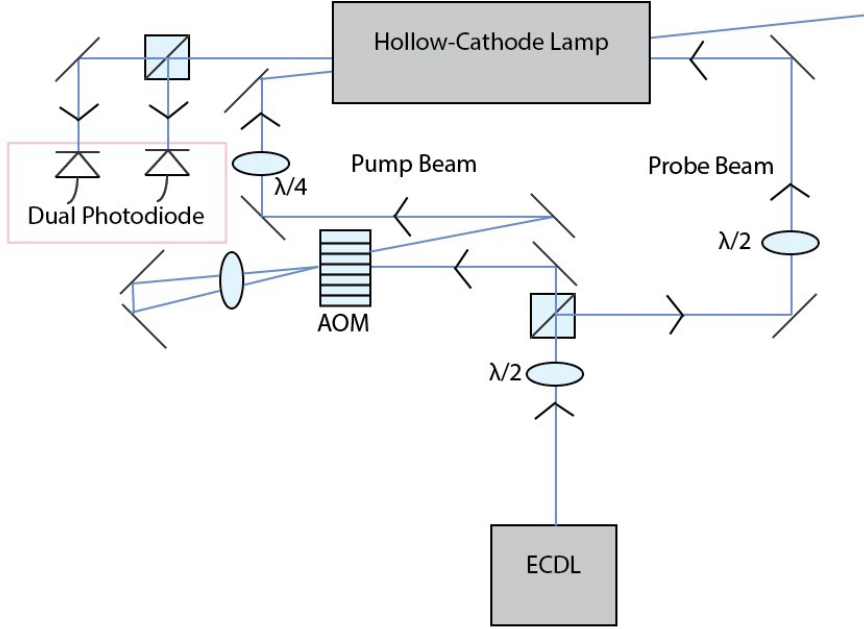


Figure 3.8: A schematic of polarization spectroscopy for 370nm laser. By using a pump beam with circular polarization and a prob beam with linear polarization that goes to a dual photodiode, A narrow zero crossing signal is generated.(Image courtesy of Valdis Blums)

absorption. The reason is that because of the Doppler effect the two beams excite different speed classes of the ions. Only at resonance both beams excite stationary ions. In this situation because most stationary ions are already in the excited state, due to presence of the powerful pump beam, we see much less absorption in the prob beam.

The signal to noise ratio of this signal is not high and to improve it we modulate pump beam with an AOM and use a lock-in-amplifier to amplify the signal(See section 3.7.1). The signal is now sharp enough to resolve different isotopes but it is not suitable for PID controllers that need a zero crossing signal.

To create a zero crossing signal we use the birefringence of Yb ions. From [74] we know that the imaginary part of the complex absorption coefficient is:

$$Im(\alpha) = -\alpha_0 \frac{\gamma(\omega_0 - \omega)}{\gamma^2(1 + I) + (\omega_0 - \omega)^2}, \quad (3.13)$$

Where α_0 is resonant absorption coefficient, γ is the transition linewidth, ω_0 is the resonant frequency and ω is the frequency of the light. This equation shows that a beam experiences a negative phase shift when it is red detuned from the resonance and positive phase shift when it is blue detuned. To use this effect we change our configuration to

what is shown in Fig. 3.8. One of the new components is a $\lambda/2$ waveplate in the prob beam path to be able to rotate the linear polarization of this beam. We also change the polarization of pump beam to $\sigma+$ by adding a $\lambda/4$ waveplate. The prob beam in the new setup, after passing through the lamp, goes through a polarizing beam splitter and goes to a dual photodiode.

To realize what physically happens to the prob beam we need to think of it as an equal superposition of $\sigma+$ and $\sigma-$ light.

$$E_{\sigma+} = E_0(\hat{x} + i\hat{y})\cos(kz - \omega t) \quad (3.14)$$

$$E_{\sigma-} = E_0(\hat{x} - i\hat{y})\cos(kz - \omega t) \quad (3.15)$$

Where E_0 is the amplitude of the electric field, \hat{x} and \hat{y} are unit vectors along x and y , i is imaginary unit, k is the wavenumber and ω is the angular frequency of the electromagnetic wave. If we add these two beams together, they form a linear polarization. The orientation of this linear polarization depends on the phase difference between the two beams. If we apply a $+\theta$ phase shift to the $\sigma+$ beam and a $-\theta$ phase shift to the $\sigma-$ beam, the sum will be a linear polarization that creates an angle θ with respect to the x axis.

$$E_{\sigma+} = e^{+i\theta} E_0(\hat{x} + i\hat{y})\cos(kz - \omega t) \quad (3.16)$$

$$E_{\sigma-} = e^{-i\theta} E_0(\hat{x} + i\hat{y})\cos(kz - \omega t) \quad (3.17)$$

$$E_{\sigma+} + E_{\sigma-} = E_0(\cos(\theta)\hat{x} + \sin(\theta)\hat{y})\cos(kz - \omega t) \quad (3.18)$$

Initially we turn the lamp and pump beam off and set the angle of the polarization of the prob beam to $\pi/4$, so that equal amount of light goes to the different inputs of the dual photodiodes. In this situation the balanced photodiode shows signal of zero.

In order to understand how the photons with circular polarization interacts with ions in the lamp, we need to mention that our lamp has a magnet that quantizes the orientation of the spin of the ions, and therefore half of the ions absorb $\sigma+$ polarized light and the other half absorb $\sigma-$ polarized light. If we turn the lamp on but keep the pump beam off, both beams experience the same phase shift and signal remains zero, regardless of the light frequency. But if we turn the $\sigma+$ pump beam on, it saturates the atoms in resonance with $\sigma-$ portion of prob beam(because they are counter-propagating). This means that the plasma cloud becomes transparent for $\sigma-$ light and it experiences no phase shift. For the $\sigma+$ portion of the prob beam, phase shift depends on frequency. Based on equation

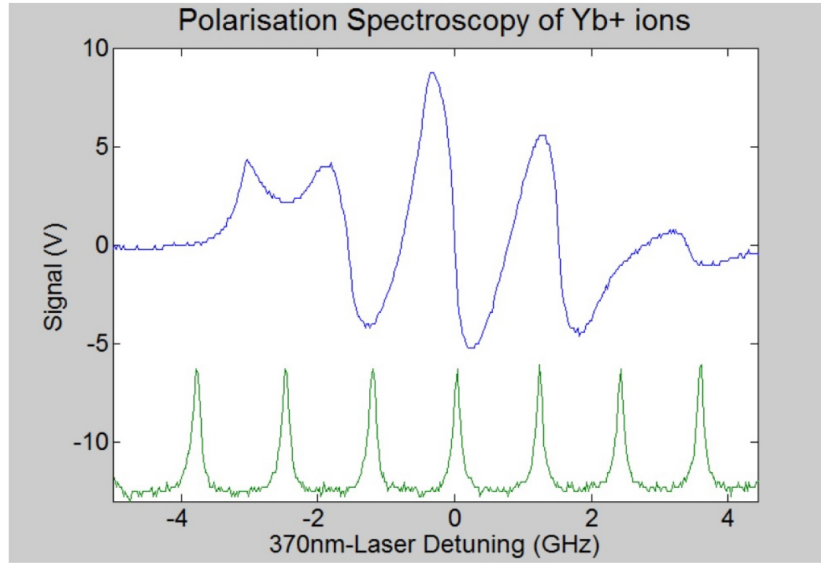


Figure 3.9: Plot of polarisation spectroscopy and Fabry-Perot trace. The blue signal is the polarisation spectroscopy and the green signal is a Fabry-Perot trace. The free spectral range of the Fabry-Perot peaks is 1.25GHz. (Graph after [8])

3.13, this phase shift is zero at resonance, positive on the red side of the resonance and negative on the blue side of the resonance. Looking at equation 3.18 we see that the effect of this phase shift is changing the angle of linear polarization of the prob beam. On the red side of the resonance this angle increases to values greater than $\pi/4$ and changes the balance between horizontal and vertical ratio of linear polarization and this creates a positive signal. On the blue side the exact opposite happens and we see a negative signal. Based on 3.13 far from the resonance the phase shift becomes zero again and signal retunes to zero.

In reality it is not only the phase-shift that is different between saturated and unsaturated components of the prob beam, linear absorption is also slightly different and this leads to slight amplitude imbalance for the two components of the prob beam after the lamp. This means that the polarization will not be perfectly linear but rather slightly elliptical. The effect of this ellipticity on the ratio between horizontal and vertical polarization is much smaller than the phase-shift and it has a small effect on the signal. A graph of the acquired signal is shown in Fig. 3.9.

3.8 399 nm Diode Laser

The 399 nm laser system consists of an external cavity diode laser, an isolator, and a spectroscopy set-up. It is used to excite only ^{174}Yb isotope which is then ionized by the

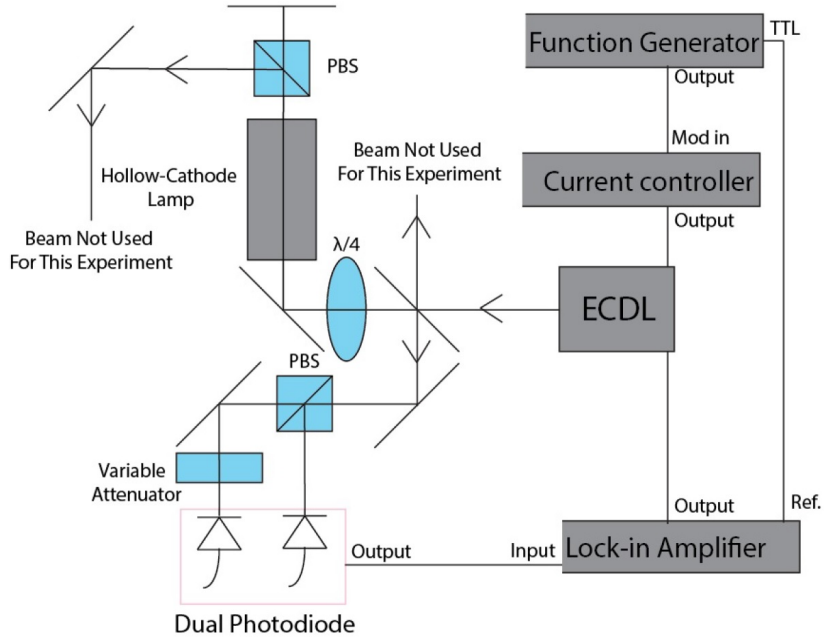


Figure 3.10: Schematic for 399nm-laser polarisation spectroscopy. The first beam through the hollow cathode discharge lamp is a circularly polarised pump beam. After the discharge lamp the beam is split into 2 and a weaker linearly polarised probe beam is sent back through the hollow cathode discharge lamp. The probe beam is then sent to the dual photodiode. The laser frequency is modulated at 20KHz and a lock-in amplifier is used to amplify the signal. (Image after [8])

370 nm laser(See section 3.3).

3.8.1 399 nm Diode Laser Frequency Stabilization

To lock the 399nm laser to the desired frequency we use a sub-Doppler spectroscopy system shown in Fig. 3.10. This system is similar to the 370 spectroscopy set-up(See section 3.7.2) with two main differences. It probes the change in the absorption instead of the phase shift and it uses frequency modulation instead of amplitude modulation.

In this set-up, the portion of the light that is branched for spectroscopy system goes through a $\lambda/4$ wave-plate. This changes the polarization of the light to $\sigma+$. This beam acts as a pump beam. After the lamp, beam goes through a polarizing beam-splitter and a mirror reflects the vertically polarized part of the light back into the lamp. This beam is an equal superposition of $\sigma+$ and $\sigma-$ light (See section 3.7.2 and equations 3.18).

Atoms in resonance with $\sigma-$ part of the prob beam are already saturated with the $\sigma+$ pump beam so this part does not experience a frequency dependent absorption explained by equation 3.19.

After the lamp this part again goes through a $\lambda/4$ wave-plate and its polarization becomes vertical and after going through a polarizing beam splitter, goes to the reference detector in the dual photodiode.

Atoms in resonance with the $\sigma+$ part of the beam are not saturated therefore this part of the beam experiences absorption as explained by equation[74]:

$$Re(\alpha) = \alpha_0 \frac{\gamma^2}{\gamma^2(1+I) + (\omega_0 - \omega)^2}, \quad (3.19)$$

Where α_0 is absorption at resonance, γ is the transition linewidth, I is a dimensionless intensity, ω_0 is the resonant frequency and ω is the laser frequency.

This part of the beam also goes through the $\lambda/4$ and becomes horizontally polarized and the polarizing beam-splitter sends it to the signal detector of the dual photodiode. This means that the signal is zero away from resonance and it becomes negative near the resonance. This is a narrow signal in terms of frequency but still not a zero crossing signal.

We use frequency modulation together with a lock-in amplifier to both amplify the signal and convert it to a zero crossing signal. Suppose that our signal strength is S and we are modulating the laser frequency:

$$f(t) = f_0 + A \sin(\omega t) \quad (3.20)$$

For the limit of small amplitude change we have:

$$S(t) = S_0 + \frac{dS}{df} \times A \sin(\omega t) + O(A^2) \quad (3.21)$$

Because lock-in amplifier only picks up the modulated part of the signal(See section 3.7.1), its output is proportional to the derivative of the signal with respect to frequency (See Fig. 3.11). This shows that not only the strength of the output but also its sign is dependent on this derivative. Therefore the output is positive on one side of the resonance and negative on the other side.

A graph of obtained signal is shown in figure 3.12. We verified this signal by checking the neutral Yb fluorescence on different isotope peaks.

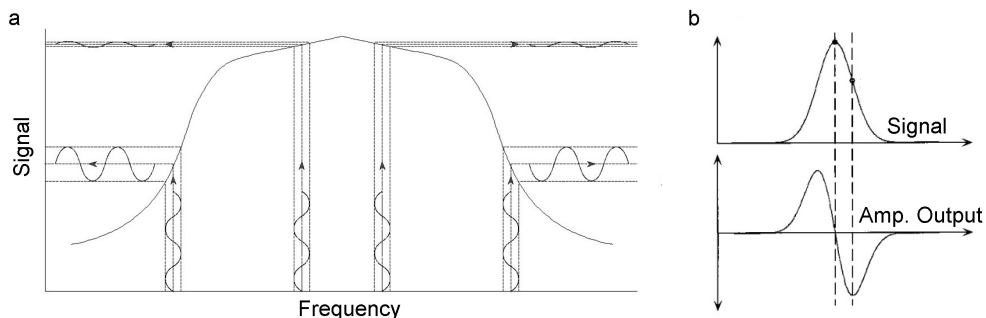


Figure 3.11: a. In a frequency dependent signal, change in signal is proportional to change in frequency times the derivative of the signal with respect to the frequency. b. Lock-in amplifier only amplifies the modulated signal which is proportional to derivative of the signal, therefore its output is positive where derivative is positive and vice versa.

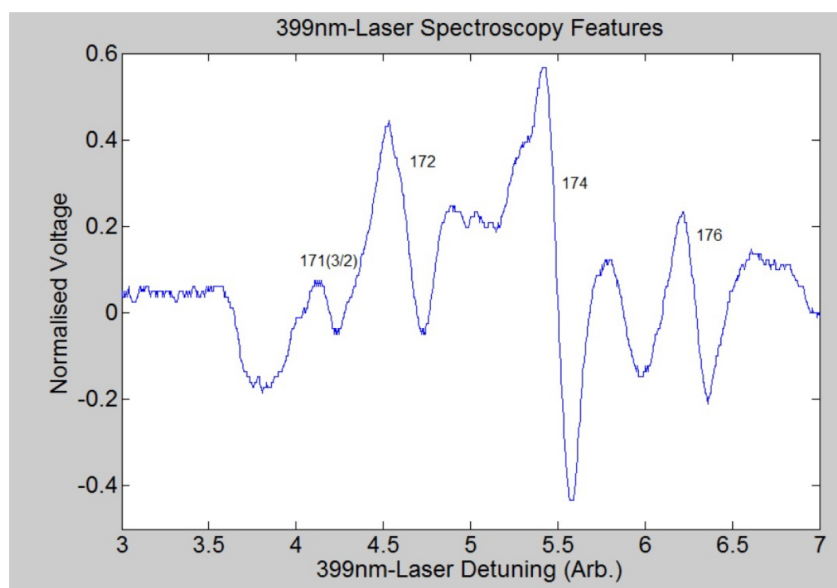


Figure 3.12: 399nm laser spectroscopy trace for neutral Yb. (Graph after [8])

3.9 935 nm Diode Laser

As it is shown in Fig. 3.1, during the cooling process, ion may decay into $^2D_{3/2}$ state. This is a metastable state with lifetime of 53 ms. This slows down the cooling rate significantly. To pump the ion out of this state we pump it to $^3D[3/2]_{1/2}$ using a 935.2 nm laser. From this state, the ion decays back into the ground state in 42 ns. 935 nm laser system consists of a home-built external cavity diode laser, an isolator and a Fabry-Perot cavity. This laser does not have any frequency stabilization system. To make sure that we are efficiently driving the transition, we operate laser at 650uw, which is well above the saturation power, and we also sweep the frequency of the laser. Doing this, we make sure that the transition is saturated even if the center of frequency sweep slightly drifts from the resonance. To trap the ion it is enough to set the frequency roughly to the resonance using a wavelength meter with accuracy of a picometer. After trapping, we maximize the ion fluorescence by manually adjusting the center frequency of the sweep. Because of the thermal drifts, we readjust the center frequency once every half an hour. We sweep the laser frequency by modulating the laser current using a bias-tee. The frequency of modulation is 1 MHz.

3.10 Beam Combiner

All the lasers mentioned above are delivered to the trap using single mode fibres. We use fibres so that we can independently align optics in the ion trap side of the experiment and in the laser set-up. We use a beam-combiner set-up to overlap the beams and send them into the vacuum chamber (Fig. 3.13).

There are 4 inputs to this system. One of them is a 370 nm laser, which its frequency can be tuned from 30MHz red detuned from the resonance upto the resonant frequency. The other one is again a 370 nm laser which is 70 MHz detuned from the resonance. These are combined using a polarizing beam splitter thus have linear polarizations perpendicular to each other. Each of these inputs are equipped with a half waveplate to maximize the power after the polarizing beam-splitter. We use two dichroic mirrors to add 399nm and 935nm lasers to these beams.

These lasers must be overlapped before going to the vacuum chamber. Each fibre is mounted on an adjustable mount and in front of each the fibre outputs there is a mirror that together with the adjustable fibre mounts enable us to set the position and angle for each input. We use a beam profiler to iteratively overlap laser positions with and without a focusing lens.

The last two components of the system are a fast steering mirror and a lens with focal length of 150 mm. The lens is mounted on a translator and is used for precise positioning of the beam. The steering mirror is used to move the beams with the ion during the shuttling.

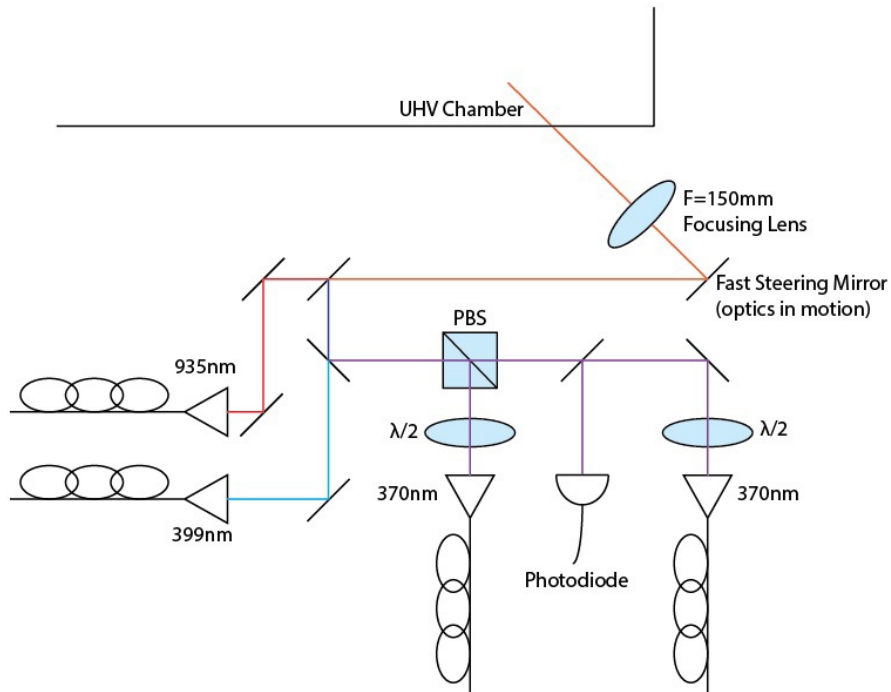


Figure 3.13: Beam combiner setup for lasers in use. The two 370nm laser are combined using a polarizing beam splitter and then 399nm and 935nm lasers are added using diachronic mirrors. A fast steering mirror and a lens mounted on a translator is used for adjusting the position and angle of the beam that goes to the vacuum chamber.(Image courtesy of Valdis Blums)

For the single-photon generation, we need circular polarization for 370 lasers. In this experiment we add a quarter waveplate after the fast steering mirror to turn the perpendicular 370 lasers' linear polarizations into $\sigma+$ and $\sigma-$ polarizations.

CHAPTER 4

Imaging and Optical System

All of my experiments involve Fluorescence collection from the ions and imaging of the ions. For ion imaging and fluorescence collection we use two modes of imaging: bulk optics imaging and integrated diffractive mirror imaging. The first technique only uses external optics and is used for trapping and shuttling. The second technique is implemented when the ion is on top of one of the collimating integrated mirrors. This second mode provides high efficiency fluorescence collection together with high resolution imaging.

4.1 Imaging Using External Bulk Optics

Bulk imaging system enable us to image an ion at every location on the chip (Fig. 4.1). This mode does not use the integrated diffractive mirror therefore has low collection efficiency of approximately 2%. We need this mode of imaging for trapping, shuttling and other diagnostic purposes. Imaging in this mode is implemented using a system consists of two refractive lenses. The first lens is an Asphericon A50-60FPX-U-S with effective focal length (EFL) of 60mm and diameter of 50mm. This lens needs to be positioned a focal length away from the ion to collimates the ion fluorescence. The second lens is a Thorlabs LE4560-UV lens with focal length of 200mm and diameter of 50.8 mm. This second lens focuses the collimated beam, created by the first lens, into a CCD camera and forms an image of the ion. The camera that we use, is an Andor DV437-BU2 CCD. The screen of the camera is an array of 512×512 pixels and each pixel is $13 \times 13\mu\text{m}$ (Fig. 4.1).

The distance of the chip from the vacuum chamber window is not exactly known therefore it is impossible to set the postilion of objective lens first. We know that if the position of this lens is correct, the ion light is collimated after that. Knowing this, we set the distance of the 200 mm lens from the camera to 200 mm and move the position of the objective lens until the chip surface is in focus. To be able to see the chip surface we removed the 150 mm focusing lens(see section 3.10) from the laser beam path to make it wider and use it to illuminate the chip surface. During this set-up, while the laser is shining on the chip, the RF voltage must be off, otherwise the trap will be charged. As a scondary test to make sure that the objective lens position is correct, we attached the 200 mm lens to the camera and moved both of them together; If the light is collimated after

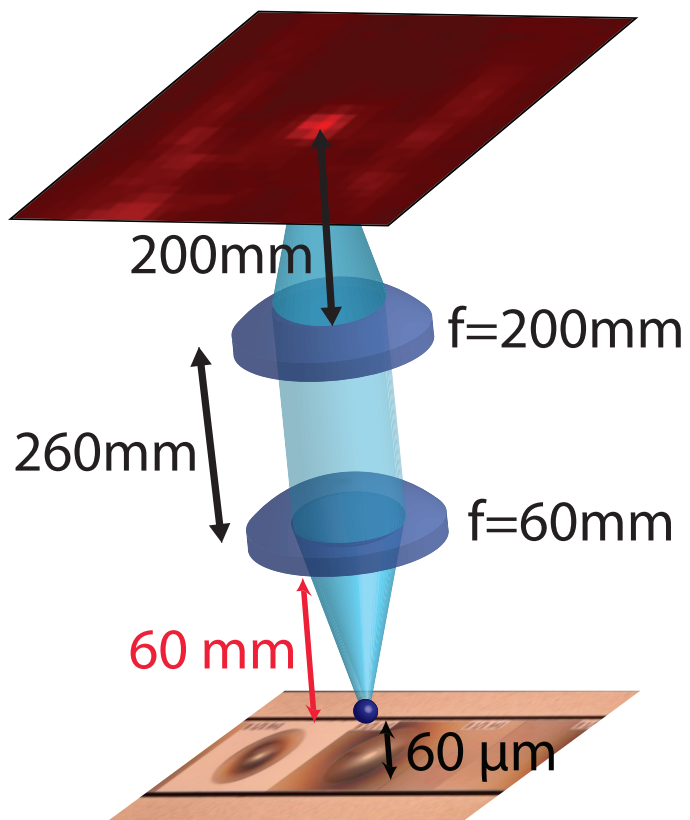


Figure 4.1: A schematic of the lens configuration in the bulk imaging mode (Image is not to scale). Ion is located $60\mu m$ above the chip. The objective lens with focal length of $60mm$ is positioned $60mm$ away from the ion. This lens collimates the ion fluorescence. The collimated beam is focused on the camera using a second lens located $260mm$ away from the objective lens.

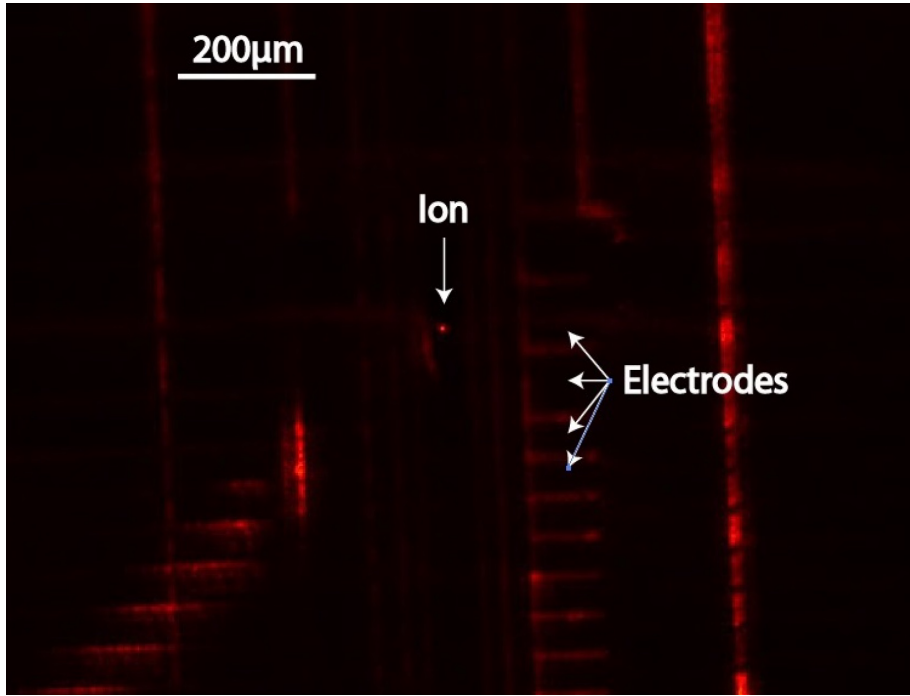


Figure 4.2: An image of the chip and a trapped ion located at loading zone captured using bulk imaging system. Ion is located the middle of the loading zone. The oval shaped scatter around the ion is the reflection of laser from the edge of the loading zone. DC electrodes are visible on both sides of the ion.

the objective lens the chip image must remain focused regardless of camera position. After this test, the 200 mm lens was detached from the camera and placed 260mm(sum of the focal lengths) away from the objective lens. This initial setting does not guarantee that ion will be in focus, when trapped, and this was one of the reasons that the first trapping of the ion was hard and time consuming. After trapping, we optimize the objective lens position and reset the distance of the two lenses to the sum of the focal lengths. Fig. 4.2 shows an image of an ion at the loading zone realized with the this optical system. In this image DC electrodes are also visible on both sides of the ion. The oval shaped glow around the ion is the reflection of the laser and the ion light from the edge of the loading zone.

The objective lens is a high NA lens that creates an aberrated image if operated off conjugate. To make sure that both lenses are not tilted, we used two irises on both sides of each of them and found the tilt angle that enable us to image the ion even with the minimum aperture of irises. This proves that the imaging axis passes the center of the lenses and is perpendicular to lenses' surface. Using the two irises attached to the camera, we also made sure that the imaging axis is perpendicular to the camera's imaging screen.

After trapping, using the scheme described in section 2.2.1, we shuttled the ion to

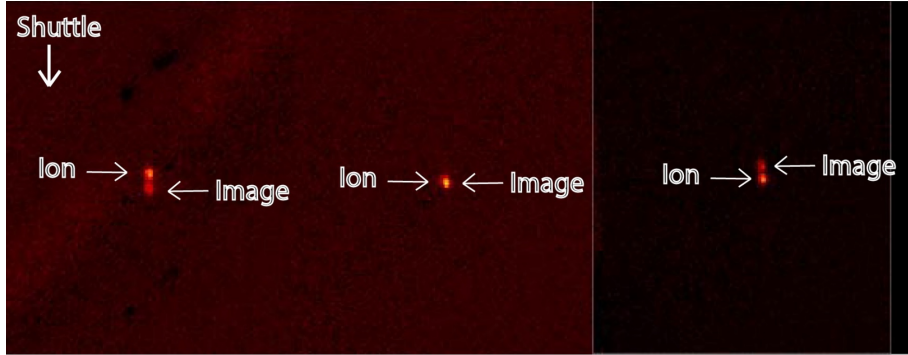


Figure 4.3: Three images from the ion and its image created by the self-imager diffractive optic for different ion positions. This optic forms an image from the ion on itself. left: the ion is located before the self-imager. middle: the ion is located on top of the self-imager. images are almost overlapped and this shows that we have small lateral mismatch between optics fabrication ad electrodes fabrication. right: the ion located after the self-imager optic

different regions of the chip. One of the integrated optics that we checked was the self-imager. This optic focuses the ion light into ion itself. Figure 4.3 shows three images of the ion and its secondary image, at three different locations near the center of the self-imager. The image shows that both the direct and indirect images of the ion are in focus. This means that the image is at the same height of the ion. Therefore the ion height is the same as the designed focal length of the optic which is equal to the nominal ion height of $58.6\mu m$. The middle image shows that images are almost overlapped. This means that the ion position has a very small lateral offset comparing to the center of the optic. This shows that the lateral mismatch between the fabrication of diffractive mirrors and the chip electrodes is very small.

4.2 Diffraction-limited Imaging(Theory)

In the 19th century Lord Rayleigh developed a criterion for the ability to resolve two point sources in an optical system. He showed that the resolution of an optical system has a limit imposed by diffraction. If one images a point source with an optical system of circular input aperture of radius a , the image looks like the Airy function shown in Fig. 4.4. This means that the image is not confined to a point but it has a central bright peak in the middle and the intensity goes to zero at $\theta = 1.22\lambda/2a$ (λ is the wavelength of the light) and then again we have series of lower intensity peaks. The exact intensity profile is:

$$I(\theta) = I(0) \left(\frac{2J_1(\rho)}{\rho} \right)^2 \quad (4.1)$$

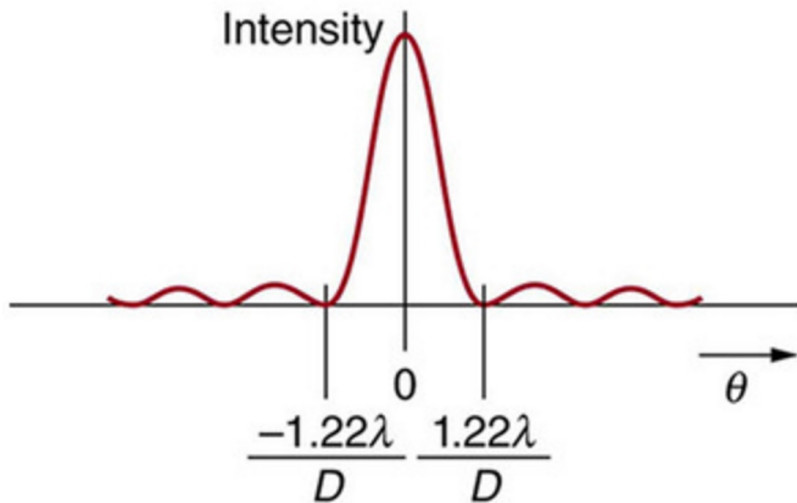


Figure 4.4: Graph of intensity of the diffraction pattern for a circular aperture. (Source: boundless.com)

$$\rho = \frac{2a\pi \sin(\theta)}{\lambda} \quad (4.2)$$

Where $I(0)$ is the maximum intensity, J_1 is the first order Bessel function, a is radius of the aperture and λ is the wavelength of the light. With this diffractive effect if one tries to image two point sources that are too close to each other their intensity profile overlaps and they become unresolvable. Rayleigh criterion is that they are resolvable when peak of one source coincides with the first trough of the other, that is their angular separation is $\theta = 1.22\lambda/2a$.

In the case that the optics add aberrations to the image, the width of the middle peak becomes larger; therefore having an image with the same intensity profile as the theoretical profile is an indication of aberration free imaging. If we ignore the surrounding peaks, the closest Gaussian profile to the middle peak is a profile with FWHM diameter of:

$$D = 0.43 * \lambda/NA \quad (4.3)$$

In which $NA = \sin(\alpha)$ is the numerical aperture of the optical system(Fig. 4.5). An aberration free imaging system, that creates an image with the diameter D from a point source, is diffraction limited.

Spot size is not the only property of the beam that changes due to aberration; divergence of the beam may also increase if the beam is not perfect. Transverse irradiance profile of a Gaussian beam is shown in figure 4.6. For a Gaussian TEM_{00} mode, if the

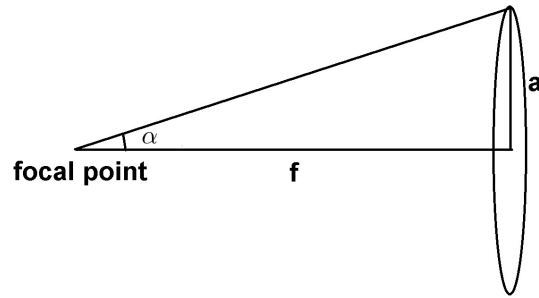


Figure 4.5: Numerical aperture (NA) of an optical system is a dimensionless number that characterizes the range of angles over which the system can accept or emit light. It is equal to $n \sin(\alpha)$, where n is the index of refraction of the medium and α is half of the acceptance angle.

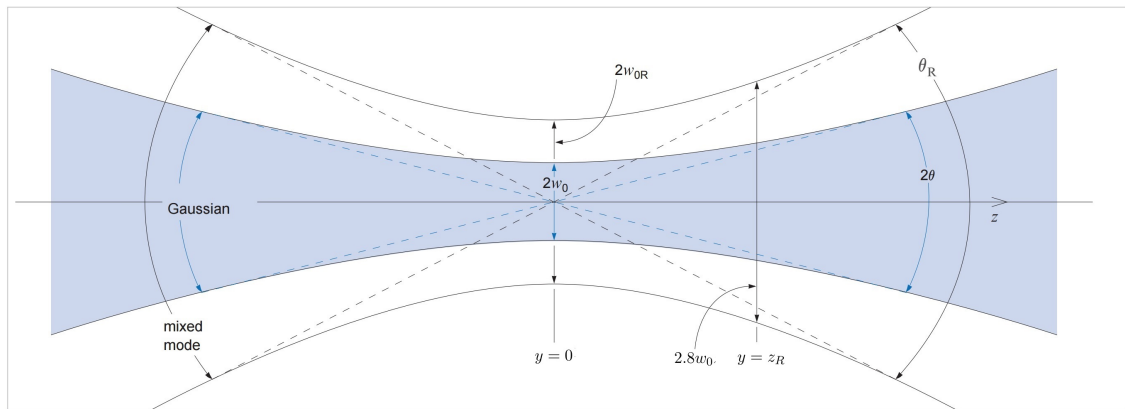


Figure 4.6: $1/e^2$ irradiance size of a Gaussian beam. w_0 and θ are the radius and the angle of the far-field divergence of the ideal zero order Gaussian beam and w_{0R} and θ_R are the radius and the angle of the far-field divergence of the mixed mode beam (image source:idexop.com)

$1/e^2$ radius of irradiance of the beam at focus is w_0 , The size at a distance y from the focus is[75]:

$$w(y) = w_0 \sqrt{1 + \left(\frac{y}{z_R}\right)^2} \quad (4.4)$$

where $z_R = \frac{\pi w_0^2}{\lambda}$ is Rayleigh range and is a measure that shows how divergent the beam is. For $z \gg z_r$ the angle of divergence is:

$$\theta = \frac{\lambda}{\pi w_0} \quad (4.5)$$

For any Gaussian beam, zero order or mixed mode, the product of the radius at the focus, w_{0R} , and the far-field divergence angle, θ_R , is constant. This enable us to define a dimensionless constant for the beam that is used as a measure of imperfection of the beam:

$$M^2 = \frac{w_{0R}\theta_R}{w_0\theta} \quad (4.6)$$

This constant is equal to one for Gaussian TEM_{00} mode and it is greater than one for mixed mode beams. This shows that it is possible to match the size or divergence of an imperfect beam to an ideal beam but it is impossible to match both. In applications like fibre coupling both the size and the divergence of the beam must be matched to that of the fibre and this equation shows that it is impossible to do this for a mixed mode beam. Therefore losing part of the power in fibre coupling becomes inevitable.

M^2 cannot be determined with only one size measurement. Based on ISO/DIS 11146 M^2 calculation needs at least 5 profile measurement at focus and 1 and 2 Rayleigh ranges away from the focus on both sides. It is possible to approximate the divergence angle of the beam with $\theta_R = \arctan(\frac{w(2z_R)}{z_R})$ and insert it to equation 4.6 and calculate M^2 but the more accurate way to do that is to fit parametric function below to the data points and calculate the M^2 of the beam:

$$w = w_0 \sqrt{1 + \left(\frac{(y - y_0)\lambda M^2}{\pi w_0^2} \right)^2} \quad (4.7)$$

To use this formula to measure M^2 , we take 5 images around a focus point of the beam and use two Matlab(TM) routines that I developed: *Ion_size* and *M2_Calc*.

Ion_size receives a saved image from the camera in the ASC format and returns the size of the ion in two dimensions. In the first step, it identifies the ion position and cuts the image around the ion and then fits a two dimensional Gaussian profile to the image:

$$f(x, z) = A \exp \left(- \left(\frac{(x - x_o)^2}{\sigma_x^2} + \frac{(z - z_o)^2}{\sigma_z^2} \right) \right) \quad (4.8)$$

where A is the maximum intensity, x_0 is the ion position along the x direction, σ_x is the $1/e^2$ size of the image along the x direction, z_0 is the ion position along the z direction and σ_z is the $1/e^2$ size of the image along the z direction.

M2_Calc receives the ion image sizes and the corresponding camera positions as input and outputs M^2 values and focus positions and focus sizes for the two axes, by fitting the equation 4.7 to the data. An example of the output of this program for the ion beam is shown in figure 4.7.

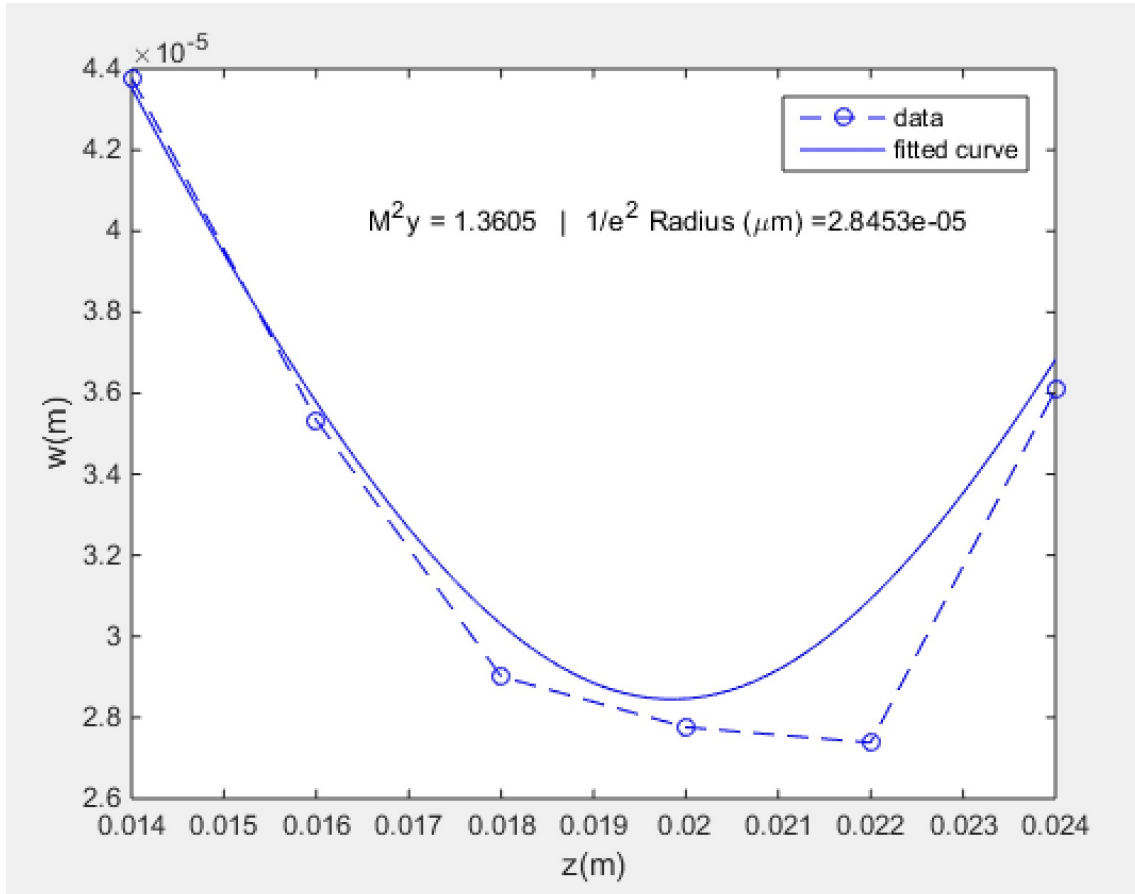


Figure 4.7: An example of measuring M^2 by fitting equation 4.7 to the spot sizes around the focus point for the optical configuration shown in Fig. 4.10. The blue circles are the measured radii and the solid line is the fitted function. In this case M^2 is 1.36 which suggests that our beam is slightly aberrated.

4.3 Imaging Using Microfabricated Collimators

After the initial trapping, in the first attempt, we tried to capture an image using the collimator at loading zone. This part of the experiment was discussed in section 2.3.4. The next step was to shuttle the ion to 4th collimator on the chip, according to procedure discussed in section 2.2.1 .

The optical telescope, used in bulk imaging, do not focus the light reflected from the diffracted mirrors on the camera screen.

To focus and image the light from the mirrors, we need to change the setting of this optical system or add some more lenses to bring that into focus. To be able to easily switch between the two modes, we left the bulk imaging lenses untouched and decided to add lenses to the system to focus the light collected by the mirrors. To set-up this new imaging system we needed to predict and calculate the beam behaviour through the

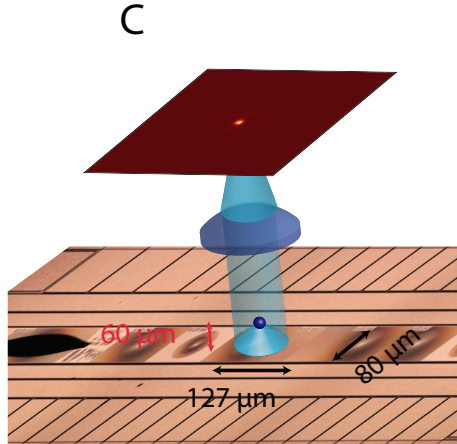


Figure 4.8: Imaging using integrated collimating mirrors. The collimated light can be focused on the screen using a second lens. This method can be used if the distance between the mirror and the axillary lens is less than Rayleigh range of the beam which is 8.7 mm for one axis and 5.1 mm for the other axis. In our system the distance between the mirror and the first lens is 60 mm . This distance is much greater than the Rayleigh range of the beam and beam will be diverging when it reaches the lens. Gaussian beam simulation must be used to predict the evolution of the beam and design an optical system to image the light collected with the mirrors.

optics. One might naively think that the ion light from the collimator remains collimated until it reaches the first objective lens and then it can be focused by this lens (Fig. 4.8). Correctness of this assumption depends on the Rayleigh range of the beam and the distance between the mirror and the lens. The calculation of the Rayleigh range for an ideal Gaussian beam collected with the 4th collimator on the chip, shows that the Rayleigh range is 8.7 mm for the larger axis of the beam and 5.1 mm for the smaller axis of the beam. This shows that after travelling 60 mm to the first objective lens, the beam is not collimated any more. In fact at this point the beam is in the far-field diverging regime. The calculation of Rayleigh range was made by assuming that the beam starts with diffraction limited spot size at the ion position. Ion is located a focal length away from the mirror which is $59.6\mu\text{m}$ for the 4th collimator. Based on equation 4.3, the diffraction limited size depends on the mirror NA which is different for the two axes. Along the larger side of the mirror, which we call z axis, $NA = \sin(\theta) = 0.73$ (Fig. 4.9) and along the shorter side (x axis), $NA=0.56$. The diffraction limited size calculated using equation 4.3 and is 285 nm for z axis and 218 nm for x axis. From the ion position to the mirror, the beam evolves according to equation 4.4 and using this equation shows that the size at the mirror

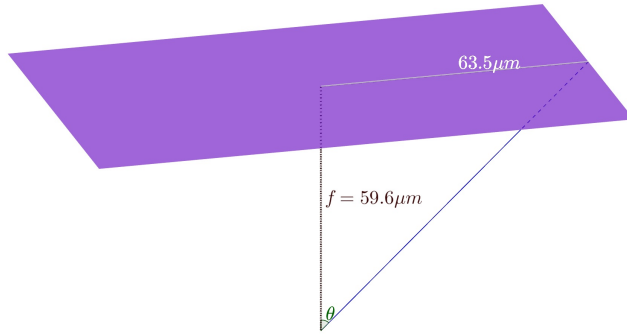


Figure 4.9: Numerical aperture(NA) of the mirror for the z axis. The distance from the ion to the mirror is $59.6 \mu m$ and the half side of the mirror along the z axis is $63.5 \mu m$. Therefore $NA = \sin(\theta) = 0.73$.

is $32 \mu m$ for the z axis and $24 \mu m$ for the x axis. The mirror collimates this diverging beam coming from the ion. The spot size of this collimated beam is $32 \mu m \times 24 \mu m$ and this is equivalent to Rayleigh range of $8.7 mm$ and $5.1 mm$. After travelling $60 mm$ to the objective lens the beam is closer to a diverging beam from a point source rather than a collimated beam. Due to the different sizes in two axes, we experience astigmatism. To be able to predict the behaviour of the beam, I developed a simulation program with Matlab(TM) that is explained in the next section.

4.3.1 Gaussian Beam Propagation Simulation

To Simulate the behaviour of the ion beam we used ABCD analysis [75]. In this type of analysis for Gaussian beams, we use the beam complex parameters q :

$$\frac{1}{q(y)} = \frac{1}{R(y)} - \frac{i\lambda}{\pi w(y)^2} \quad (4.9)$$

Where R is the radius of curvature, i is the imaginary unit, λ is the wavelength of the light and w is the beam waist. The evolution of the beam in free space is based on:

$$q(y') = q(y) + d \quad (4.10)$$

Where d is the distance between y and y' . When a beam goes through a thin lens with focal length f , q' after lens is:

$$q' = \frac{q}{1 - \frac{q}{f}} \quad (4.11)$$

I wrote a Matlab routine to use these equations to simulate the propagation of the

beam. The Matlab routine receives mirror size, ion distance from the mirror, lenses' positions and lenses' focal lengths as input. In the first step the program calculates NA for the two axes based on mirror size and ion distance from the mirror. Having NA, it uses equation 4.3 to calculate the ideal size of Gaussian beam at the ion. From here it uses equation 4.10 to calculate q just before the mirror. The next step is to apply equation 4.11 to calculate q just after the mirror. From here it calculates evolution of q in free space with steps of one mm and applies lens effect where it reaches a lens.

To prepare an output it calculates an array of beam sizes, w , and radius of curvature, R , for each mm using equations below:

$$R = \frac{1}{\text{real}(1/q)} \quad (4.12)$$

$$w = \sqrt{-\frac{\lambda}{\text{img}(1/q)\pi}} \quad (4.13)$$

Where λ is the wavelength, $\text{real}()$ is function that returns real part of a complex number and $\text{img}()$ is a function that returns the imaginary part of a complex number. The program also calculates the Rayleigh range after each lens and identifies focus points and their sizes and magnifications. Finally it plots the evolution of the beam for two axes and adds the calculated values to the graph.

Fig. 4.10 shows the output of the program for one of the optical setups that we use for beam transfer.

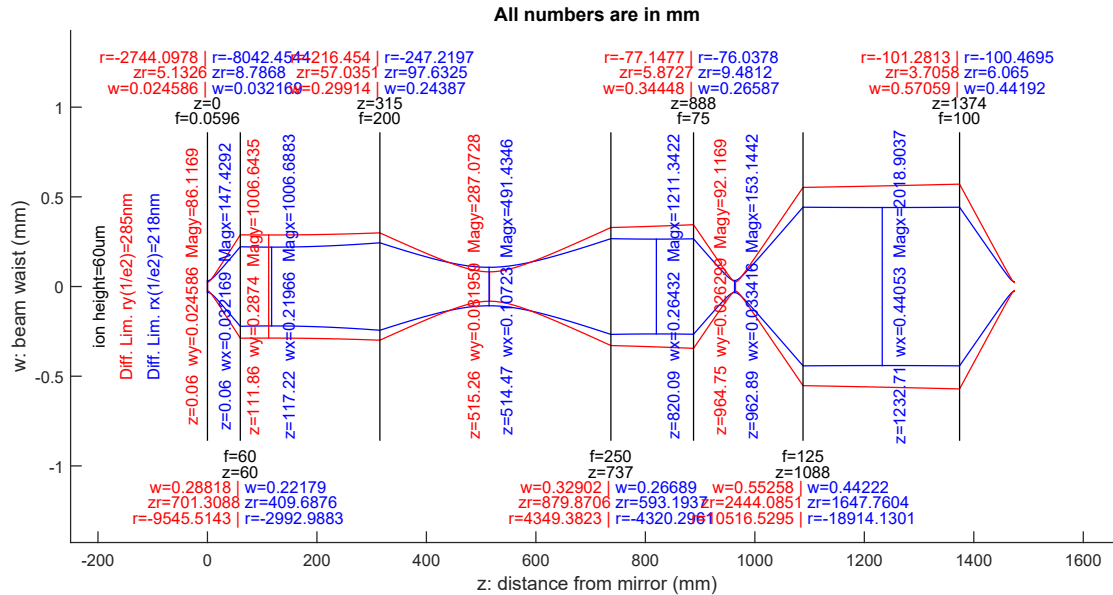


Figure 4.10: Gaussian beam propagation simulation for one of the settings we used for beam transfer. Blue curve shows the size of the beam in the x direction and red curve shows the size of the beam for z direction. Vertical black lines are lenses with f their focal lengths and z their distances from the diffractive mirror. r , zr and w labels, next to the focal length label, are radius of curvature, Rayleigh range and beam size respectively. Vertical blue and red lines show the focus points and for each axis the beam size, focus position and magnification is shown with respective color next to them. On the left side it displays the diffraction limited size at ion position for each axis.

4.4 Near Diffraction-limited Image

After simulating the beam propagation and setting up proper optics we captured images using different collimators that we have on the chip. The focal lengths of these four collimators are 58.6(+0), 60.6(+2), 62.6(+4), 59.6(+1) μm . The ion is more stable when its height is at nominal $58.6\mu m$ or lower therefore we expected to get the best image with our first collimator in the array which has a focal length of $58.6 \mu m$. We captured an image using this collimator but unfortunately it is too close to the loading zone and ion is unstable at this position.

Another more important problem with this collimator was that when we tried to position the ion at the center of this collimator in the z direction(along RF lines) we captured a distorted image which was apparently being blocked partly by some object. This object turned out to be the conducting mesh on the top of the chip that is placed to protect the chip from stray fields. This mesh is very thin and does not have any visible effect on normal external imaging but unfortunately one of the mesh lines is located

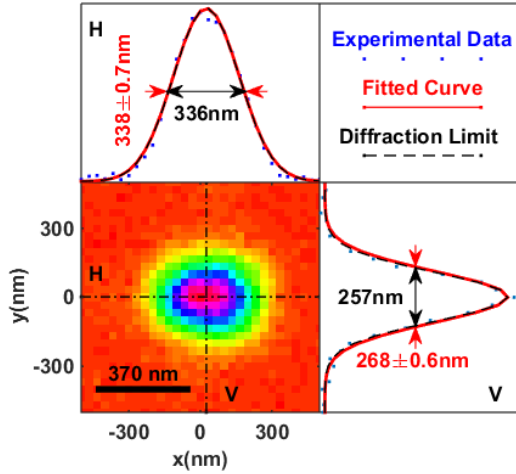


Figure 4.11: Near diffraction limited image of an $^{174}\text{Yb}^+$ ion obtained using integrated diffractive mirror and comparison with diffraction limited size. Solid angle coverage is 13.3% and exposure time is 1 second. Ion image size measured to be $338(1.6)\text{nm} \times 268(1.2)\text{nm}$ FWHM diameter.

directly above the center of this collimator. Therefore it is only possible to image the ion by positioning ion $1\mu\text{m}$ away from the center of the collimator in the z direction. This adds aberration to the image and increases the M^2 value of the beam. this means that the beam size is greater than the diffraction limited size.

The next best option was the 4th collimator which has a focal length of $59.6\ \mu$ ($1\mu\text{m}$ higher than nominal height). To capture an image we set-up the optical system shown in Fig. 4.10. In general imaging set-up does not need to be this complicated and have 6 lenses. The first two lenses are the ones that we use for bulk imaging and we did not want to remove them. The remaining lenses are only used for resizing the beam for the fibre coupling experiment(section ??). In principle only one lens is enough to focus the light on camera if there is no positioning and distance constraints. Using this system we captured the image shown in Fig. 4.11.

To be able to capture this almost diffraction limited image, we needed to optimize 2 important set of parameters:

1. external optics positioning and orientation
2. ion position relative to diffractive mirror

To have the best image, ion beam must go through the center of the external lenses and must be perpendicular to the lenses. To align the first two lenses in the setup , *i.e.* the 2" 60mm objective lens and the 200mm lens, we mounted them on two 3-axes translators for

accurate positioning and adjustable mirror mounts to set the angle. We attached two irises before and after each lens and iteratively made irises tighter and tighter and optimized position and angle to get clearest and brightest image of the surface of the chip.

The next task was to optimize the ion position. Our convention for direction is to label the axis along the RF lines z , perpendicular to the chip surface y and the lateral direction x . Along the z direction DC harmonic potential confines the ion so we can position the ion finely without adding to the micro motion. We do this by setting position in the chip trap control program and we use accuracy of 100nm to position the ion. From our design we know the position of the centre of the mirror within few μm . By moving the ion over that region we saw that we get a round and clear ion image within a distance of $2\mu m$ and outside that ion image starts to become distorted. We set the ion position to the center of this region. This center is located at $871.1\mu m$ away from the loading point.

Along the x direction we move the ion using a set of voltages named `Ex_Comp` waveform(see section 2.2.1). This set of voltages are designed to apply $1000V/m$ along the x direction to the ion. We use a scalar parameter `Ex_Comp_Weight` to scale this electric field and apply the desired field to the ion. Moving the ion in this direction increases the micro-motion of the ion and eventually leads to the loss the ion. Even though the best E_x for cancelling the stray fields is position dependent, `Ex_Comp_Weight` is usually between -0.2 and $+0.2$. This is equivalent to applying an electric filed between -200 to $+200 V/m$ to the ion. Normally we lose the ion when the `Ex_Comp_Weight` is set to greater than 0.7 or smaller than -0.7 . At the center of the 4th collimator, `Ex_Comp_Weight=0.1` is the best field that minimizes the micro motion. We find this parameter by setting the laser frequency $5 MHz$ detuned from resonance and find the `Ex_Comp_Weight` that maximizes the ion fluorescence in external imaging mode. For imaging with the collimator we capture a round small image for $0 < \text{Ex_Comp_Weight} < 0.4$. Outside this range the image becomes skewed and the image size starts to increase. We use `Ex_Comp_Weight=0.2` for imaging and this does not have a significant effect on the micromotion.

Position in y direction or the ion height is the most important parameter that can affect the image quality. Ideally we want to have the ion exactly at the focus of the collimator. The nominal ion height is shown in figure 4.12. This is based on simulation of the RF and DC field done by GTRI and never confirmed experimentally. Therefore we can only roughly guess that ion height is $58.6\mu m$ when we apply no field along the y direction. For the 4th collimator with the focal length of $59.6\mu m$ we need to apply a positive E_y (away from surface of the trap) to push the ion $1\mu m$ higher but the exact amount of electric field for this displacement is also unknown. To find the right height we used the imaging simulator described in section 4.3.1. We created a list of different ion heights and simulated image focus position relative to the last lens before camera. Then we applied a set of different E_y fields and created a table of E_y vs camera focus point. Because the dimensions of our mirror is asymmetric, the image suffers from astigmatism

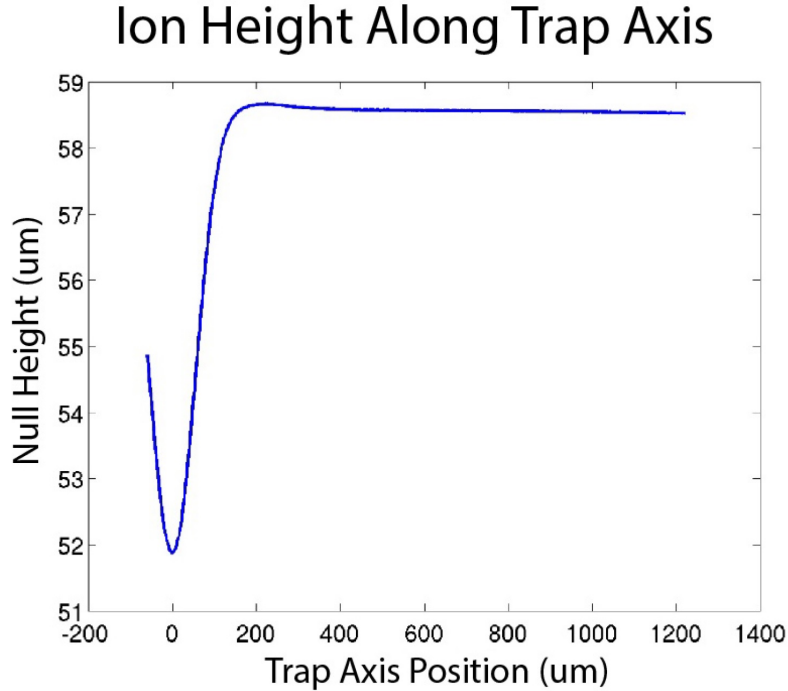


Figure 4.12: The ion height for the different positions of the ion on the chip. When at the middle of the loading zone the ion height is $52 \mu\text{m}$. Ion height gradually increases by moving away from the loading point and becomes $58.6 \mu\text{m}$ outside of the loading zone. (GTRI)

and this makes it hard to recognise the focus point. For each ion height we saved a set of five images around the focus point and fitted a Gaussian beam profile to find the focus for each axis. By comparing to the simulation we found out that `Ey_Comp_Weight=0` corresponds to the height of $58.6 \mu\text{m}$ and `Ey_Comp_Weight=0.5` corresponds to the height of $59.6 \mu\text{m}$. We confirmed this results by doing the same procedure for the 1st collimator with the focal length of $58.6 \mu\text{m}$.

After finding all the right parameters and aligning external optics we captured the image shown in Fig. 4.11. To be able to compare the image size with the diffraction limited size, we scaled the image size on camera by the magnification of the optical system. To measure the magnification, we moved the ion $1 \mu\text{m}$ towards the $-z$ direction and $1 \mu\text{m}$ towards the $+z$ direction and captured two images. We fitted a Gaussian profile to these images and knowing the camera pixel size, which is $10 \times 10 \mu\text{m}$, we calculated that it moves $780.0(2) \mu\text{m}$ which is equivalent to Magnification of 390X.

Fitting a Gaussian profile to the captured ion image and dividing the sizes by magnification of 390 we arrive at near diffraction limited spot size of $338(0.7) \text{ nm}$ horizontal (H) and $268(0.6) \text{ nm}$ vertical (V), FWHM diameter. This is the highest resolution imaging of an ion, with an integrated optic, without aberration correction, reported to date and only

is slightly larger (0.6% for horizontal and 4% for vertical) than the diffraction limited size of 336 nm (H) and 257 nm (V).

To characterize the mode quality we took 5 images of the ion by defocusing camera around the focus point and found the M^2 of the beam as described in section 4.2. The M^2 , mode quality, of the spot was 1.36 (H) and 1.54 (V), compared to an ideal Gaussian beam with $M^2 = 1$. Other than design imperfections, this slightly non-ideal behaviour is driven by the increased divergence in the beam due to astigmatism and the fundamentally non-Gaussian distribution of the ion's photon emission.

CHAPTER 5

Single Photon Generation

To demonstrate a quantum mechanical application we designed and implemented a single photon generation scheme that can be used for quantum communication applications. This also provides a method to rigorously demonstrate collection efficiency of the diffractive mirrors. Conventional method for demonstration of the collection efficiency is to use the cooling cycle and calculate the number of photons that an ion is emitting and compare it with the number of photons that is collected. The fluorescence counts depends on the intensity of the laser and frequency detuning from the resonance. The fluorescence rate is given by[70]:

$$\gamma_p = \left(\frac{s_0}{1 + s_0} \right) \left(\frac{\gamma/2}{1 + (2\delta/\gamma')^2} \right) \quad (5.1)$$

where s_0 is the saturation parameter, γ is the linewidth of the transition, $\gamma' = \gamma\sqrt{1 + s_0}$ and δ is the detuning from the resonance. This calculation depends on many assumptions and not fulfilling them adds errors to the value. One assumption is that the laser frequency linewidth must be much narrower than transition linewidth. Repumper laser power must also be saturating its transition. Laser power must be stabilized to make sure that intensity remains constant. Another important point is to know the focus size of the laser and its intensity at the focus. We also need to make sure that laser is focused at the ion.

With on-demand deterministic single photon generation, we do not need to rely on the accuracy of this calculation. We generate a known amount of photons and compare them with the number of the collected photons.

5.1 Atomic Transitions, Absorption and Emission Patterns

In the process of generating single photons, to excite the ion, we use lasers with circular polarizations. In this process emitted photons from the ion can have linear, π , or circular, σ , polarization. In order to explain the protocol, it is necessary to know the absorption and emission patterns for these polarizations.

For our single photon generation protocol, we use the usual ${}^2S_{1/2}$ - ${}^2P_{1/2}$ cooling transition with wavelength of 370 nm. Figure 5.1 shows the excitation and decay process

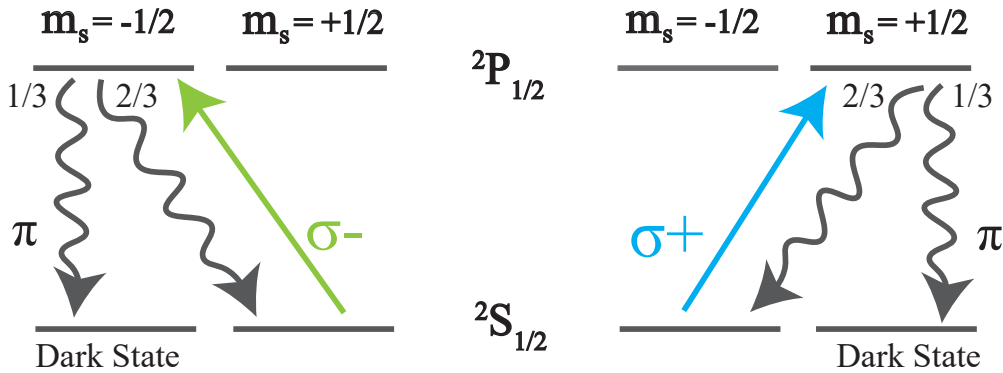


Figure 5.1: Relevant transitions for the single photon generation protocol. The 370 nm $\sigma-$ laser can only excite $^2S_{1/2}m_s = +1/2$ to $^2P_{1/2}m_s = -1/2$ transition. The excited ion may emit a σ photon, with probability of $2/3$, and return back to $m_s = +1/2$ ground state or it may emit a π photon, with probability of $1/3$, and fall into $m_s = -1/2$ state. This is a dark state for $\sigma-$ laser and ion does not interact with the laser while in this state. For the $\sigma+$ laser, after excitation, the ion will undergo the same type of decaying and emission as the case for $\sigma-$ laser. The only difference is that it can only excite $m_s = -1/2$ ground state but not $m_s = +1/2$ ground state.

of the ion interacting with $\sigma+$ and $\sigma-$ lasers. $\sigma-$ laser can only excite the ion to $^2P_{1/2}m_s = -1/2$ state when it is in $m_s = +1/2$ ground state. From $m_s = -1/2$ excited state, atom spontaneously emits a σ photon with probability of $2/3$ and returns back to the $m_s = +1/2$ state or a π photon with probability of $1/3$ and falls into the $m_s = -1/2$ ground state. In this state the ion does not interact with this laser any more. On average the ion emits two σ photons and then emits a terminal π photon and goes to the dark state.

From $m_s = -1/2$ ground state, $\sigma+$ laser can excite the atom to $^2P_{1/2}m_s = +1/2$ state. Again ion may emit a π or σ photon and in the case of emitting a π photon, it falls to the dark state for this laser.

The emitted π and σ photons are not scattered homogeneously. The emission pattern for the π and σ Polarizations is shown in Fig. 5.2. For the π transition, the radiation is maximum perpendicular to the magnetic field and zero along the magnetic field. For the σ transition most of the radiation is along the magnetic field and it is minimum perpendicular to the magnetic field.

Radiation pattern for a π transition is similar to the radiation from an oscillating electric dipole along the z direction:

$$\vec{E}_\pi(r, \theta, t) = \frac{\mu_0 p_0 \omega^2}{4\pi r} \sin(\theta) \cos(\omega t - \omega r/c) \hat{\theta} \quad (5.2)$$

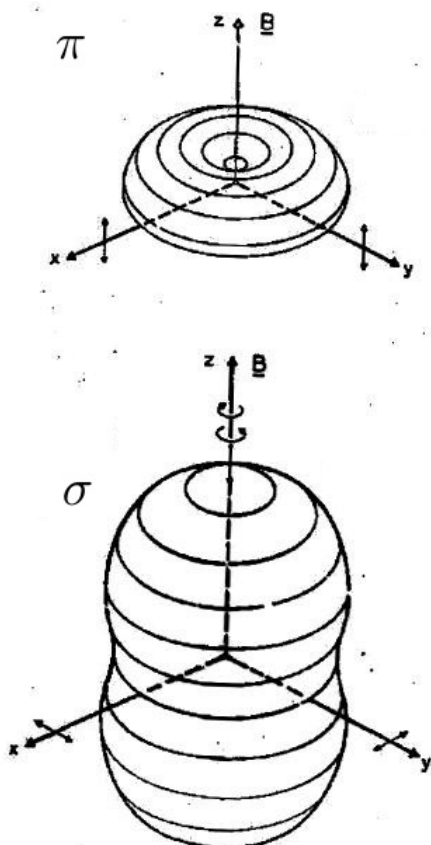


Figure 5.2: Emission Pattern of the π and σ polarized photons. top: For the π photons the maximum probability of emission is perpendicular to the magnetic field. No π photon is emitted along the magnetic field direction. bottom: The probability of emission of σ photons along the magnetic field is twice the probability perpendicular to the magnetic field. Both polarizations are linear, if they are emitted perpendicular to the magnetic field. In this direction polarization of the π photons is along the magnetic field and polarization of the σ photons is perpendicular to the magnetic field. (Image courtesy: <http://astro1.panet.utoledo.edu>)

which has the amplitude of:

$$\vec{E}_\pi(r, \theta) = \frac{\mu_0 p_0 \omega^2}{4\pi r} \sin(\theta) \hat{\theta} \quad (5.3)$$

For a σ transition, the emission pattern is similar to a rotating dipole around the z axis:

$$\begin{aligned} \vec{E}_\sigma(r, \theta, t) &= \frac{\mu_0 p_0 \omega^2}{4\pi r} \cos(\theta) \left(\cos(\omega t - \omega r/c) \cos(\phi) + \sin(\omega t - \omega r/c) \sin(\phi) \right) \cos(\omega t - \omega r/c) \hat{\theta} \\ &\pm \frac{\mu_0 p_0 \omega^2}{4\pi r} \left(\cos(\omega t - \omega r/c) \sin(\phi) - \sin(\omega t - \omega r/c) \cos(\phi) \right) \cos(\omega t - \omega r/c) \hat{\phi} \end{aligned} \quad (5.4)$$

with amplitude of:

$$\vec{E}_\sigma(r, \theta) = \frac{\mu_0 p_0 \omega^2}{4\pi r} \left(\cos(\theta) \hat{\theta} \pm i \hat{\phi} \right) \quad (5.5)$$

For these emissions, the polarization quantum state functions are:

$$|\pi\rangle = \sin(\theta) |\hat{\theta}\rangle \quad (5.6)$$

$$|\sigma_\pm\rangle = \frac{e^{\pm i\phi}}{\sqrt{2}} \left(\cos(\theta) |\hat{\theta}\rangle \pm i |\hat{\phi}\rangle \right) \quad (5.7)$$

Where θ is the polar angle with respect to \hat{z} and ϕ is the azimuthal angle. $\hat{\theta}$ and $\hat{\phi}$ are the unit vectors in the spherical coordinate.

This shows that for π polarized light, the probability of emission is proportional to $\sin^2(\theta)$ which means that it is zero along the z direction and maximum perpendicular to the z direction. The polarization is always linear and along the $\hat{\theta}$.

For the σ transition, the probability of emission along a direction with the polar angle of θ is proportional to $1 + \cos^2(\theta)$. This means that the probability of emission along the z axis is double the probability of emission perpendicular to the z axis. Along the z direction with $\theta = 0$, the wavefunction takes the form $|\hat{\theta}\rangle \pm i |\hat{\phi}\rangle$ which is a circularly polarized light. With a finite θ the polarization becomes elliptical and at $\theta = \pi/2$ it becomes linear and perpendicular to the polarization of the π polarized light.

The absorption pattern is exactly the same as emission pattern. The higher the probability of emission in a particular direction, the higher is the probability of absorbing a photon along that direction. Therefore to maximize the absorption of σ polarized photons one must set the direction of the laser to the direction of the magnetic field. For the lasers with linear polarization, the best direction is to have it perpendicular to the magnetic field

and set the direction of the polarization parallel to the magnetic field.

5.2 Automatic Control Of The Lasers and The Detectors Using Labview FPGA

To perform the single photon generation protocol, one important requirement is the ability to turn the lasers and the detectors on and off very accurately in time. To perform this, I developed a program in LabView(TM) to control the digital and analogue outputs of the LabView(TM) FPGA RIO0 PCI-7833R card. This program can control the on/off time of the outputs with the accuracy of 25 ns . This accuracy is limited by the device clock cycle and not the program's algorithm. A screenshot of the program's user interface is shown in figure 5.3. In this program it is possible to define a sequence of actions, simultaneously on all outputs, then repeat it by the number given in the "Number of Repetitions" input. An input array, "Element Clock Cycles", enables the user to divide each single repetition to a number of elements. User can determine the length of each element individually and during each element, turn each digital input on or off or change the value of an analogue output. The shortest length for each element is one clock cycle of the FPGA card. The vertical inputs given on the left side of the digital and analogue inputs can be used to determine the default status of the outputs, when sequence is not running. The rows "DIO 14" and "DIO 15" show the number of detected photons from two photon detectors. These outputs show live accumulation of counts separately for each element, during the repetition of the sequence. When the sequence is not running the counts/s for each detector can be read from "DIO 14 Idle Counts(/s)" and "DIO 15 Idle Counts(/s)".

The underlying algorithm of the program is composed two main block diagrams(in LabVIEW(TM) programming, a graphical unit of codes is called block diagram). One of them consists of the codes that are executed on the host computer and is called `Host_main`. The other block diagram is the code that is executed on the FPGA chip and is called `FPGA_main`. The communication between the two is through a set of commands that are called interrupts. `FPGA_main` waits for a command and the corresponding data and executes the command on the FPGA card and after finishing the task waits for the next command.

`Host_main` has two principle modes of operation: the *Idle* mode and the *Sequence* mode. *Sequence* mode is executed when requested by the user. *Idle* mode is the default mode and is running when the *Sequence* mode is not running. In the *Idle* mode, `Host_main`, alternatively, sends *Counting* and *Set to Default* commands to the `FPGA_main`. For the *Counting* mode, `Host_main` provides `FPGA_main` with a time window for detection and `FPGA_main` accumulates the counts on the detectors' inputs for the period of the time



Figure 5.3: FPGA control program's user interface screenshot. In the default mode, program shows counts/s for each detector with "DIO 14 Idle Counts(/s)" and "DIO 14 Idle Counts(/s)" outputs and applies the default values to the digital and analogue outputs. These default values are entered using vertical array inputs on the left side of the interface. User can also choose to repeat a sequence of events and change the values of outputs during time. Time length of each element is entered in "Element Clock Cycles" field and the corresponding value of digital and analogue outputs can be entered under each element cell in the inputs provided for each output port. After pressing "Start Sequence" program repeats the commands for the number of times given in "Number of Repetitions". During the execution of the sequence, DIO14 and DIO15 outputs display the live accumulation of number of detections for each time element.

window and returns a counts/s value for each detector. For the *Set to Default* command, `Host_main` reads the default values for each digital and analogue output from the user interface and creates an array of values and pass it to `FPGA_main`. `FPGA_main` sets the outputs to the requested values and waits for the next command.

In the *sequence* mode `Host_main` provides `FPGA_main` with an array of values for each output, array of time elements and number of repetitions. `FPGA_main` runs a *single-cycle timed loop* that guarantees the execution of all calculations in one clock cycle(which is 25 ns). In each cycle it calculates the value of each output using the arrays provided and applies that to the outputs. During the execution of the sequence, it also saves the detection times for each detector. This data is saved in a FIFO in FPGA chip and is transferred to `Host_main` after the end of the sequence. `FPGA_main` also accumulates the number of detections for each time element in the sequence. This data is streamed to `Host_main` to be displayed live on the user interface.

To use FPGA outputs, to turn the lasers on and off, we used AOMs. Each laser goes through an AOM that is controlled by a homebuilt AOM driver. These drivers accept TTL inputs. For TTL 1 they turn the diffraction on and for TTL 0 they turn the diffraction off. Turning the diffraction off, moves the direction of the laser beam and misaligns the coupling to the fibre that goes to the trap and effectively turns the laser off at the trap.

In this protocol we need to turn the detection off for the period of the cooling and the preparation and keep it on only for the period of the detection(see section 5.3). We realize this by using Mini-Circuits(TM) ZYSW-2-50DR RF switches that received an input from FPGA and cut or connected the connection between PMT's and the time-tagger device.

5.3 Single Photon Generation Protocol

The single photon generation protocol is depicted and explained in Fig. 5.4. The sequence shown in this figure is repeated to generate single photons. For this protocol, we use two 370 nm lasers with $\sigma+$ and $\sigma-$ polarizations. Interaction of these lasers with the ion is explained in section 5.1. Each repetition starts with a cooling cycle. When any of the lasers are on, after a few cycles, the ion goes to a dark state for that laser. Therefore we need to keep both lasers on to have a continuous excitation and emission process to cool the ion. The next step is the preparation step. To prepare the ion, we only keep the $\sigma-$ laser on. In this step the ion may emit a few σ photons and return back to $m_s = +1/2$ ground state but finally it emits a π photon and falls into the $m_s = -1/2$ ground state. This is a dark state for this laser.

To separate the preparation and generation steps we turn our detection on 750 ns and the generation laser 1000 ns after the preparation. For the single photon generation step we use the $\sigma+$ laser. When the ion is exited by this laser, it goes to ${}^2P_{1/2}m_s = +1/2$ state. From here the ion spontaneously emits a photon and returns back to the ground

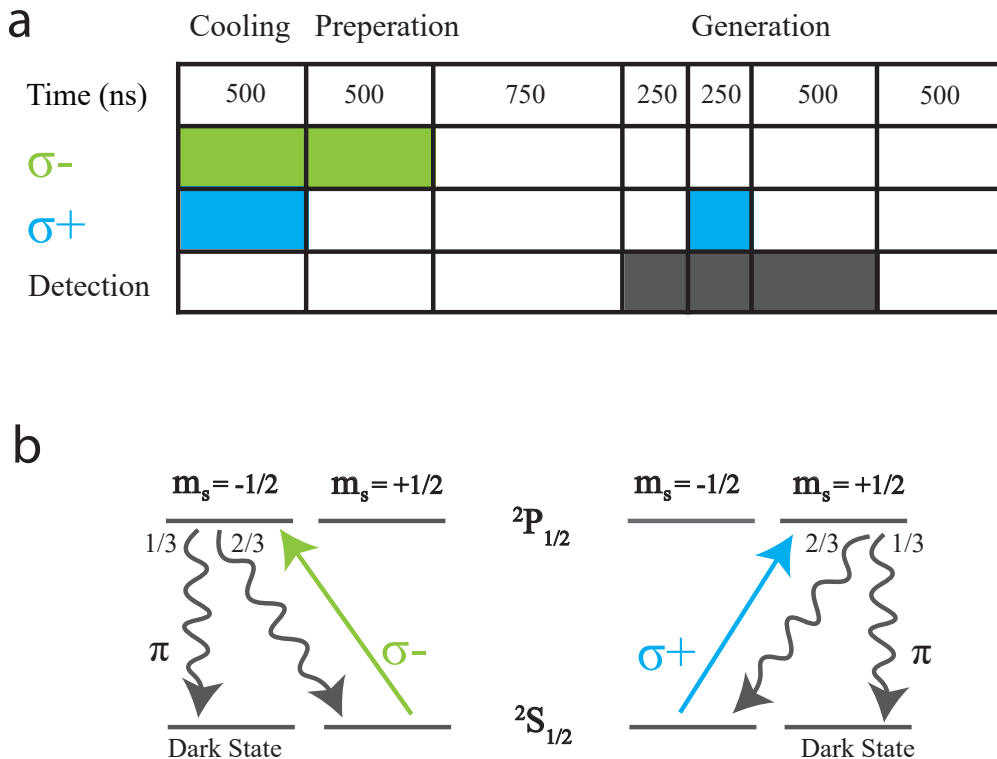


Figure 5.4: a. Single photon generation protocol. 370 nm $\sigma-$ and $\sigma+$ lasers are on for 500 ns to generate a continuous excitation cycle to cool the ion. Then only $\sigma-$ laser remains on for another 500 ns to prepare the ion in the $m_s = -1/2$ ground state. For 1000 ns both lasers remain off to reliably separate the preparation process from generation process. Detection is turned on 750 ns after the preparation and remains on for 1000 ns. 1000 ns after preparation, $\sigma+$ generation laser is turned on and remains on for 250 ns. This generates two σ photons on average and finally the ion emits a π photon and goes to the dark state. By filtering the σ photons using a polariser, Only one photon is collected during the generation step. b. Relevant transitions for single photon generation protocol.(for details on transitions see section 5.1 and Fig. 5.2)

state. There is a $2/3$ chance for the ion to return to $m_s = -1/2$ and emit a σ photon. If this happens the $\sigma+$ laser excites the ion again to the same excited state. There is also a $1/3$ chance for the ion to emit a π photon and drop to $m_s = +1/2$ ground state. This is a dark state for the $\sigma+$ laser and no photon is absorbed in this state. On average ion emits 2σ photons and then goes to the dark state by emitting a π photon. To generate only one photons in each cycle, we need to filter σ photons and only collect the π photons.

As it is explained in section 5.1, all photons that are emitted perpendicular to the magnetic field direction have linear polarizations. For a π photon this polarization is along the magnetic field and for a σ photon it is perpendicular to the magnetic field. This means that if we set our imaging axis perpendicular to the magnetic field (on the equatorial circle), we can use a polariser to filter the σ photons and collect only π photons.

Going away from the equatorial circle, photons from σ transition start to have a polarization component along $\hat{\theta}$ (see section 5.1) and may pass the polariser with probability of $\cos^2(\theta)$; This is called polarization blurring. For the optics with high numerical aperture this effect can be significant.

To estimate the collection efficiency for σ and π photons and polarization blurring, Erik Streed has developed a program in Mathematica(TM). In our system, the mirror dimensions are $80 \times 127\mu m$ and the ion height is $59.6\mu m$. The direction of the magnetic field (and the laser) is parallel to the surface of the mirror and creates a 45° angle with the mirror sides. In this configuration mirror's NA is 0.55×0.73 which is equivalent to circular NA of 0.68. The mirror covers 12.9% of the total solid angle. This mirror collects 17.4% of the π light and 11.3% of the σ light (Fig. 5.5).

In the process of characterizing the mirror collection efficiency, we reduced NA to alleviate the polarization blurring. To do this we used an iris in the cooling mode(both $\sigma+$ and $\sigma-$ lasers on) to reduce the counts to 50%. With this configuration the program shows that 0.069% of the σ photons pass the polariser; therefore we expect a second order correlation $g^{(2)}$ of equal to or greater than 0.069(See section 5.6).

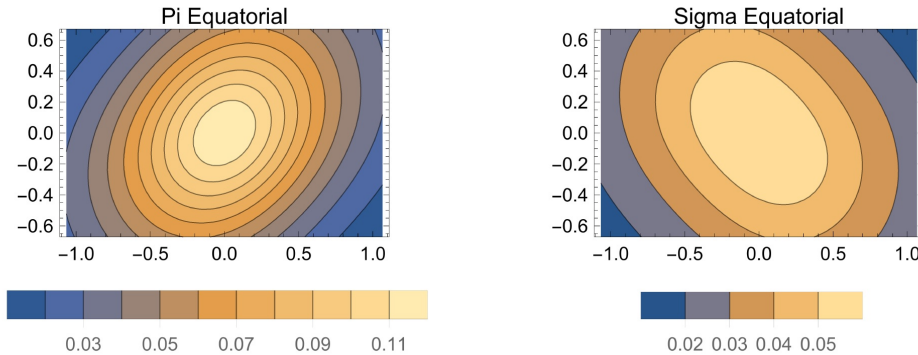


Figure 5.5: Contour plot of the emission pattern on the mirror for π photons(left) and σ photons(right). (Plot courtesy of Erik Streed)

5.4 Experimental Setup

The experimental preparation process can be divided into three main categories of setting up electronics, optics for the lasers and optics for the photon collection.

A schematic of electronic devices configuration is shown in Fig. 5.6. The FPGA card is controlled by the program explained in section 5.2. One of the digital outputs of this card goes to TTL input of the AOM driver for the $\sigma+$ laser. This driver turns the AOM on for TTL pulse of 1 and turns it off for TTL pulse of 0. Another digital output is connected to the TTL inputs of the AOM driver for the $\sigma-$ laser and controls that in the same manner. The third digital output of the FPGA card is split and goes to two RF switches that can connect or disconnect the connection between PMTs and the time-tagger box. This box is used to analyse the statistical behaviour of the time of arrival of the photons.

The lasers that we need for this protocol are two 370 nm lasers with circular polarizations of $\sigma+$ and $\sigma-$. The lasers have $7 \mu\text{w}$ of power and their spot size at focus is $80 \mu\text{m}$. In the normal operation mode we already have two 370 nm lasers that go to the trap but their frequency detuning is different. One of them has a fixed 70 MHz detuning and is used to facilitate the cooling process of the hot ion at the time of trapping. For this protocol we need both lasers to have 10 MHz detuning from the resonant frequency therefore we need to replace this laser. Having 10 MHz detuning instead of 70 MHz detuning, increases the chance of the absorption of the photons and decreases the time that is needed for the preparation or generation step. We combine the 370 nm lasers with a polarizing beam splitter (see section 3.10) therefore their polarizations are linear and perpendicular to each other. For this experiment we add a quarter waveplate to the set-up that turns the polarization of one of the lasers into $\sigma+$ and the other into $\sigma-$ polarization.

For this experiment the laser polarization purity is very important. If the polarizations

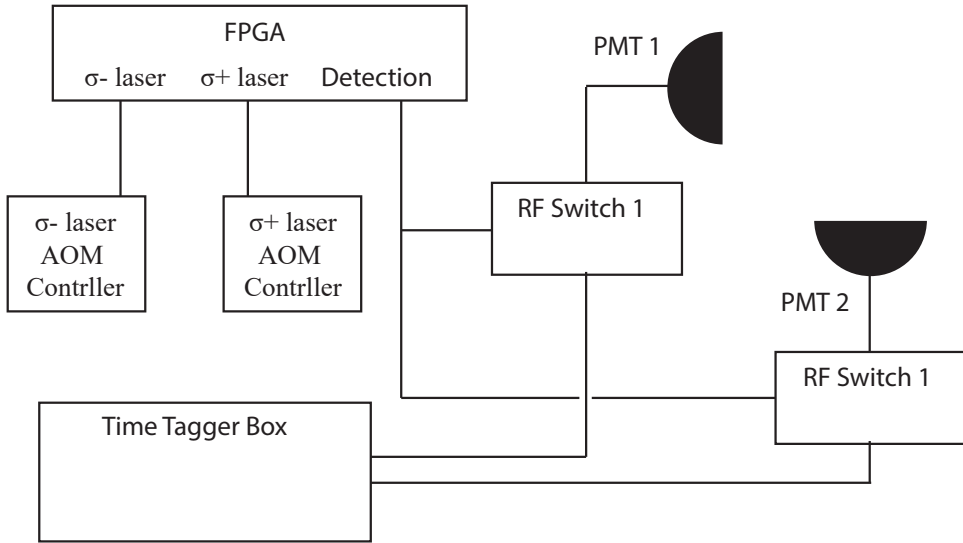


Figure 5.6: Schematics of the electronic setup for the single photon generation protocol. FPGA card controls the lasers and detection. To turn the lasers on and off, we use FPGA digital outputs to send a TTL signal to the AOM drivers. To turn the detection on and off, we use RF switches between PMTs and the time-tagger box.

of the lasers deviate from the circular polarization, they can excite the ion when it is in the dark state and this may lead to the generation of two photons instead of one for some generation cycles. To prepare a pure polarization we used a *Casix(TM)PN : WPZ1312 – $\lambda/4$ – 370* zero order quarter waveplate and replaced the Thorlabs(TM) PBS102 polarizing beam splitter in the beam combiner with a Thorlabs(TM) GLB10-UV - Glan-Laser alpha-BBO polarizing beam splitter that has the polarization purity of 100,000:1 for the through port.

The non-trivial angle for the side port of this polarizing beam splitter makes the overlapping process hard. The input laser to this side port generate two modes and part of the power is wasted in the second mode. The polarization purity of the side port is lower than the through port therefore we use it for less critical $\sigma-$ laser that is used in the preparation step.

During this experiment 935 nm repumper laser is always on and is heavily saturating its transition. To make sure that the absorption of the σ photons is maximized, we set the direction of the magnetic field parallel to the laser propagation axis. Absorption is maximized in the direction that emission is maximized. Fig. 5.2 and Equ. 5.5 shows that the emission is maximum along the direction of the magnetic field.

To set the direction of magnetic field along the laser, which is parallel to the chip

surface and creates a 45° angle with RF electrodes, we used three coils for vertical, 45° and -45° directions. To have the magnetic field exactly along the laser we measured earth's magnetic field and roughly set the coils' currents to cancel the earth's magnetic field. Then by scanning near this point we found Henley resonance to make sure that magnetic field is zero. Henley resonance is the sudden drop of the ion fluorescence when magnetic field is set to zero, where there is no preferred quantization axis. From this point we swapped the current direction in the 45° coil to have a magnetic field only along this direction.

To collect and analyse the generated photons we used the optical set-up shown in Fig. 5.7. A set of five lenses shown in this figure is used to transfer, collimate and resize the beam. The collimated beam is sent to a polariser, shown in Fig. 5.7b, to filter σ photons and leave only π photons. π photons are sent to the two photo multiplier tubes(PMTs) using a non-polarizing beam splitter(NPBS). An IDQ TDC id800 time-tagger device is used to analyse the statistics of the time delays between the detections(see section 5.6).

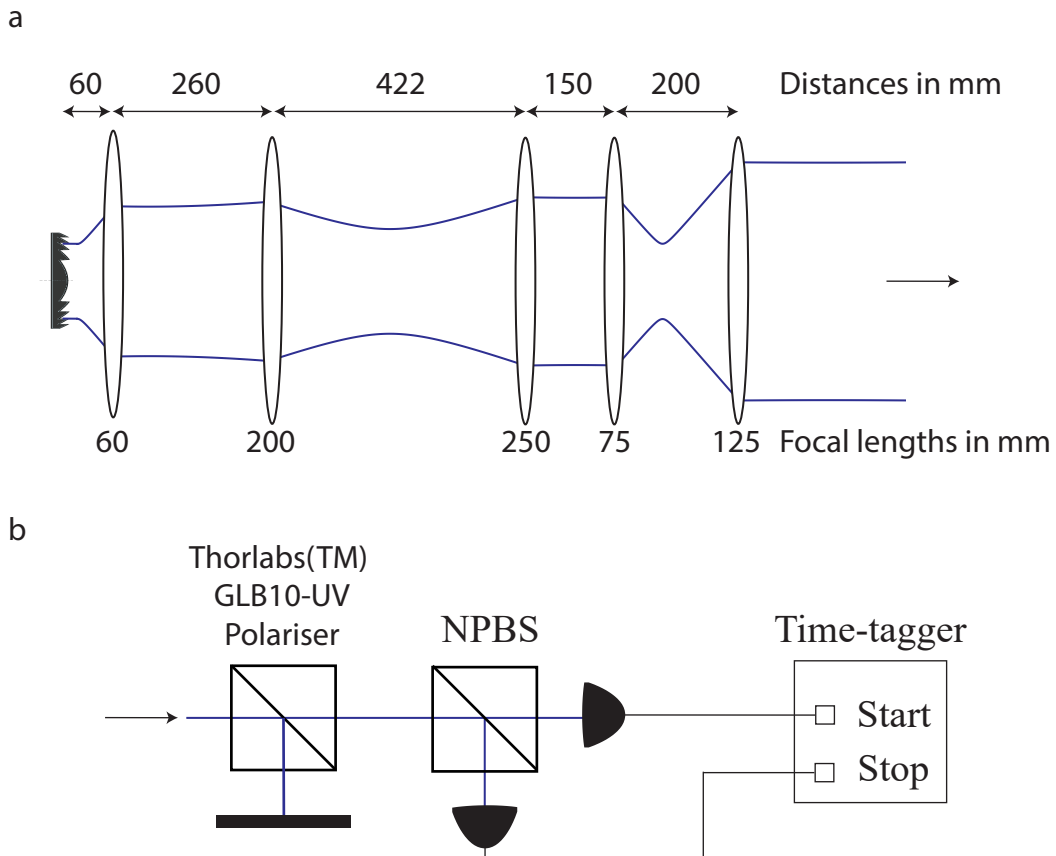


Figure 5.7: Optical set-up for the collection of the single photons. a. The optical set-up used to transfer, collimate and resize the beam to send it to the single photon analyser set-up. The first two lenses are used in the bulk imaging set-up (4.1). We leave this set-up untouched and use a $f=250\text{ mm}$ lens to collimate the light. The next two lenses($f=75\text{ mm}$ and $f=125\text{ mm}$) act as a telescope to resize the beam. This last telescope is not necessary for this experiment and is used for mode matching for the fibre coupling experiment. b. Single photon analyser set-up. This set-up uses a polariser to filter the σ photons and let through the π photons. Using a non-polarising 50-50 beam splitter, the π photons are split and sent to the two photo multiplier tubes(PMTs). A time-tagger device analyses the statistical regime of photon emission(see section 5.6)

5.5 Characterization Of The Time Scales and Delays

To synchronize generation and detection processes, It is important to know the delay between executing a command to turn a laser on and detecting it at the detectors. To measure this delay we used continuous fluorescence of the ion and turned the laser on for 250 ns at the start of the sequence and kept it off for $1\text{ }\mu\text{s}$ after that. We divided the off time of the laser to 50 ns elements and saved the counts for each element for 2 seconds of accumulation. The results showed that we start detecting fluorescence 500ns after sending the command to turn the laser on.

It is also important to know the time scale of getting a single photon after turning on the generation laser. In the generation step, on average, it takes three absorption and emission processes to emit a final π photon. These absorptions are probabilistic and the chance of absorption increases exponentially with time. To measure the exponential time constant for this process we ran the single photon generation sequence shown in figure 5.4 and divided the detection period to the elements of $1.25\mu\text{s}$. Then we accumulated the counts for 1 minute and fitted an exponential function to the data. The exponential time scale of the probability of generating a single photon measured to be $0.21\text{ }\mu\text{s}$. A graph of data acquired and the exponential fit is shown in figure 5.8. This time scale shows that for the period of 250 ns , that we use for the generation step, there is a 69% chance to generate a photon.

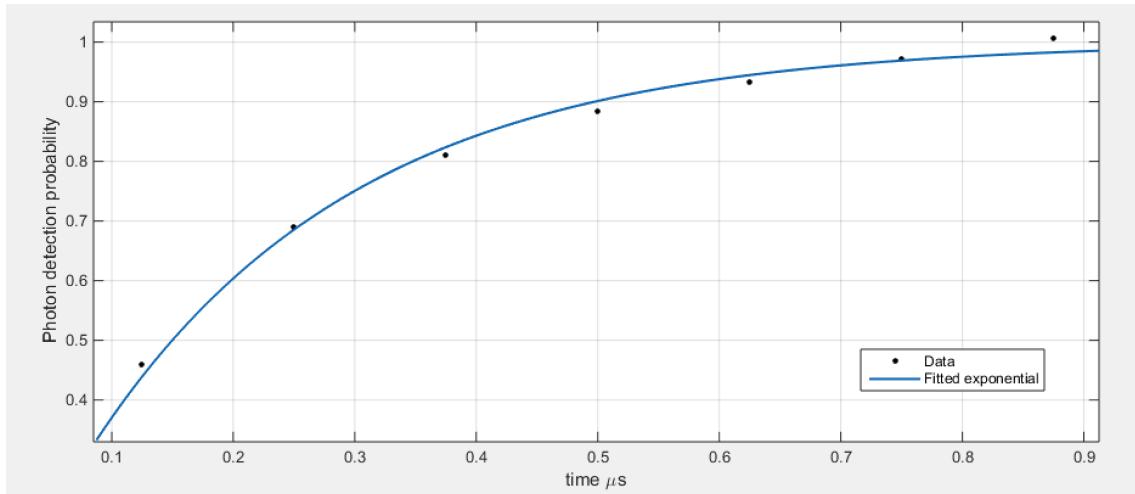


Figure 5.8: Number of photons generated in each step after time t after turning on the generation laser. The data is taken by repeating the sequence for one minute and then normalise the data to one at infinity. the blue fitted graph shows that the exponential time scale of the generation is $0.21\mu\text{s}$. This is equivalent to the average generation of 0.69 photons in each step.

5.6 Measuring Single Photons 2nd Order Correlation $g^{(2)}$

The second-order correlation function $g^{(2)}(\tau)$ quantifies the intensity fluctuations of a light source. $g^{(2)}(\tau)$ is often called the degree of second-order coherence, in the classical optics books. The definition in terms of intensity is[76]:

$$g^{(2)}(\tau) = \frac{\langle I(t)I(t+\tau) \rangle}{\langle I(t) \rangle^2} \quad (5.8)$$

In an experiment, the data that we have maybe the arrival time of the photons. In this case we use the formula below:

$$g^{(2)}(\tau) = \frac{\langle n(t)n(t+\tau) \rangle}{\langle n(t) \rangle^2} \quad (5.9)$$

$g^{(2)}(\tau)$ answers this question: If we detect a photon at any time t , what is the probability of getting another one after the time delay of τ . If $g^{(2)}(\tau)$ is smaller than one, the probability of getting the second photon after the time τ is smaller than the average probability and this means that photons are anti-bunched. This is a behaviour seen in a single photon regime. For $g^{(2)}(\tau)$ higher than one the chance is higher than the average and the photons are bunched. Thermal lights usually show bunched statistical behaviour. If $g^{(2)}(\tau)$ is one, the chance of getting a photon, after time τ , is equal to average photon rate and this means that it is statistically independent of the arrival of the previous photon. Lasers show this type of statistical behaviour. $g^{(2)}(\tau)$ can be different for different time delays τ and this means that we can have bunching for some time scales and anti-bunching for the others.

In the case of generating single photons, one important number is $g^{(2)}(0)$. The closer to zero this number is the more efficient is our single photon generation. $g^{(2)}(0) = 0.5$ is called single photon generation threshold. In the case of analysing experimental photon counting statistics with formula 5.9, calculating $g^{(2)}(0)$ leads to a problem. In any physical situations, photons do not arrive exactly at the same time and this means that $g^{(2)}(0)$ is always zero. To avoid this problem and get a meaningful number we need to choose a time window and if the two photons arrive within that time window, consider the event a coincidence for delay of zero. Practically this time window must be equal or greater than the time resolution of the detector or if we are doing a process on the single photons, it must be equal or greater than the time it takes for our devices to change its settings for the next photon. In our case because the generation is deterministic and the generation cycle is $3.75\mu s$ we count every arrival within the delays of $\pm 1.875\mu s$ a coincidence for the time delay of zero, every arrival within the time window of $3.75 \pm 1.875\mu s$ a coincidence for $\tau = 3.75\mu s$ and so on.

Using the data that was collected by time-tagger box in the experimental set-up, we

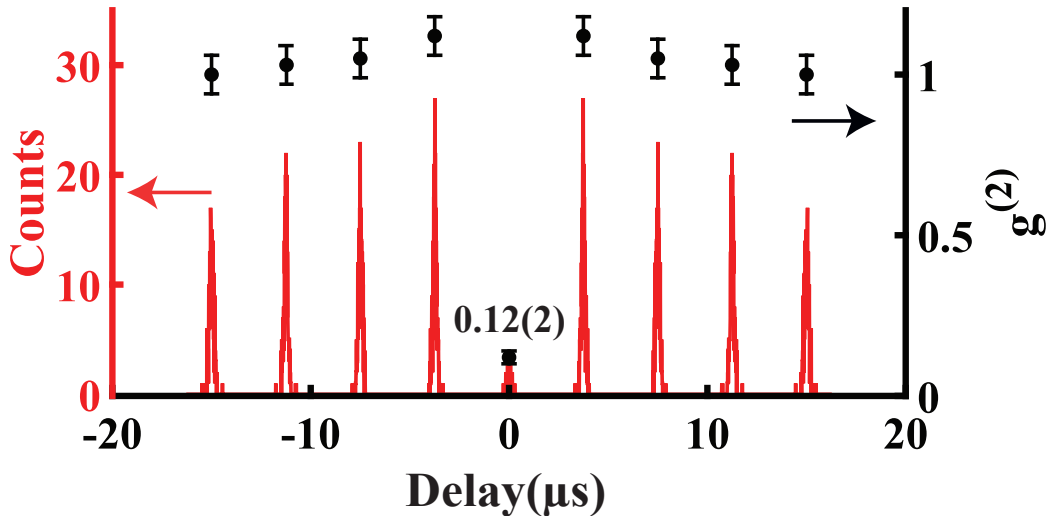


Figure 5.9: Second order correlation $g^{(2)}$ for the single photon generation protocol. The raw $G^{(2)}$ counts are shown on the left red axis. To calculate $g^{(2)}(0)$ we bunched all the counts in each peak and using an exponential decaying fit estimated $G^{(2)}(\infty)$. Using this value we measured $g^{(2)}(0)$ of $0.12(2)$.

plotted the graph shown in figure 5.9. To normalize the raw coincidence counts $G^{(2)}(0)$, we used the fact that $g^{(2)}(\infty)$ is 1. This is because for long enough time there will be no correlation between arrival time of photons. To estimate the $G^{(2)}(\infty)$ we used a decaying exponential fit for the $G^{(2)}(\tau)$ and estimated the value at infinity. Using this technique we showed that $g^{(2)}(0)$ for our experiment is $0.12(2)$ which is well below the single photon threshold of 0.5. Black dots on the graph shows the $g^{(2)}$ for each peak. Except for the middle peak the $g^{(2)}$ is greater than one for all the other peaks. This means that we have slight bunching behaviour for the time delays equal to or greater than one generation cycle. This shows that if we get a photon in one cycle, the chance of getting another photon in the next cycle is higher than average. This is because of the slight power fluctuation of the laser. When power is higher, It is more likely to get photons in consecutive cycles and when the power is lower it is more likely to get nothing in a few consecutive cycles.

CHAPTER 6

Efficient Photon Collection

This chapter covers the demonstration of efficient collection of ion fluorescence using diffractive mirrors which was the main goal of this project. Photon collection from an ion is an important part of many applications in quantum computing and quantum communication with trapped ions. For example the most common method of ion qubit state readout -which is called electron shelving technique- is accomplished by shining a specific laser on the ion and detecting the ion fluorescence. For one qubit state ion starts fluorescing strongly but for the other state it stays dark. The time that one needs to wait to discriminate between these two states is directly proportional to the fraction of the light that an optical system can collect from the ion.

Another application -in which the ion light collection efficiency plays a crucial role- is remote entanglement. In this technique short pulses are used to excite the ions and generate single photons. The single photons from two ions then collected and interfered to post selectively entangle ions. The probability of entangling two ions is squarely proportional to the light collection efficiency. In these type of experiments ion light is coupled into a single mode fibre and transferred to the interference setup. This is because without coupling to a fibre transferring the photons and interfering them from two remote locations is practically challenging, if not impossible. This means that not only the free space light collection efficiency but also single mode fibre coupling efficiency is important in this application.

Single mode fibre coupling efficiency is also important in quantum communication applications where ion plays the role of a single photon source or a memory. Both the generation rate of a single photon source or the success rate of the storing the state of a photon qubit in an ion qubit is proportional to the single mode fibre coupling efficiency.

This chapter reports the demonstration of collection efficiency of integrated diffractive mirror in both regimes of free space collection and coherent collection into a single mode fibre.

6.1 Ion Fluorescence Collection

Efficient collection of the photons from an ion is a challenging task. The first requirement for an efficient optical system is to cover a large fraction of solid angle around the ion which is equivalent of having a high numerical aperture(NA). This means that the size of the entrance pupil must be comparable or bigger than the distance from the ion to this pupil. To fulfil this requirement we designed a system with reflective optics with the size of $127 \times 80 \mu\text{m}$ which have different focal lengths between 56.6 to $62.6 \mu\text{m}$ (see section 2.3). These mirrors are made by integrating diffraction rings into the ground electrode of GTRI Microwave I chip traps(see section 2.2). The diffraction pattern simulates the phase shift of a curved mirror and collimates the light from a point source that is located at the focal point of the mirror. The maximum depth of the features is only 180 nm and has no effect on the electrical role of the electrode. The design is wavelength dependent and is designed for 370 nm which is the wavelength of the main cooling transition of Yb^+ ions. The integrated design of the mirrors eliminates the need for alignment and the maximum mis-alignment that we may experience is one μm which is the accuracy of the alignment of the e-beam lithography process that is used to fabricate the diffractive features(see section 2.3.3. This is within the two μm tolerance of the optical design(see section 2.3.2).

To collect the photons efficiently, the ion must be placed at the focus of the mirror. In our design we have four collimators on each chip that have different focal lengths. In this experiment we used γ design that have collimators with focal lengths of 58.6 , 60.6 , 62.6 and $59.6 \mu\text{m}$. 58.6 is the normal ion height in the Microwave I chip trap therefore it is the most preferable option but because of the problems explained in section 4.4 we use the 4th collimator with focal length of $59.6 \mu\text{m}$.

when the ion is placed at the focal point, the mirror collects and collimates the portion of the light that is within the field of view(FOV). Other optics maybe used to transfer or resize the beam but in principle it is possible to directly send this light to a detector(For more details about the diffractive mirrors refer to section 2.3).

To demonstrate the collection efficiency of the mirror, as it is explained in chapter 5, instead of using the continuous fluorescence of the ion and calculating the fluorescence rate using equation 5.1, we used the single photon protocol that we developed. In this method the number of generated photons is known from the repetition rate of the protocol and comparing that with the detected photons give us the collection efficiency of the mirrors.

6.1.1 Experimental Setup

The first step in preparing an experimental set-up for the demonstration of the collection efficiency is to trap an ion and shuttle it to the 4th collimator. The center of this collimator is located at $871.1 \mu\text{m}$ away from the loading point. To laterally position the ion at the focus we use `Ex_Comp_Weight=0.2` which is equivalent to applying an electric field of 200

V/m to the ion.(see section 4.4). This fine lateral adjustment does not have any effect on the collection efficiency but it has an effect on the mode quality of the beam that improves the single mode coupling efficiency. Based on the characterization in section 4.4, we set the E_y to 0.5 to set the ion height to $59.6 \mu m$. This is equivalent to applying an upward electric field of $500V/m$ to the ion.

Once the ion is at the focus, the mirror collimates the collected light. We use the optical set-up shown in Fig. 6.1 to collect the light. To set-up the optical system, the behaviour of the beam was simulated with the ABCD method explained in section 4.3.1. The output of the simulation is shown in Fig. 4.10. In designing this optical system, we left the bulk optics imaging lenses untouched(see section 4.1). The reason is that we need to switch to this mode every time that we need to trap a new ion or shuttle the ion. These two lenses create a focus $172 mm$ away from the second lens and we need to use $f = 250mm$ lens $422 mm$ after the second lens to collimate the light. The extra telescope consists of $f = 75mm$ and $f = 125mm$ lenses is only necessary for the mode matching of the single mode fibre coupling experiment6.2.

To generate the single photons we used the protocol shown in Fig. 5.4. A compatible optical set-up needs a polariser to filter unwanted σ photons generated by the protocol. This protocol also needs an iris to reduce the counts to 50%. This is to reduce the effect of polarization blurring of the σ photons for the high NA optics.

To prepare the lasers for this experiment we need to have two near resonance lasers($10 MHz$ detuned) with circular polarization of $\sigma+$ and $\sigma-$ (see section 5.4) therefore we need to add a quarter waveplate to the beam combiner set-up, to transform the polarizations of the lasers from linear into circular.

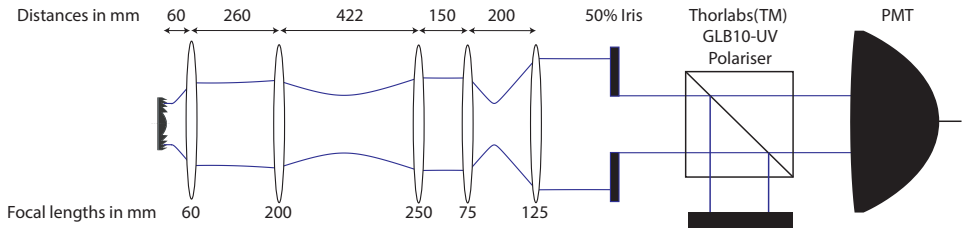


Figure 6.1: The optical set-up for the demonstration of the collection efficiency of the 4th collimator on the γ chip. The focal length of this collimator is $59.6 \mu m$. This collimator collect and collimates the ion beam. because of the short Rayleigh range of 8.7 and $5.1 mm$ (see section 4.3), this beam becomes divergent before exiting the vacuum chamber. The first 2 lenses are the the lenses that are used for external bulk optics imaging mode(see section 4.1). This part focuses the beam $172 mm$ after the second lens. A $f = 250 mm$ lens is used to collimate the light again. A final telescope consists of a $f = 75mm$ and $f = 125mm$ resizes the beam and sends that to a PMT. In principle this complex optical set-up is not necessary for this experiment. The only reason that we used this set-up was that we wanted to use the same optical system for this experiment and the single mode coupling experiment. The iris is used to decrease the counts to 50% and reduce the polarization bluring effect. The polariser is used to filter unwanted σ photons and only let through π photons. This is necessary for the single photon generation protocol(see section 5.3).

6.1.2 Theoretical Estimation Of Collection Efficiency

The collection efficiency of the diffractive mirrors depends on three parameters: reflectivity of the material, diffraction efficiency of the design and solid angle coverage.

The electrodes and hence the integrated mirrors are made of aluminium. Reflectivity of the aluminium over ultra violet range is 92%. The diffraction efficiency of the design depends on the number of levels used in diffraction profile approximation. The γ design that we use is a hybrid design. For the larger inner features($> 200nm$), the design uses four level approximation. For this part, each step is $45 nm$ heigh. For the features smaller than $200 nm$ two level approximation is used and each level is $90 nm$ high. Simulation with Gsolver and GD-calc programs predict the diffraction efficiency of about 50% for this design. This number includes the reflectivity of the aluminium(see section 2.3.2).

If ion was a homogeneous emitter, the percentage of the photons that reach the mirror was the same as the geometrical solid angle coverage. For the 4th collimator the focal length is $59.6 \mu m$ and the mirror is $80 \mu m$ wide and $127 \mu m$ long. Using solid angle coverage formula for a rectangle we calculate 12.9% coverage:

$$\frac{\Omega}{4\pi} = \frac{1}{\pi} \arcsin \frac{ab}{\sqrt{(a^2+h^2)(b^2+h^2)}} = 0.129 \quad (6.1)$$

where $a = 40\mu m$ is half the rectangle's width, $b = 63.5\mu m$ is half the rectangle's length and $h = 59.6\mu m$ is the height of the ion.

From section 5.1 we know that the emission pattern of the ions is not homogeneous and depends on the polarization. Here we collect π photons and our optical axis is perpendicular to the magnetic field. Fig. 5.2 shows that the probability of emission of the π photons, in this direction, is higher than the average. To calculate the probability of collecting of the π photons, Erik Streed used Mathematica(TM) to numerically integrate the emission probability, equation 5.6, over the area of the mirror. This calculation predicts 17.4% collection efficiency for the π photons. Together with 50% diffraction efficiency we expect collection efficiency of 8.7%.

6.1.3 Measuring Collection Efficiency:

To measure the collection efficiency of the mirrors, we generate single photons according to the protocol explained in Fig. 5.4. Performing this protocol generates average of 0.69 photons per cycle(see section 5.5) and repeating the protocol continuously is equivalent to having 2.66×10^5 cycle per second. This results in generation of 1.84×10^5 photons per second. These photons go through the optics shown in Fig. 6.1 and reaches the detector. Knowing the number of generated photons, NGP , total transmission rate of the optics, TR , PMT quantum efficiency, $PMTQE$, and the number of detected photons, NDP , one can calculate the collection efficiency of the mirror, CE :

$$CE = \frac{NDP}{NGP \times TR \times PMTQE} \quad (6.2)$$

We measured $NDP = 770(27)$ for the number of detected photons. The quantum efficiency of the PMT, $PMTQE$, is 0.19. A list of optical transmissions for the different optical components is shown in table 6.1. The total transmission of these components is $TR = 0.38$. According to equation 6.2 this results in measured collection efficiency of 5.8(8)% for the π photons. This collection efficiency is higher comparing to other integrated methods [55] and multimode fibre methods [54]. The efficiency is smaller comparing to 25% for the micro-mirror method [52]. The advantage over this method is that the collected light with micro-mirrors is aberrated and without aberration correction most of the light will be lost in coupling to a single mode fibre. However the light collected with diffractive mirrors has a low aberration and we demonstrate that we can couple most of the power into a single mode fibre(see section 6.2.3).

The collection efficiency is smaller than the expected 8.7% collection efficiency(see section 6.1.2). This means that the actual diffraction efficiency of the mirror is 33% not

Optical Component	Transmission Rate
AR-coated vacuum window	0.995
5 AR-coated UV lenses	0.975
5 UV mirrors	0.95
Iris to limit the NA	0.5
Polariser	0.82
Total Transmission	0.38

Table 6.1: Table of the transmission rates of the optical components in experimental set-up for demonstration of the collection efficiency of the integrated mirror.

50%. This is most likely due to fabrication imperfections.

The collection efficiency for a mixed polarization is lower than the collection efficiency for the π photons. Because of the branching ratios, on average 1/3 of the emitted photons are π photons and 2/3 of them are σ photons(see section 5.1). Numerical calculation shows that the area that the mirror covers, collects 17.4% of the π photons and 11.3% of the σ photons. If we suppose that the diffraction efficiency is the same for both polarizations, the ratio of the collection efficiencies will be the ratio of these coverages therefore:

$$CE_\sigma = CE_\pi \times 11.3/17.4 = 3.8(5)\% \quad (6.3)$$

and the mixed polarization collection efficiency is:

$$CE_{mixed} = \frac{1}{3}CE_\pi + \frac{2}{3}CE_\sigma = 4.5(6)\% \quad (6.4)$$

To improve the collection efficiency for the future projects, one option is to use a trap that has a middle electrode with a width bigger than $80 \mu m$ to increase the covered area. Increasing the $127 \mu m$ is not preferable because it is selected to match the industry standard $127 \mu m$ pitch of V-groove fibre arrays. The other option is to use more steps in approximating the smooth profile of the diffraction rings. This option needs a fabrication method that has better accuracy comparing to electron lithography. Nano-imprinting is one option that can overcome the feature size limit imposed by limitation of the electron lithography. One problem in using this method is that the required pressure for the procedure is one Gpa and this is on the order of the stress fracture for the silicon wafers. Multi-layer grating method is also attractive and has shown to be able to reach 99% diffraction efficiency[77] but the dielectric layer used in this method can cause charging problem. One solution to this probelm can be using a transparent conducting film on top of the dielectric layer to prevent charging.

6.2 Single Mode Fibre Coupling Of the Ion Fluorescence

In many applications like remote entanglement, modular quantum computing with ions, using ion as a quantum memory and using ion as a photons source for quantum communication, single mode fibre coupling plays a crucial role. Most of the scalable solutions for the ion fluorescence collection, like micromirrors, suffer from poor mode quality. This means that fibre coupling the light collected needs aberration correction and without correction most of the light will be lost. The design of the diffractive mirrors is aberration free and even though we lose part of the light due to diffraction efficiency, most of the light collected in free space can be coupled into a single mode fibre.

6.2.1 Experimental Setup

In this experiment we use continuous fluorescence of the ion and compare the photon counts before the coupling lens and after the fibre. A schematic of the optical set-up is shown in Fig. 6.2.

For this experiment, it is very important to place the ion at the center of the mirror and set the ion height equal to the focal length of the mirror. Two μm offset in lateral positioning or one μm offset in height leads to significant increase in aberration and deteriorates the coupling efficiency. We set the ion position and height according to the procedure that was used for the near diffraction limited imaging experiment(section 4.4). The ion positions along the z direction was set to 871.1 μm . This position was chosen because it was at the middle of the range 869.1-873.1 μm . In this range, ion image is round and small but outside this range the image becomes clearly aberrated and skewed. The lateral position was set by applying E_x field weight of 0.2 which is equivalent to applying electric field of 200V/m to the ion. Again this value is in the middle of the range that we

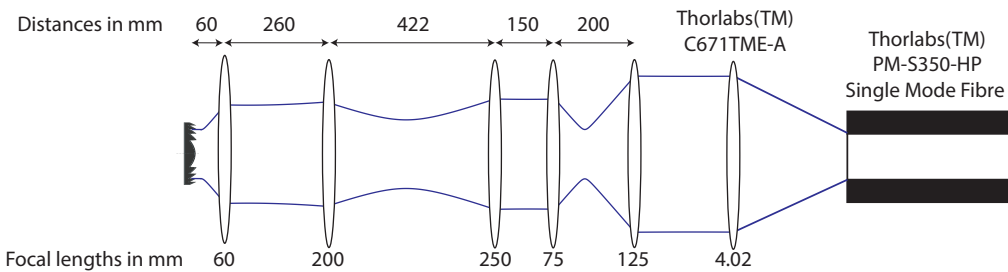


Figure 6.2: Optical set-up used for coupling ion fluorescence into the single mode fibre. The optical set-up collimates the ion light and resizes the beam to match it with the mode size of the fibre. An a-spheric lens couples the light into the single mode fibre.

can have a non-aberrated image. To set the ion height to $59.6 \mu m$, which is equal to the focal length of the 4th collimator, we used E_y field weight of 0.5(see section 4.4). Setting the ion height is the most sensitive part of the ion positioning and mismatch of one μm in this direction can notably increase the aberration.

To make the beam ready for the fibre coupling set-up, we need to create a collimated light with a diameter that matches the mode of the coupler. The coupling lens (Thor-labs(TM) C671TME-A), has a focal length of $4.02 mm$. The single mode fibre (Thor-labs(TM) PM-S350-HP) has $1/e^2$ mode field diameter of $2.3 \mu m$. Using the formula for the size of a focused Gaussian beam, we have:

$$D = \frac{\lambda f}{\pi d} \quad (6.5)$$

where D is the beam diameter before the lens, λ is the wavelength of the light, f is the focal length of the lens and d is the mode filed diameter at the focus. This shows that to match the mode we need to create a collimated beam with $1/e^2$ mode filed diameter of $1.03 mm$ before the coupling lens. In practice because of the astigmatism ,due to asymmetric dimensions of the mirror, we could not match the size of the both axis. We tried to match the average size to $1.03 mm$. The simulation of the optical set-up of Fig. 6.2, shown in Fig. 4.10, predicts the size of the beam to be $0.88 mm$ by $1.14 mm$. The measured beam size on the camera was $0.93 mm$ by $1.07 mm$. Most probably the slight discrepancy between the predicted and measured size is due to inaccuracy in measuring the distance between the lenses and setting the ion heigh to the focal length of the mirror.

The next step after preparing the beam size, was to align the position and angle of the beam to the fibre. The light from the ion is so week that practically it is impossible to align it to the fibre. To overcome this problem we used an axillary tracer laser beam. We used a flipper mirror to be able to switch between sending this laser beam or the ion light through the optical set-up. Using a neutral density filter we were able to switch between the low power(of the order of a few nW) and high power(of the order of a few μW). This laser was equipped with two adjustable mirrors to enable us to set the position and angel of this beam. We first used the low power tracer beam to overlap it with the ion light beam. This was accomplished by marking the position of the ion light beam on the camera at two different camera positions and iteratively change the position and angle of the tracer beam to match both of those positions. Then we used the high power tracer beam to set our coupling translator and coupled the beam into a multimode fibre. After maximizing the coupling into the multimode fibre we switched to the singlemode fibre and maximized it again. At this stage we switched to the ion beam and maximized the coupling for the ion beam. There are times that after switching to the ion beam, no signal can be detected. If this happens the tracer beam overlapping and coupling steps must be repeated.

6.2.2 Theoretical Estimation Of Fibre Coupling Efficiency

To estimate the coupling efficiency into the single mode fibre two factors are important. Mode size matching and the quality of the beam. The mode size matching efficiency is equal to the overlap of the 2-dimensional Gaussian profile of the beam with Gaussian profile of the fibre mode:

$$\eta_{size} = \frac{4\omega_{fibre}^2 \omega_x \omega_y}{(\omega_x^2 + \omega_{fibre}^2)(\omega_y^2 + \omega_{fibre}^2)} \quad (6.6)$$

where ω_{fibre} is the $1/e^2$ radius of the fibre mode, ω_x is the $1/e^2$ radius of the x axis of the beam and ω_y is the $1/e^2$ radius of the y axis of the beam. In our case with $\omega_{fibre} = 1.15\mu m$, $\omega_x = 1.03\mu m$ and $\omega_y = 1.19\mu m$, we have $\eta_{size} = 0.99$. This shows that the slight astigmatism of the beam is not a big factor in losing the power in fibre coupling.

A rough estimate for the effect of the mode quality is to divide η_{size} by the mode quality factor M^2 :

$$\eta_{SM} = \frac{\eta_{size}}{M^2} \quad (6.7)$$

As it was measured in section 4.4, The M^2 of the beam is 1.36 (x) and 1.54 (y). This amounts to average M^2 of 1.45. Therefore the total expected collection efficiency, η_{SM} , is 0.68. This number is with the assumption that the alignment and optical quality of our coupling lens is ideal but practically even with a perfect beam in the UV range we have 80% coupling efficiency. This is measured by coupling the direct output of two identical coupling set-up to each other. One the reasons for this loss is that in the UV range the diameter of the fibre is only $2.5\mu m$ and perfect alignment with the accuracy of our translation stages is impossible. The other reason is that the coupling lens adds some aberration to the beam. Moreover the fibre tip is not coated and we lose some fraction of the light due to Fresnel reflection:

$$R_s = \left| \frac{n_1 \cos \theta_i - n_2 \cos \theta_t}{n_1 \cos \theta_i + n_2 \cos \theta_t} \right|^2 \quad (6.8)$$

$$R_p = \left| \frac{n_1 \cos \theta_t - n_2 \cos \theta_i}{n_1 \cos \theta_t + n_2 \cos \theta_i} \right|^2 \quad (6.9)$$

where n_1 and n_2 are the refraction indexes of the two mediums, θ_i is the angle of incidence and θ_t is the angle of the transmitted beam. For the normal incidence between air with refraction index of 1 and pure silica with refractive of 1.458, $R_s = R_p = 0.035$. In total we lose 7% of the power at the two tips of the fibre.

The loss in propagation for our fibre is $0.05\text{ db}/m$. For the 2 m fibre that we use this amounts to 2.3% loss in the propagation.

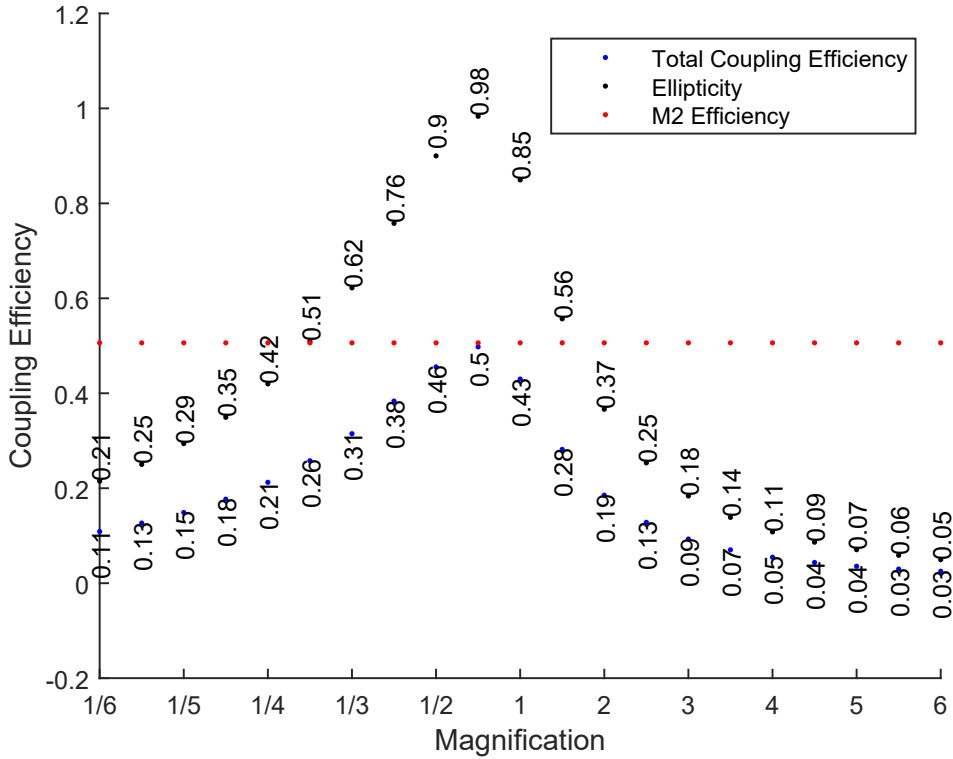


Figure 6.3: Theoretical simulation of single mode coupling efficiency. Mode size matching efficiency, effect of mode quality M^2 and total coupling efficiency is plotted for different magnifications.

The sum of all these losses leads to measured total transmission of 80%. By taking into account this transmission rate, the practical coupling efficiency that we expect is:

$$\eta_{Pr} = \eta_{SM} \times 0.80 = 0.54 \quad (6.10)$$

To find the best magnification for the resizing telescope I developed a Matlab routine that calculates and plots η_{size} and η_{SM} for different magnifications(at the tip of the fibre). To find the best magnification practically, we started from the top coupling point in the graph and tried the magnifications close to this value. The best telescope that we found was using the $f = 125\text{mm}$ and $f = 75\text{mm}$ with magnification of 1.67 which is equivalent to magnification of 0.60 at the tip of the fibre. This leads to $\eta_{size} = 0.99$, $\eta_{SM} = 0.68$ and $\eta_{Pr} = 0.54$

6.2.3 Measuring Single Mode Fibre Coupling Efficiency

Using continuous fluorescence of the ion and a PMT we measured number of photons per second before the coupling lens and after the fibre. The background corrected counts before the fibre was 42400 ± 2200 per second and after the fibre was 23900 ± 500 per second. Therefore $\eta_{Pr} = 0.57(4)$. Taking into account the 80% transmission of the coupler and the fibre we have $\eta_{SM} = 0.71(5)$. This number is close to predicted value of 0.68%.

To calculate the maximum achievable total collections efficiency into a single mode fibre we have:

$$SMCE = \eta_{SM} \times CE \quad (6.11)$$

where $SMCE$ is the single mode fibre collection efficiency, η_{SM} is the single mode coupling efficiency and CE is the diffractive mirror collection efficiency. With $\eta_{SM} = 71(5)\%$ and $CE = 5.8(8)\%$ this amounts to $SMCE = 4.1(6)\%$. This is almost three times better than the previous number of 1.4% using conventional lenses [64] and can significantly increase the efficiency of quantum communication and remote entanglement of the ions. The methods that mentioned to improve the collection efficiency of the mirrors, also improves the fibre coupling efficiency. Improving mode quality can also improve the coupling efficiency. Our design of diffraction rings is aberration free but average M^2 of 1.45 shows that there are fabrication defects that leads to aberration. Using fabrication methods that can reproduce the design with a better accuracy can decrease the aberration and improve the fibre coupling efficiency.

CHAPTER 7

Conclusion

7.1 Future Work

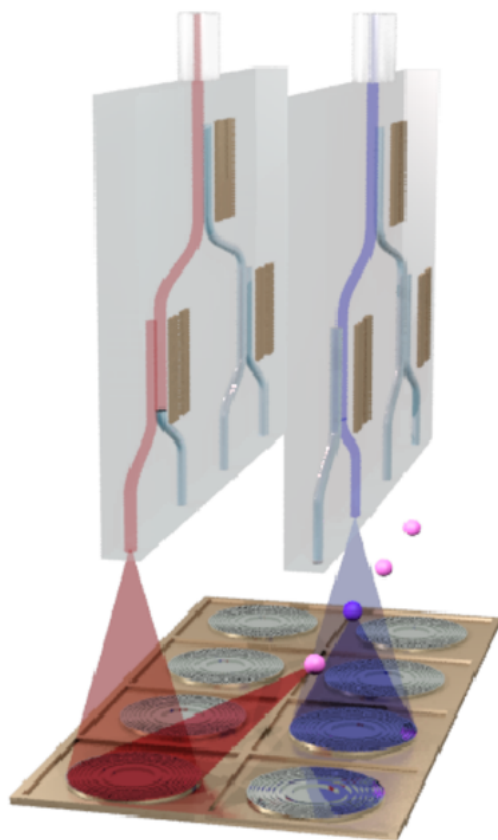


Figure 7.1: Future work

References

- [1] F. Splatt *et al.*, *Deterministic reordering of $^{40}\text{Ca}^+$ ions in a linear segmented Paul trap*, New J. Phys. **11**, 103008 (2009).
- [2] D. Kielpinski, *Entanglement and Decoherence in a Trapped-Ion Quantum Register*, PhD thesis, University of Colorado, 2001.
- [3] J. Chiaverini *et al.*, *Surface-Electrode Architecture for Ion-Trap Quantum Information Processing*, arXiv **quant-ph**, 0501147 (2005).
- [4] G. T. R. I. Q. S. Group, *GTRI Microwave Ion traps for QIP applications*.
- [5] A.-M. Martensson-Pendrill and D. S. G. P. Hannaford, *Isotope shifts and hyperfine structure in the 369.4-nm $6s\text{-}6p_{1/2}$ resonance line of single) ionized ytterbium*, Phys. Rev. A **49**, 3351 (1994).
- [6] H. M. Meyer, M. Steiner, L. Ratschbacher, C. Zipkes, and M. K02hl, *Laser spectroscopy and cooling of Yb^+ ions on a deep-UV transition*, Phys Rev. A **85**, 012502 (2012).
- [7] S. D. Saliba, M. Junker, L. D. Turner, and R. E. Scholten, *Mode stability of external cavity diode lasers*, Appl. Opt. **48**, 35 (2009).
- [8] V. R. Blums, *Ion Fluorescence Collection And Diffraction Limited Imaging From A Microfabricated Ion Trap With Integrated Diffractive Mirrors*, Master's thesis, Griffith University, 2012.
- [9] J. P. Dowling and G. J. Milburn, *Quantum Technology: The Second Quantum Revolution*, Arxive , 0206091 (2002).
- [10] T. H. Maiman, *Stimulated Optical Emission in Fluorescent Solids. I. Theoretical Considerations*, Pys. Rev. Lett. **123**, 1145 (1961).
- [11] R. P. Feynman, *Simulating Physics with Computers*, Int. J. Theor. Phys. **21**, 467 (1982).
- [12] M. A. Nielsen and I. L. Chuang, *Atomic Physics* (Cambridge University Press, 2000).

- [13] *Algorithms for quantum computation: discrete logarithms and factoring*, Santa Fe, NM, USA, 1994, IEEE.
- [14] D. Bes, *Quantum Mechanics: A Modern and Concise Introductory Course* (Springer, 2012).
- [15] C. Bennett and G. Brassard, *Quantum Cryptography: Public Key Distribution and Coin Tossing*, Proc Intl Conf Comp Sys Sig Proc,(IEEE Bangalore India) , 175 (1984).
- [16] J. L. O'Brien, G. J. Pryde1, A. G. White1, T. C. Ralph1, and D. Branning, *Demonstration of an all-optical quantum controlled-NOT gate*, Nature **426**, 264 (2003).
- [17] D. P. DiVincenzo, *The Physical Implementation of Quantum Computation*, Fortschritte der Physik **48**, 771 (2000).
- [18] T. P. Harty *et al.*, *High-Fidelity Preparation, Gates, Memory, and Readout of a Trapped-Ion Quantum Bit*, Phys. Rev. Lett. **113**, 220501 (2014).
- [19] R. Blatt, H. H. C. F. Roos, C. Becher, and F. Schmidt-Kaler, *Ion Trap Quantum Computing with Ca+ Ions*, Quant. Inf. Proc. **3**, 1 (2004).
- [20] B. E. King *et al.*, *Cooling the Collective Motion of Trapped Ions to Initialize a Quantum Register*, Phys. Rev. Lett. **81**, 1528 (1998).
- [21] C. Roos *et al.*, *Quantum State Engineering on an Optical Transition and Decoherence in a Paul Trap*, Phys. Rev. Lett. **83**, 4713 (1998).
- [22] C. Monroe, D. M. Meekhof, B. E. King, W. M. Itano, and D. J. Wineland, *Demonstration of a Fundamental Quantum Logic Gate*, Phys. Rev. Lett. **75**, 4714 (1995).
- [23] M. A. Rowe *et al.*, *Experimental violation of a Bell's inequality with efficient detection*, Nature **409**, 791 (2000).
- [24] K. R. Brown *et al.*, *Single-qubit-gate error below 10^{-4} in a trapped ion*, Phys. Rev. A **84**, 030303 (2011).
- [25] J. Benhelm, G. Kirchmair, C. F. Roos, and R. Blatt, *Towards fault-tolerant quantum computing with trapped ions*, **174**, 1 (2008).
- [26] J. Chiaverini *et al.*, *Realization of quantum error correction*, Nature **432**, 602 (2004).
- [27] J. F. Goodwin *et al.*, *Trapped-ion quantum error-correcting protocols using only global operations*, Phys. Rev. A **92**, 032314 (2015).

- [28] S. Debnath *et al.*, *Demonstration of a programmable quantum computer module*, arXiv (2016).
- [29] T. Monz, I. L. Chuang, and R. Blatt, *Realization of a scalable Shor algorithm*, Science **351**, 1068 (2016).
- [30] K.-A. Brickman *et al.*, *Implementation of Grover's quantum search algorithm in a scalable system*, Phys. Rev. A **72**, 050306(R) (2005).
- [31] D. L. Moehring *et al.*, *Entanglement of single-atom quantum bits at a distance*, Nature **449**, 68 (2007).
- [32] J. Cirac and P. Zoller, *Quantum Computations with Cold Trapped Ions*, Phys. Rev. Lett. **74**, 4091 (1994).
- [33] A. Sørensen and K. Mølmer, *Entanglement and quantum computation with ions in thermal motion*, Phys. Rev. A **62**, 022311 (2000).
- [34] D. J. Wineland *et al.*, *Experimental Issues in Coherent Quantum-State Manipulation of Trapped Atomic Ions*, J. Res. NIST. **103**, 259 (1998).
- [35] R. J. Hughes, D. F. V. James, E. H. Knill, R. Laflamme, and A. G. Petschek, *Decoherence Bounds on Quantum Computation with Trapped Ions*, Phys. Rev. Lett. **77**, 3240 (1996).
- [36] T. Monz *et al.*, *14-Qubit Entanglement: Creation and Coherence*, Phys. Rev. Lett. **106**, 13050 (2011).
- [37] C. Monroe *et al.*, *Large-scale modular quantum-computer architecture with atomic memory and photonic interconnects*, Phys. Rev. A **89**, 022317 (2014).
- [38] L.-M. Duan and C. Monroe, *Colloquium: Quantum networks with trapped ions*, Rev. Mod. Phys. **82**, 1209 (2010).
- [39] D. Kielpinski, C. Monroe, and D. Wineland, *Architecture for a large-scale ion-trap quantum computer*, Nature **417**, 709 (2002).
- [40] S. Seidelin *et al.*, *Microfabricated Surface-Electrode Ion Trap for Scalable Quantum Information Processing*, Phys. Rev. Lett. **96**, 253003 (2006).
- [41] J. M. Amini *et al.*, *Towards scalable ion traps for quantum information processing*, New J. Phys. **12**, 033031 (2010).
- [42] W. K. Hensinger *et al.*, *T-junction ion trap array for two-dimensional ion shuttling, storage, and manipulation*, 60Appl. Phys. Lett. **88**, 034101 (2006).

- [43] D. Hucul, M. Yeo, W. Hensinger, J. Rabchuk, and S. O. andsa C. Monroe, *On the transport of atomic ions in linear and multidimensinal ion trap arrays*, Quantum Inf. Comput. **8**, 501 (2008).
- [44] R. B. Blakestad *et al.*, *High-Fidelity Transport of Trapped-Ion Qubits through an X-Junction Trap Array*, Phys. Rev. Lett. **102**, 153002 (2009).
- [45] H. C. Nägerl *et al.*, *Laser addressing of individual ions in a linear ion trap*, Phys. Rev. A **60**, 145 (1999).
- [46] S. Crain, E. Mount, S. Baek, and J. Kim, *Individual addressing of trapped $^{171}\text{Yb}^+$ ion qubits using a microelectromechanical systems-based beam steering system*, APPLIED PHYSICS LETTERS **105**, 181115 (2014).
- [47] K. K. Mehta *et al.*, *Integrated optical addressing of an ion qubit*, arXiv (2015).
- [48] S. Olmschenk *et al.*, *Quantum Teleportation Between Distant Matter Qubits*, Science **323**, 486 (2009).
- [49] G. R. Guthöhrlein, M. Keller, K. Hayasaka, W. Lange, and H. Walther, *A single ion as a nanoscopic probe of an optical field*, Nature **414**, 49 (2001).
- [50] A. B. Mundt *et al.*, *Coupling a Single Atomic Quantum Bit to a High Finesse Optical Cavity*, Phys. Rev. Lett. **89**, 103001 (2002).
- [51] D. R. Leibrandt, J. Labaziewicz, V. Vuletic, and I. L. Chuang, *Cavity Sideband Cooling of a Single Trapped Ion*, Phys. Rev. Lett. **103**, 103001 (2009).
- [52] G. Shu, N. Kurz, M. R. Dietrich, and B. B. Blinov, *Efficient fluorescence collection from trapped ions with an integrated spherical mirror*, Phys Rev A **81**, 042321 (2010).
- [53] J. T. Merrill *et al.*, *Demonstration of integrated microscale optics in surface-electrode ion traps*, New J Phys **13**, 103005 (2011).
- [54] A. P. Vandevender, Y. Colombe, J. Amini, D. Leibfried, and D. J. Wineland, *Efficient Fiber Optic Detection of Trapped Ion Fluorescence*, Phys. Rev. Lett. **105**, 023001 (2010).
- [55] C. R. Clark *et al.*, *Characterization of Fluorescence Collection Optics Integrated with a Microfabricated Surface Electrode Ion Trap*, Phys. Rev. Applied **1**, 024004 (2014).
- [56] A. Wilson *et al.*, *Fiber-coupled single ion as an efficient quantum light source*, Arxive **1**, 1101.5877 (2011).

- [57] E. W. Streed, B. G. Norton, A. Jechow, T. J. Weinhold, and D. Kielpinski, *Imaging of Trapped Ions with a Microfabricated Optic for Quantum Information Processing*, Phys. Rev. Lett. **106**, 010502 (2011).
- [58] A. Jechow, E. W. Streed, B. G. Norton, M. J. Petrasius, and D. Kielpinski, *Wavelength-scale imaging of trapped ions using a phase Fresnel lens*, Opt. Lett. **36**, 1371 (2011).
- [59] E. W. Streed, A. Jechow, B. G. Norton, and D. Kielpinski, *Absorption imaging of a single atoms*, Nat. Commun. **3**, 933 (2012).
- [60] P. M. nad S. Olmschenk, D. Hayes, D. N. Matsukevich, L.-M. Duan, and C. Monroe, *Heralded Quantum Gate between Remote Quantum Memories*, Phys. Rev. Lett. **109**, 250502 (2009).
- [61] D. N. Matsukevich, P. Maunz, D. L. Moehring, S. Olmschenk, and C. Monroe, *Bell Inequality Violation with Two Remote Atomic Qubits*, Phys. Rev. Lett. **100**, 150404 (2004).
- [62] S. Gerber *et al.*, *Quantum interference from remotely trapped ions*, New Journal of Physics **11**, 013032 (2009).
- [63] B. B. Blinov, D. L. Moehring, L.-M. Duan, and C. Monroe, *Observation of entanglement between a single trapped atom and a single photon*, Nature **428**, 153 (2004).
- [64] D. Hucul *et al.*, *Modular entanglement of atomic qubits using photons and phonons.*, Nature **11**, 37 (2015).
- [65] L. Deslauriers, *Cooling and Heating of the Quantum Motion of Trapped Cd+ Ions*, PhD thesis, University of Michigan, 2006.
- [66] D. W. Macalpine and R. O. Schildknecht, *Coaxial resonators with helical inner conductor*, Proc. of the IRE **47** (2010).
- [67] T. Shiono, M. Kitagawa, K. Setsune, and T. Mitsuyu, *Reflection micro-Fresnel lenses and their use in an integrated focus sensor*, Appl. Opt. **28**, 3434 (1989).
- [68] A. Kreuter *et al.*, *Spontaneous Emission Lifetime of a Single Trapped Ca+ Ion in a High Finesse Cavity*, Phys. Rev. Lett. **92**, 203002 (2004).
- [69] L. X *et al.*, *Direct imprint of nanostructures in metals using porous anodic alumina stamps*, Nanotechnology **24**, 2553036 (2013).
- [70] H. J. Metcalf and P. van der Straten, *Laser Cooling and Trapping* (Springer, 1999).

- [71] J. Böhlke *et al.*, *Isotopic Compositions of the Elements, 2001*, Journal of Physical and Chemical Reference Data **34**, 57 (2005).
- [72] D. Das, S. Barthwal, A. Banerjee, and V. Natarajan, *Absolute frequency measurements in Yb with 0.08 ppb uncertainty: Isotope shifts and hyperfine structure in the 399-nm 1S0-1P1 line*, Phys. Rev. A **72**, 032506 (2005).
- [73] S. Olmschenk *et al.*, *Manipulation and detection of a trapped Yb+ hyperfine qubit*, Phys. Rev. A **76**, 052314 (2007).
- [74] P. Meystre and M. Sargent III, *Elements of Quantum Optics* (Springer-Verlag, Berlin, 1990).
- [75] B. E. A. Saleh and M. C. Teich, *Fundamentals of Photonics* (John Wiley and Sons Ltd, 2007).
- [76] M. Fox, *Quantum Optics: An Introduction* (Oxford University Press, 2006).
- [77] N. Destouches, J. C. P. A. V. Tishchenko, S. Reynaud, and O. Parriaux, *99% efficiency measured in the 1st order of a resonant grating*, Opt. Express **13**, 3231 (2005).